

AD-A081 584

HONEYWELL ELECTRO-OPTICS CENTER LEXINGTON MA
SPATIAL RADIOMETER. VOLUME 1.(U)

F/6 17/5

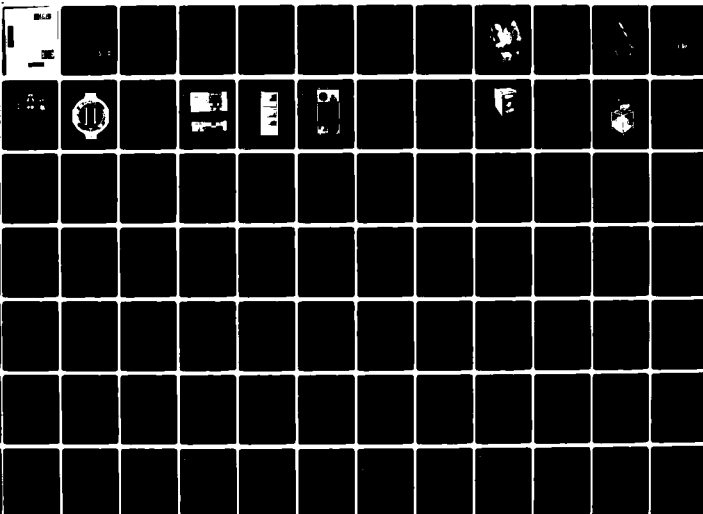
MAR 79 R SULLIVAN
7902-4-VOL-1

F19628-75-C-0179
NL

UNCLASSIFIED

AFGL-TR-80-0061-VOL-1

1 3
4
5



Unclassified
SECURITY CLASSIFICATION OF THIS PAGE (When Data Entered)

| 19 REPORT DOCUMENTATION PAGE | | READ INSTRUCTIONS BEFORE COMPLETING FORM | |
|---|---|--|--|
| 1. REPORT NUMBER AFGL TR-80-1161-VOL-1 | 2. GOVT ACCESSION NO. | 3. RECIPIENT'S CATALOG NUMBER | |
| 4. TITLE (and Subtitle) SPATIAL RADIOMETER. Volume 1, 1978 | 5. TYPE OF REPORT & PERIOD COVERED Final Report. 10 Nov 77 - 7 Sep 78. | | |
| 6. AUTHOR(s) Richard Sullivan | 7. CONTRACT OR GRANT NUMBER(s) F19628-75-C-0179 | 8. PERFORMING ORG. REPORT NUMBER | |
| 9. PERFORMING ORGANIZATION NAME AND ADDRESS Honeywell Radiation Center 2 Forbes Road Lexington, Massachusetts 02173 | 10. PROGRAM ELEMENT, PROJECT, TASK AREA & WORK UNIT NUMBERS 63424F 212303AC | 11. REPORT DATE March 1979 | |
| 11. CONTROLLING OFFICE NAME AND ADDRESS Air Force Geophysics Laboratory Hanscom AFB, Massachusetts 01731 Monitor/Ned Wheeler/OPR | 12. NUMBER OF PAGES 238 | 13. SECURITY CLASS. (of this report) Unclassified | |
| 14. MONITORING AGENCY NAME & ADDRESS (if different from Controlling Office) | 15a. DECLASSIFICATION/DOWNGRADING SCHEDULE | | |
| 16. DISTRIBUTION STATEMENT (of this Report) Approved for public release; distribution unlimited. | | | |
| 17. DISTRIBUTION STATEMENT (of the abstract entered in Block 20, if different from Report) 7902-4-VOL-1 | | | |
| 18. SUPPLEMENTARY NOTES | | | |
| 19. KEY WORDS (Continue on reverse side if necessary and identify by block number) Spatial Radiometer System Parameters | | | |
| 20. ABSTRACT (Continue on reverse side if necessary and identify by block number) This final report describes the Spatial Radiometer System, analysis, operational parameters and data results of the Head No. 1 system launch on 10 November 1977 at White Sands Missile Range, New Mexico. In addition, this final report contains the operational parameters and data of Head No. 2, thru 31 December 1978. Head No. 2 was not launched on 7 September 1978 due to pre-separation on the launch pad and is rescheduled for an early 1979 flight. | | | |

DD FORM 1 JAN 73 1473

393 776

Unclassified

SECURITY CLASSIFICATION OF THIS PAGE (When Data Entered)

SECURITY CLASSIFICATION OF THIS PAGE(When Data Entered)

SECRET
NO FORN DISSEM
E

SECURITY CLASSIFICATION OF THIS PAGE(When Data Entered)

SPATIAL RADIOMETER

Final Report

VOLUME NO. 1 OF 2

PREPARED FOR
AIR FORCE GEOPHYSICS LABORATORY
HANSCOM AFB
BEDFORD, MA 01731

DOCUMENT NO. 7902-4
CONTRACT NO. F19628-75-C-0179
MARCH 1979

HONEYWELL
Electro-Optics Center
2 Forbes Road
Lexington, Massachusetts 02173

SUMMARY

This final report describes the Spatial Radiometer System, analysis, operational parameters and data results of the Head No. 1 system launch on 10 November 1977 at White Sands Missile Range, New Mexico.

In addition, this final report contains the operational parameters and data of Head No. 2, thru 31 December 1978. Head No. 2 was not launched on 7 September 1978 due to pre-separation on the launch pad and is rescheduled for an early 1979 flight.

| | | |
|---------------------------------|---------------|-------------------------------------|
| ACCESSION for | | |
| NTIS | White Section | <input checked="" type="checkbox"/> |
| DOC | Buff Section | <input type="checkbox"/> |
| UNANNOUNCED | | <input type="checkbox"/> |
| JUSTIFICATION _____ | | |
| BY _____ | | |
| DISTRIBUTION/AVAILABILITY CODES | | |
| Dist. | AVAIL. and/or | SPECIAL |
| A | | |

TABLE OF CONTENTS

| | PAGE |
|---|------|
| SECTION I INTRODUCTION | 1-1 |
| SECTION II ELECTRONICS | 2-1 |
| SECTION III SCAN MIRROR DESIGN | 3-1 |
| SECTION IV OPTICAL DESIGN | 4-1 |
| SECTION V OFF AXIS ANALYSIS | 5-1 |
| SECTION VI OFF AXIS TEST DATA | 6-1 |
| SECTION VII CRYOGENIC DESIGN AND TEST RESULTS | 7-1 |
| SECTION VIII STRUCTURAL DESIGN ANALYSIS | 8-1 |
| SECTION VX INTERNAL CALIBRATION | 9-1 |
| SECTION X FOCAL PLANE DESIGN | 10-1 |
| SECTION XI QUALIFICATION TESTS | 11-1 |
| SECTION XII SYSTEM OPERATIONAL PARAMETERS AND TEST RESULTS | 12-1 |
| SECTION XIII PRE-FLIGHT/FLIGHT DATA | 13-1 |
| SECTION XIV SYSTEM NO. 2 | 14-1 |

SECTION I

INTRODUCTION - SPATIAL RADIOMETER

1.0 INTRODUCTION

In 1976 Honeywell Electro-Optics Center was awarded a contract through Air Force Geophysics Laboratory/Electronic System Division AFGL/ESD, Bedford, Massachusetts, funded by SAMSO to design, build, and test two Spatial Radiometers for use on the Multi-spectral Measurements program.

The primary objective of the Spatial Radiometer System is to provide an absolute radiometric map of low thrust level rocket plumes over a large dynamic range in two spectral channels.

2.0 GENERAL SYSTEM DESCRIPTION

The Spatial Radiometer System consists of the sensor, sensor electronics, power supply, and interconnecting cables. Figure 1 shows the designed system.

The sensor is 27" long by 14" in diameter and weighs 80 lbs. A flange around the outside diameter provides the mounting support to the payload. The cryogenic and vacuum pumping and electrical access is at the rear of the sensor. A pop off 6" cover is mounted at the front of the sensor.

The sensor electronics is housed in a 10" x 9" x 9" welded aluminum box weighing 8 lbs.

The power supply is an 8" x 7" x 3" aluminum box weighing 8 lbs.

In order to operate the system a Ground Support Equipment (GSE) System supplied by AFGL is used. Also utilized for data reduction is Government Furnished Equipment (GFE) supplied Infrared Background Sensor GSE equipment, to supplement the SP/RAD System, including a computer (UK44A1), mag-tape transport (UK52A1), CRT Display Terminal (UK46A) and Hardcopy Unit (UK45A).



01474

Figure 1 Spatial Radiometer System

Also used to assist with data reduction is an EOC supplied Disk Pack Drive Model 273, a Model No. 1200A Honeywell Line Printer and a Turbo Molecular Vacuum Pumping System.

3.0 DETAIL DESCRIPTION OF SYSTEM COMPONENTS

Figure 2 shows a breakdown in the sensor assembly components.

The vacuum vessel is constructed from 6061-T6 aluminum with viton "O" rings providing the vacuum seal. The overall length of the dewar is 27" and 12" in diameter. The mounting ring flange is 13" in diameter. An extended cylinder of 6" in diameter by 3" long provides the mounting and access port for the detector assembly (ref. Figure 3).

The optical bench/brazement assembly is constructed from 6061-T6 aluminum and provides the mounting structure for the optical and detector components. In addition, the cryogenic cooling tanks are part of this structure. The overall size of the optical bench is 22" long and 9" in diameter with an 11" diameter mounting flange (ref. Figure 4).

The multilayer insulation jacket consists of a calculated number of layers of .00025 mil thick aluminized mylar loosely wrapped and covered with an outer shell of .005 mil aluminized mylar. This jacket is made in two separate sections that fit in the base of the vacuum vessel and the top portion.

The front cover is 6" in diameter and provides the vacuum seal prior to ejection during the system flight. The ejection system consists of explosive bellows, hermetically sealed, activated by an electrical signal. These covers have been flown on other programs and are purchased from Utah State University.

The fill and vent lines for the cryogenic system are .25" stainless steel lines. The fill line connects to the tank. The two

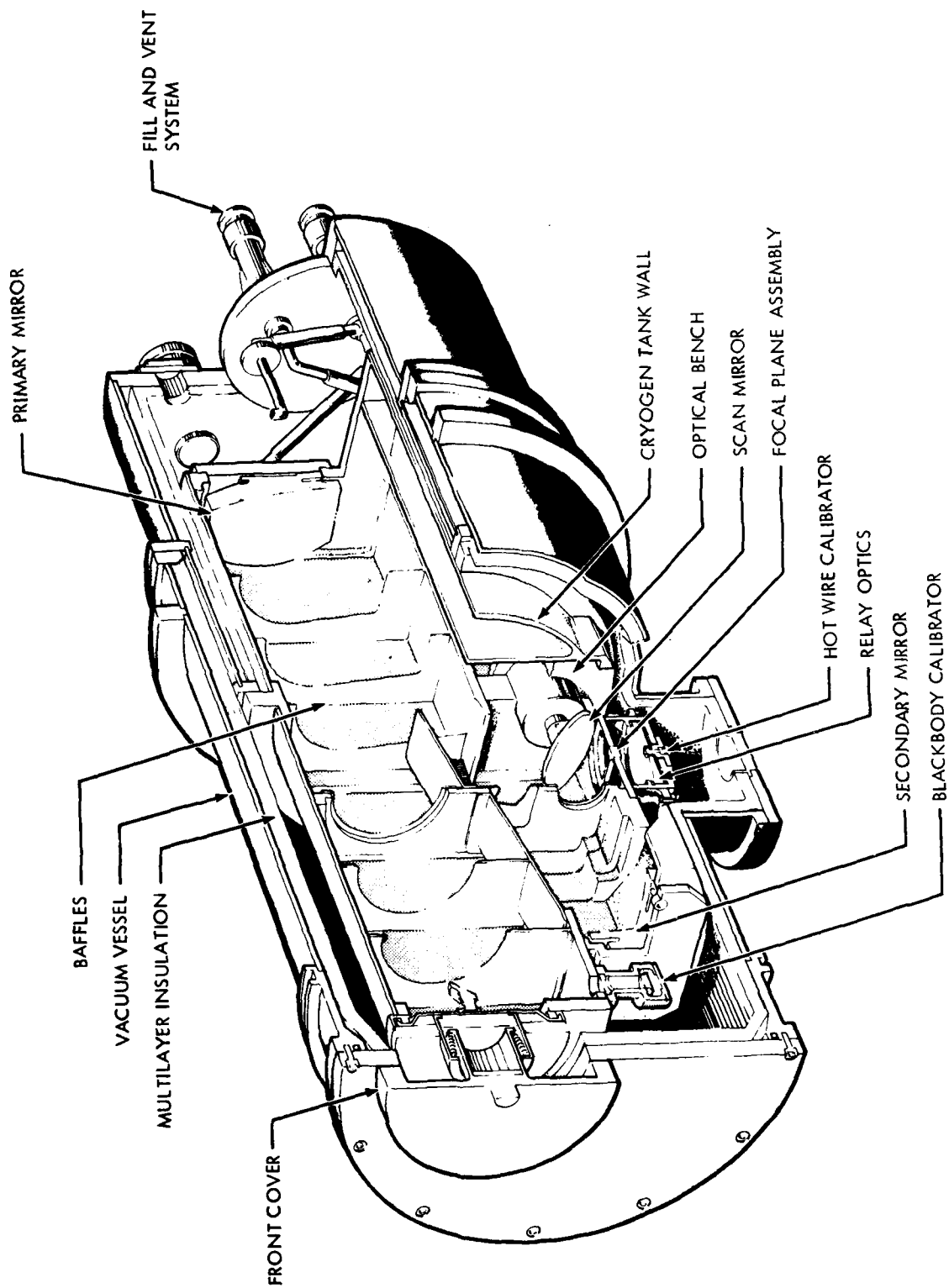


Figure 2 Spatial Radiometer



Figure 3 Vacuum Vessel

01753



Figure 4 Optical Bench

01752

return lines from the top of each tank are connected together at the vacuum vessel. The external lines are vacuum jacketed to eliminate frosting during the fill procedure.

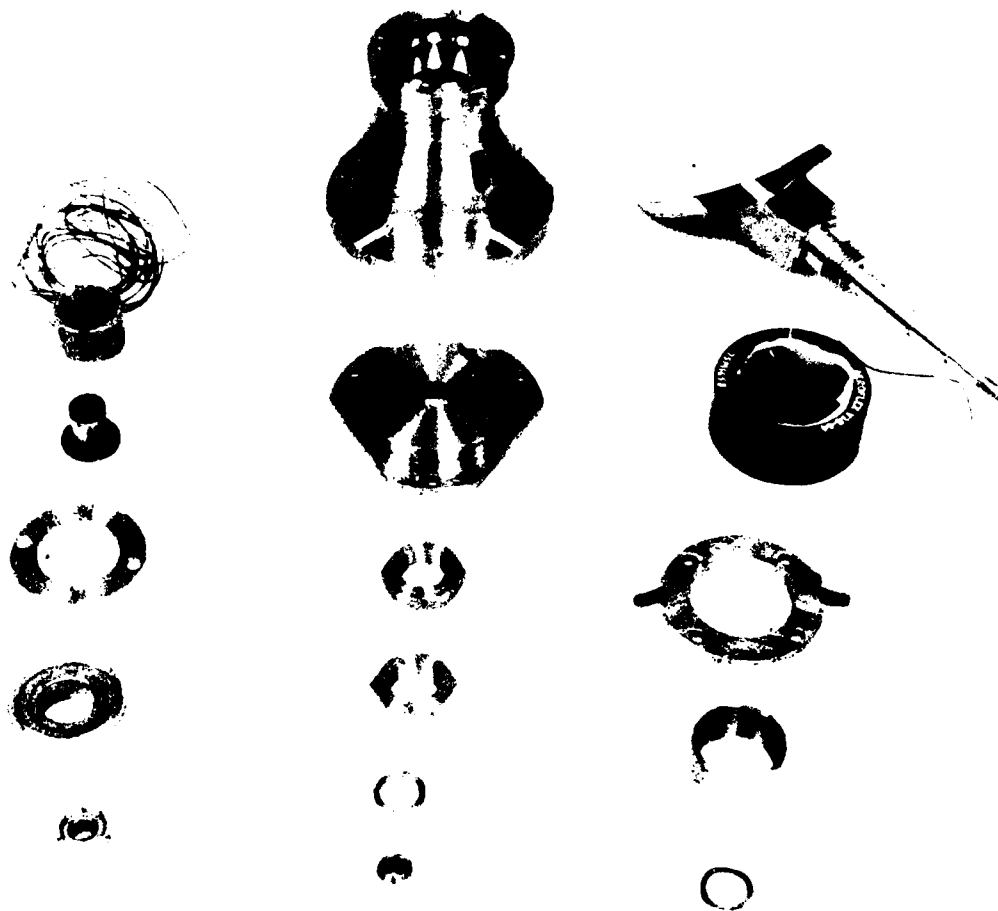
All mirrors are constructed from 6061-T6 aluminum, electroplated nickel plated and gold coated. The primary and secondary mirrors are parabolas which form a confocal pair. A second focus is formed by relay optics to the focal plane detector.

The scan mirror assembly consists of a 2" diameter 45° mirror driven by a dc torque motor mounted in a housing. A rotary variable differential transducer indicates the mirror position. Special barden low temperature bearings are mounted on the mirror shaft. All materials are stainless steel construction except for the motor and RVDT readout device. The mirror scan rate is $24^\circ/\text{s}$ constant velocity drive with a total scan of 24° (ref. Figure 5),

The focal plane assembly is .5" in diameter mounted to a circular spider ring design of 4" in diameter. Four separate Microdot connectors mounted to Kapton cable lines make the electrical connections to the focal plane assembly. The focal plane is constructed using HgCdTe detectors for operation at 77K. There are 40 elements, 20 each for the short and medium wavelength respectively. Of the 20 elements per color, 10 each have a $0.4^\circ \times 0.4^\circ$ IFOV and 10 each have $0.2^\circ \times 0.2^\circ$ IFOV. The array is 4° long for the $.4^\circ$ elements and 2° long for the $.2^\circ$ elements. The sensor total field of view is $6^\circ \times 4^\circ$ for the large elements and $6^\circ \times 2^\circ$ for the small elements (ref. Figure 6).

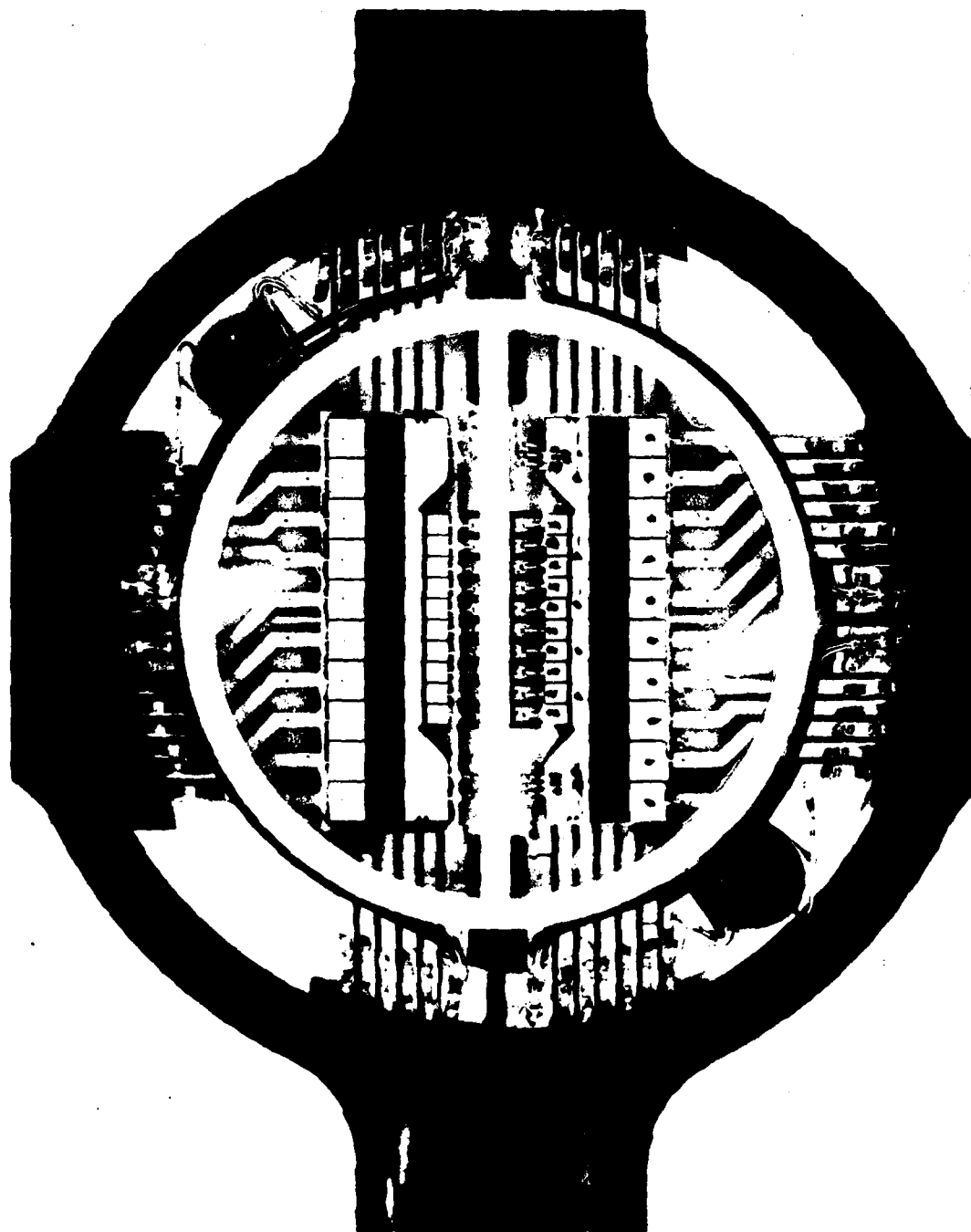
All baffles are constructed from 6061-T6 aluminum and are mechanically fastened internal on the optical bench assembly. Knife edges are machined on each baffle.

A 300K blackbody calibration assembly is mounted to the brazement assembly. The assembly consists of a blackbody cavity



01754

Figure 5 Scan Mirror



01427

Figure 6 Focal Panel

mounted into a housing with a nichrome wire heater and two thermistors used in the control circuit. This assembly is then mounted into another housing and lens mount. The overall size is 1.5" in diameter by 2" long.

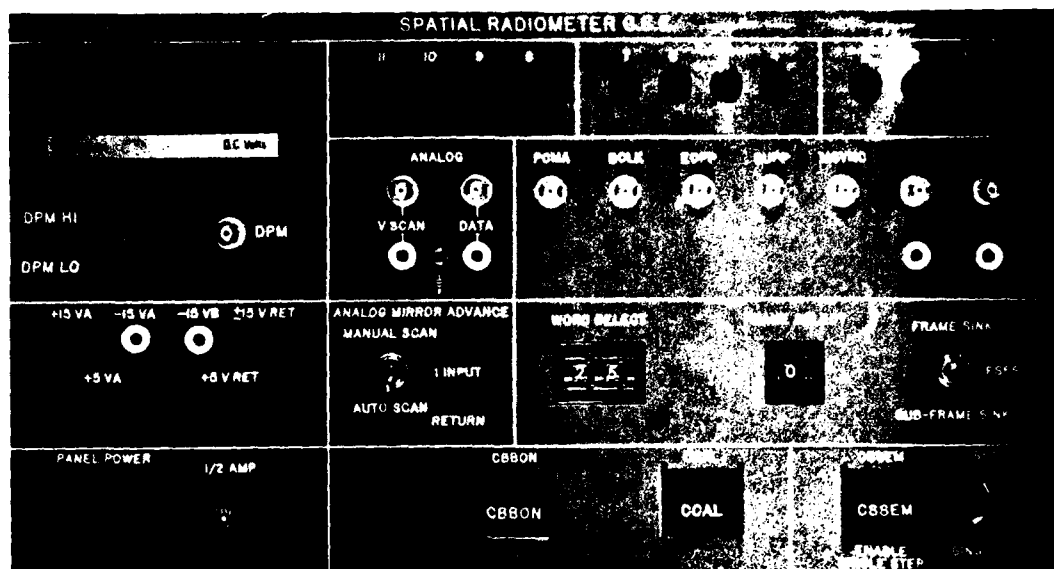
The hot wire assembly is a miniature tungsten lamp with the outer glass shell removed and the lamp base posted into a metal housing.

The power supply is packaged in an aluminum box 7.5" by 6.5" by 3" high.

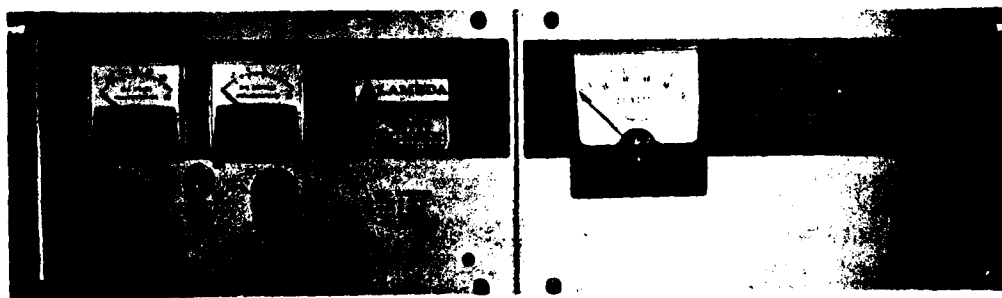
The electronic box assembly is constructed from .06" thick 6061-T6 aluminum spot welded. Mounting frames and card guides are held in place with screws and hardware. The overall size of the electronic package is 10.5" x 9" x 8.5" high. The printed circuit boards are 7" x 7" x .07" thick manufactured from copper clad plastic sheet per MIL-P-55617 type TL-GF0040C1/OA2. All components are MIL spec and all workmanship inspected by EOC in process inspection methods. The boards are mounted into the chassis and are held in place by a top cover with a vibration damper mounting pad.

The ground support system used to support the spatial radiometer program includes the following.

To operate the system, AFGL supplied a control panel and power supply (Figure 7). Equipment for data reduction was borrowed from the Infrared Background Sensor Program including a computer (Figure 8), magnetic tape transport (Figure 9), CRT display terminal (Figure 10), and a hardcopy unit (Figure 11). Also used to assist with data reduction is an EOC supplied disk pack drive unit (Figure 12), Model 1200A Honeywell line printer (Figure 13), and a vacuum pumping station (Figure 14.).



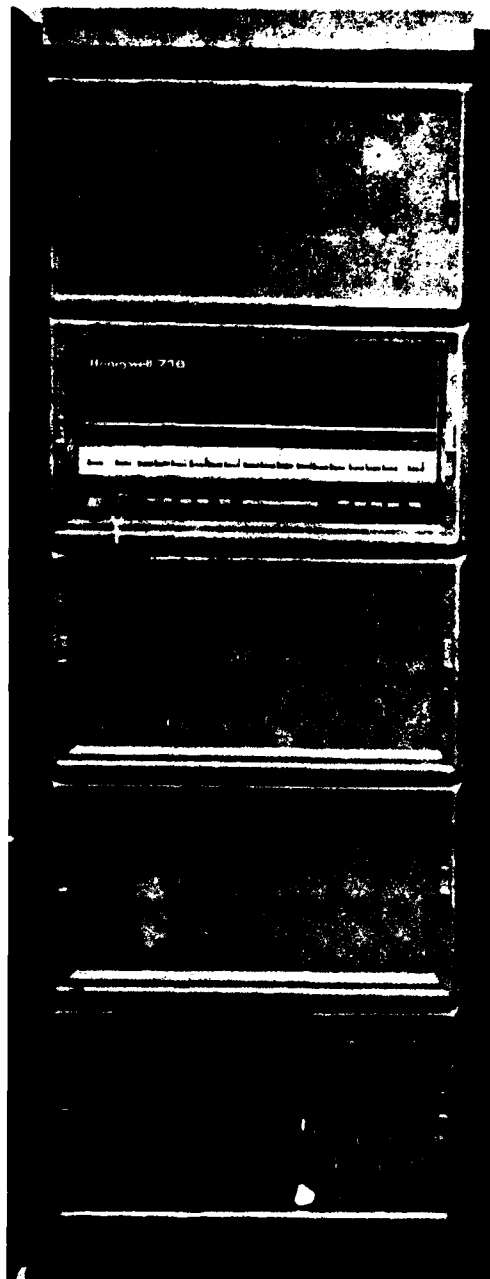
CONTROL PANEL



POWER SUPPLY

01475

Figure 7 AFGL/GSE System



01295

Figure 8 Computer

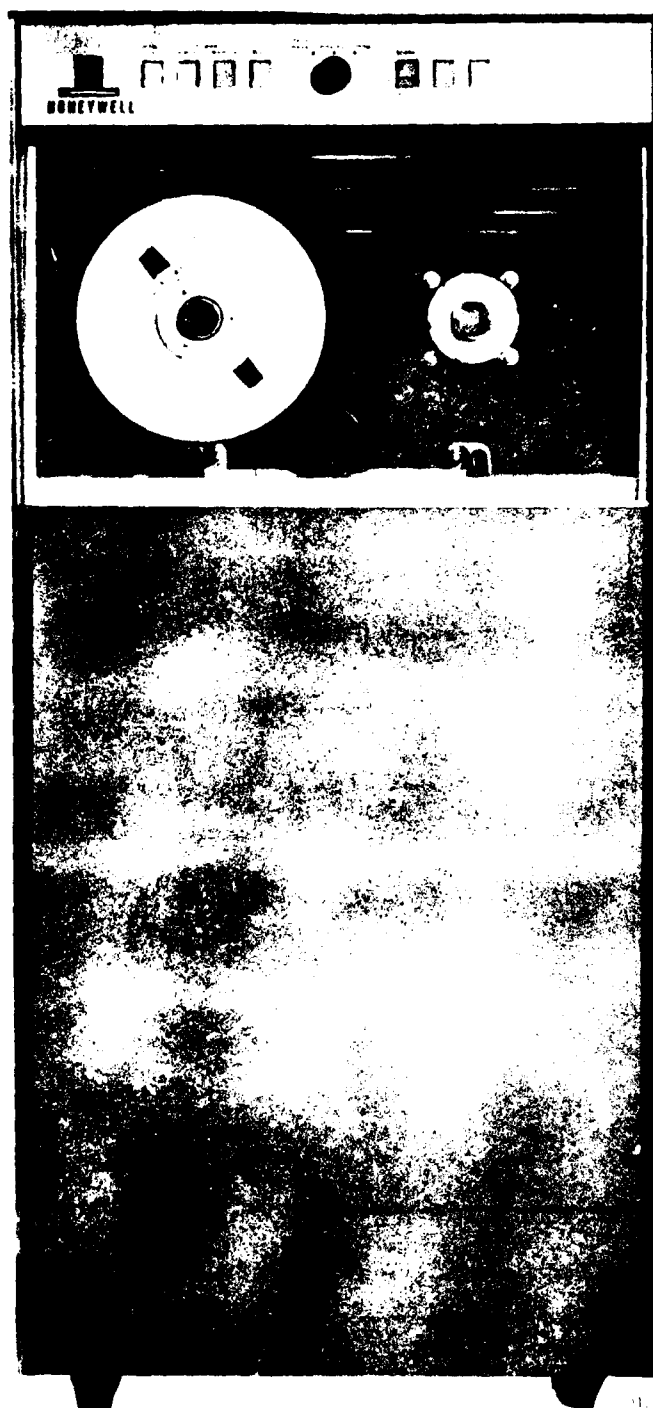


Figure 9 Mag-Tape Transport (UK52A1)

1-14

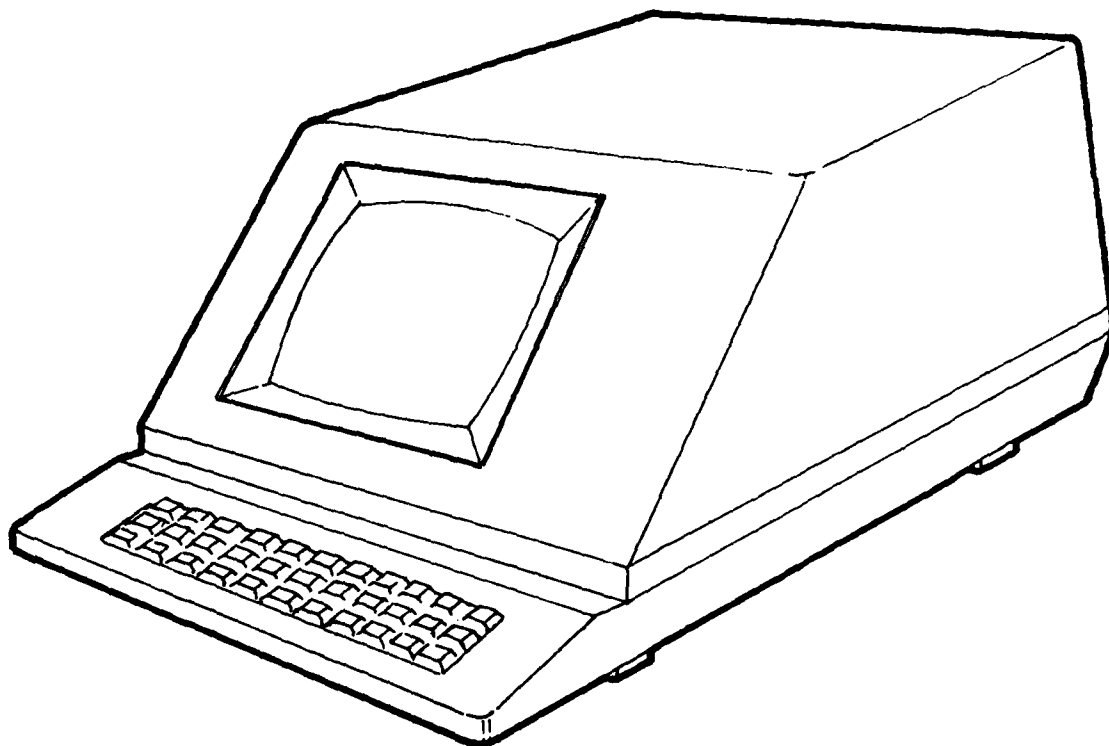


Figure 10 CRT Display Terminal

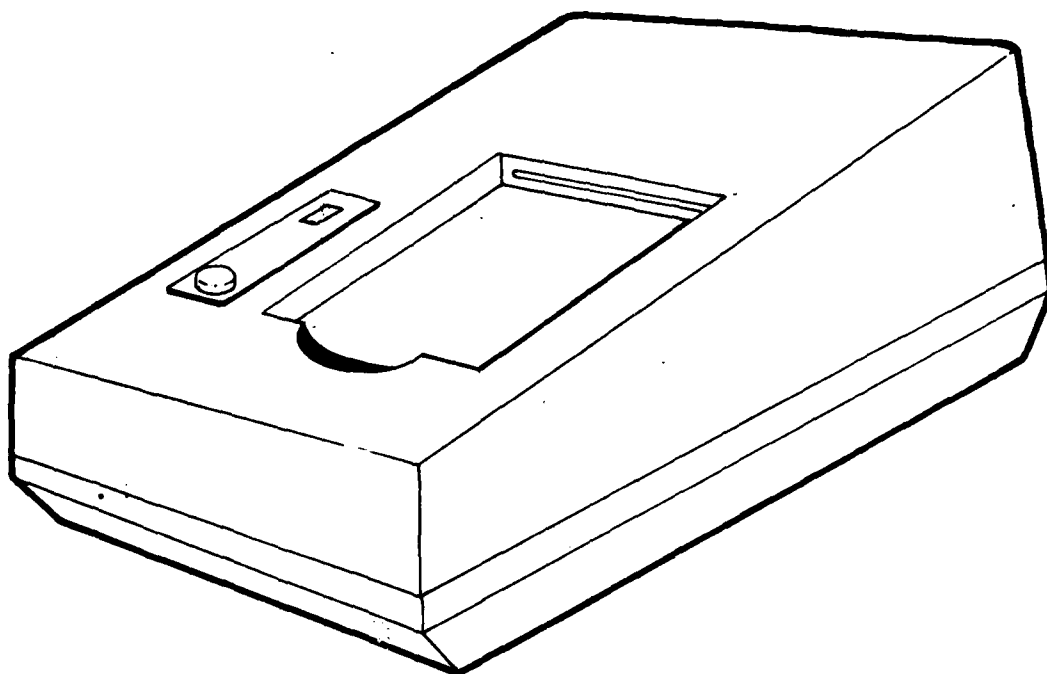


Figure 11 Hard Copy Unit (UK45A)

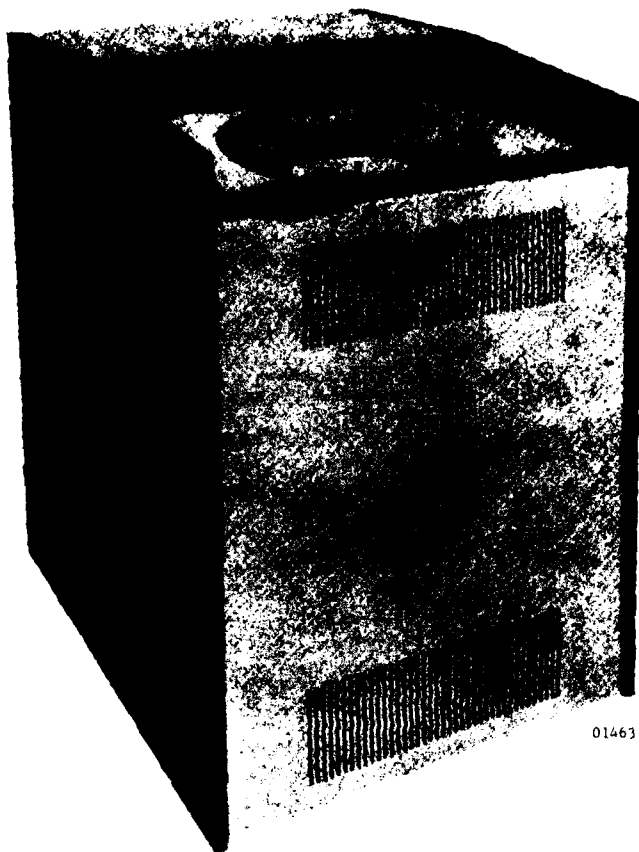
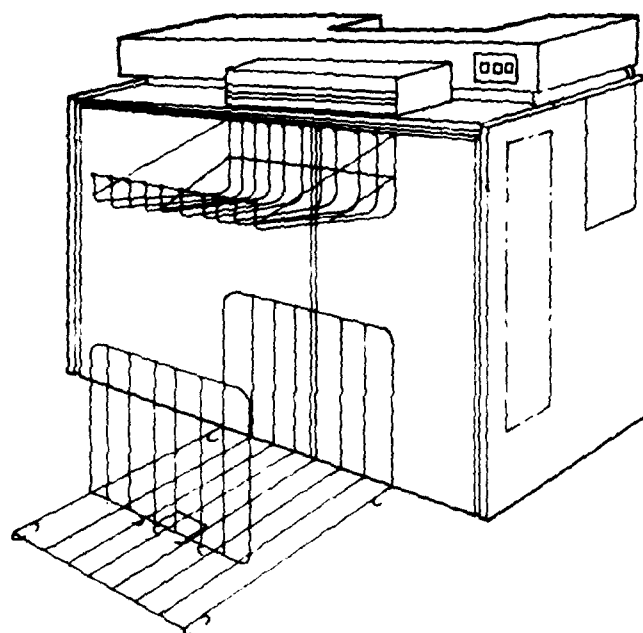
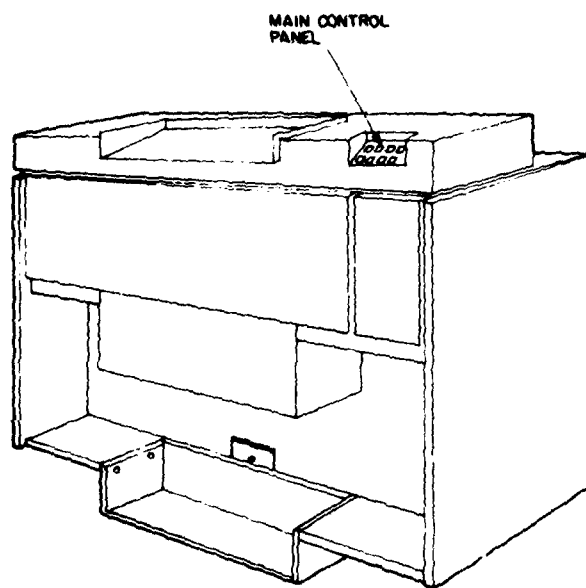


Figure 12 Disc Pack Drive



REAR VIEW



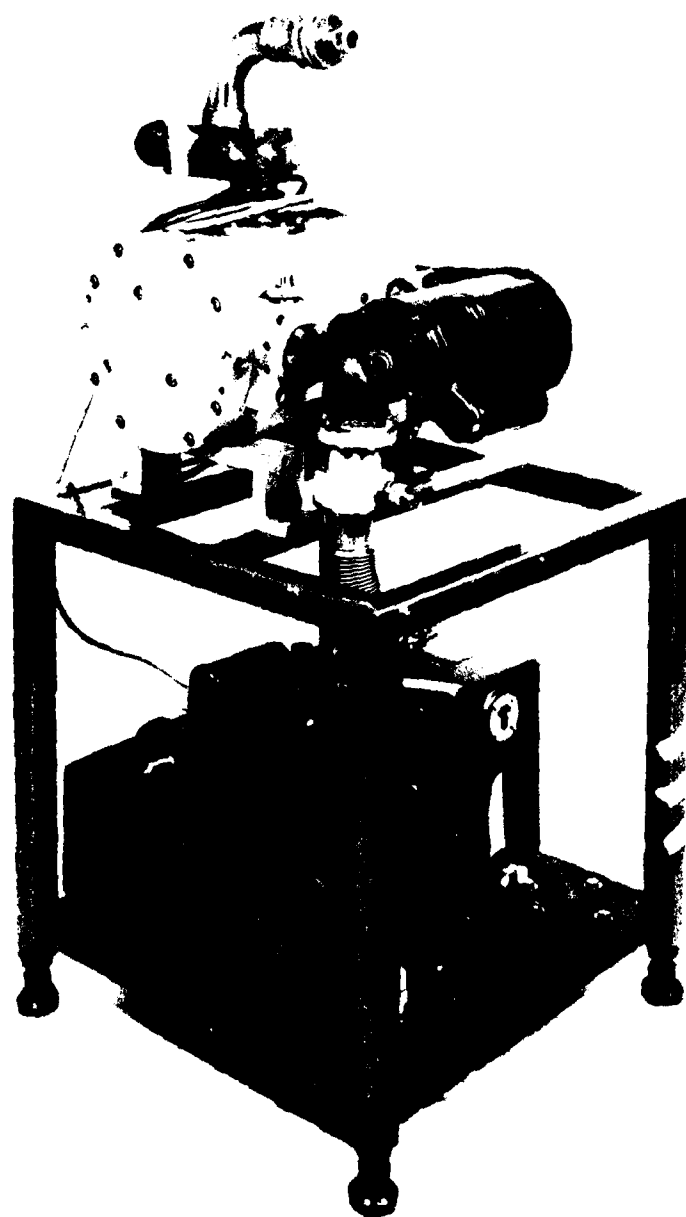
FRONT VIEW

7000-002

Figure 13 Line Printer

1-18

7902-4



01751

Figure 14 Vacuum Pumping Station

1-19

7902-4

4.0 SYSTEM ANALYSIS AND DESIGN REPORTS

Analysis and design efforts were required in critical areas to meet the Spatial Radiometer performance specifications. Table 1 outlines the performance requirements for the system. The following design and analysis reports are documented and will be included in Volume II of this final report. Excerpts of critical analysis criteria will be included in the following sections.

TABLE 1
SPATIAL RADIOMETER REQUIREMENT SUMMARY

| SPECIFICATION ITEM | REQUIREMENT |
|--------------------------------|---|
| Field of View | Near Field: $2^{\circ} \times 6^{\circ}$ Far Field: $4^{\circ} \times 6^{\circ}$ |
| IFOV | Near Field: 0.2° Far Field: 0.4° |
| Aperture Diameter | 3 inches |
| Wavelength | Classified |
| Frame Time | 0.5 - 1s |
| Noise Equivalent Radiance | Near Field: $<10^{-8} \text{w/cm}^2/\text{sr}$ Far Field: $<10^{-11} \text{w/cm}^2/\text{sr}$ |
| Signal Range | Near Field: Linear to $10^{-4} \text{w/cm}^2/\text{sr}$ Far Field: Linear to $10^{-8} \text{w/cm}^2/\text{sr}$ |
| Optical & Electrical Crosstalk | Combined Electrical & Optical Crosstalk $10^{-11} \text{w/cm}^2/\text{sr}$ for all res elms outside 1° of intense source (2×10^5 brighter than NER-worst case) |
| Size | Approx. max. of 12.5 inch diameter, 27 inches long |
| Electronics | $<1 \text{ ft.}^3$ |
| Optical Axis | Along 30-inch dimension |
| Weight System | $\leq 120 \text{ lbs.}$ |
| Input Power | Unregulated battery power 24 Vdc - 32 Vdc |
| Cryogenic Hold Time | 4 hours minimum |
| System Vibration Qualification | $0.1 \text{ g}^2/\text{Hz}$ 100-1000 Hz w/6db rolloff at 20 Hz and 2000 Hz |
| Signal Output | Digital bit stream pcm |
| Synchronizing Waveforms | 0.1° scan position accuracy |
| Housekeeping Data | Focal plane temperature Optical baffle temperature |
| Optical Components | Reflecting optics preferred |
| Off Axis Rejection | No NER degradation when sensor views to 60° SUN, 30° Earth |
| Internal Calibrator | Provide inflight calibrator |
| Instrument Calibration | Absolute Calibration $\pm 20\%$ |
| Operation Manual | Provide |
| Cryogenic Req't | Fill ports, orientation hold time, flight time |
| Cleanliness | Assembly requirement |

SECTION II

ELECTRONICS

SUMMARY

The following section is from the electronic design portion of the Spatial Radiometer System. The complete reports are in Volume II of the final report. The page numbers have been changed to conform to this report, however, section titles and figures are as written in each report.

PART A

REFERENCE DOCUMENT NUMBER 073076-0007

1.0 INTRODUCTION

The Spatial Radiometer electronics system consists of:

- 1) The Power Supply Assembly
- 2) The Electronics Assembly
- 3) The detectors, temperature sensors and electromechanical devices inside the sensor assembly.

The power supply accepts a 28DC input and provides all the necessary voltages to operate the Spatial Radiometer. The electronics assembly contains all the detector and signal processing electronics, and electronics to operate the electromechanical devices and sensors. Inside the sensor assembly there is a mirror scan mechanism, a blackbody calibration source, a hot wire calibration source, seven temperature sensors and forty (Hg,Cd)Te detectors. The following describes the signal processing. Figure 1.1 is a block diagram of the signal processing electronics from the detectors to the transmitter.

The first element is the Data Channel Electronics board. (Refer to the DCE description for details on the circuit operation.) The board contains ten identical pre-amp circuits to accommodate ten detectors. (There are four DCE boards per system). Each preamp is a low noise, high gain DC amplifier

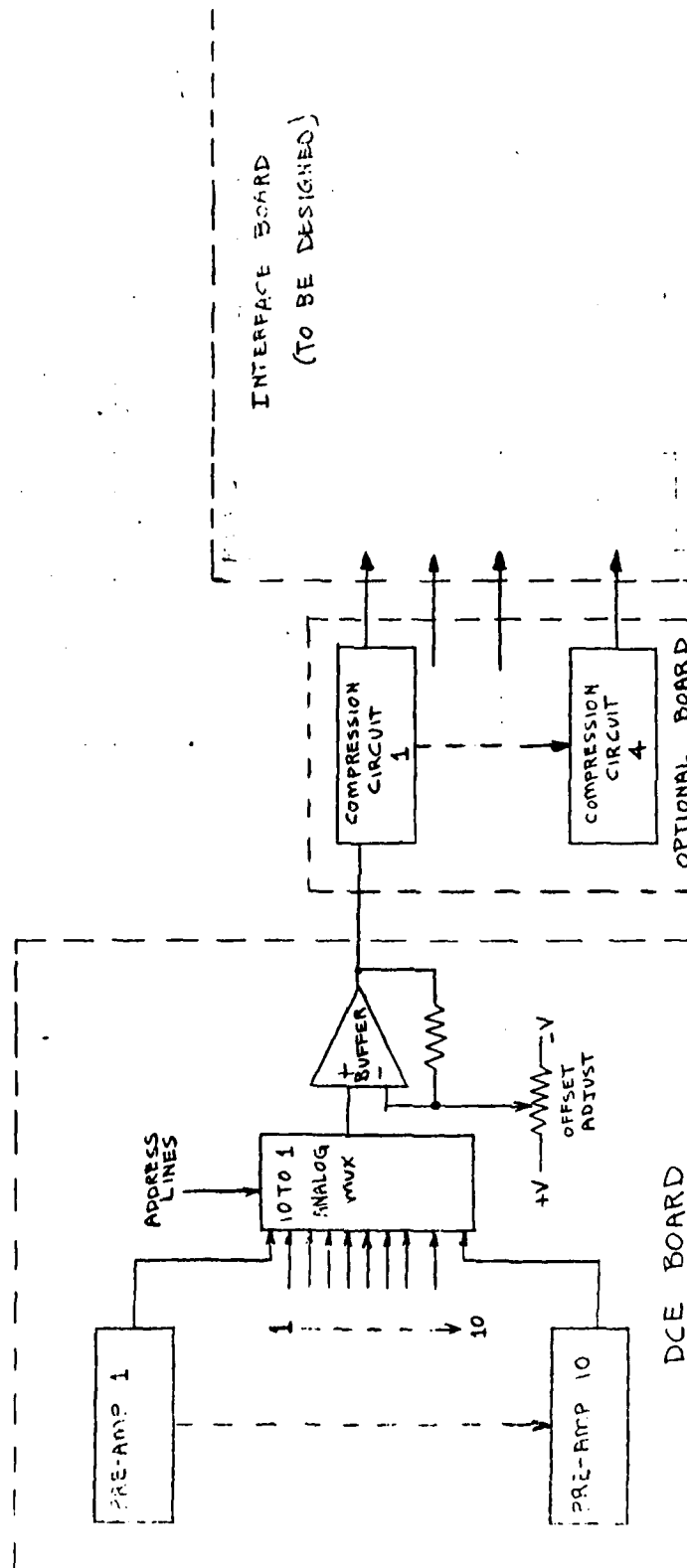


FIGURE 1.1.

with a 50Hz bandwidth. Each preamp has an adjustable detector bias voltage. All ten preamp outputs are multiplexed into a single output which is buffered. An offset adjustment is provided at the buffered output in order to raise the output 50mV for a zero signal input. This insures that all digitized noise samples are non-zero on the telemetry. The noise contribution by the preamp electronics (as measured in lab) is one-half of a quantizing level (level = 2.4mV) at a DC gain of 10^4 . Detector noise would add to this figure.

The second element in the signal processing electronics is the compression circuit. There are four such circuits: one for each of the four DCE board outputs. Each circuit provides a single gain break which is sufficient to accommodate the dynamic range of the detectors. This circuit could be deleted if the non-linear response of the detectors is sufficient to provide the necessary signal compression.

Each data channel is sampled at a 250Hz rate which is five times the 50Hz signal bandwidth of the DCE preamps.

The major areas of EMI are the power supply, cables and connectors. The power supply (manufactured by Powercube Corporation, Waltham, MA) meets MIL-STD-461 for both conducted and radiated EMI/RFI noise suppression. All connectors on the Spatial Radiometer assemblies conform to MIL-C-83723B and MIL-C-38999D. The cables connecting the power supply, electronics assembly and the sensor together meet MIL-STD-461 for EMI.

The interface board, which is to be designed, will multiplex the four DCE outputs (along with other analog data) into one output and do the A/D conversion. It will then transmit the digital bit stream in a compatible form to the transmitter.

2.0 DATA CHANNEL ELECTRONICS

2.1 Applicable Documents

Schematic No. 21016588
Detail No. 21016589
Assembly No. 21016590

2.2 Interfaces

2.2.1 Inputs

DETH1 - DETH10 Detector 1 - 10 Inputs
DSELO Data Multiplexer Address (LSB) - 6KHZ
DSEL1 Data Multiplexer Address - 3KHZ
DSEL2 Data Multiplexer Address - 1.5KHZ
DSEL3 Data Multiplexer Address (MSB) - 1.0KHZ
DCRS DC Restore Pulse

2.2.2 Outputs

DC OUT Multiplexed Data Output

2.2.3 Power (ma)

| | <u>Typical</u> | <u>Max</u> |
|---------|----------------|------------|
| +5 | 25 | 50 |
| +15VDC | 39 | 50 |
| -15VADC | 59 | 95 |
| -15VBDC | 68 | 69 |

2.3 Description

Figure 2.1 is a block diagram of the DCE board. The board contains ten preamp circuits, +12VDC and -11VDC low noise voltage regulators, an analog multiplexer and a buffer amplifier for the DC restore (DCRS) pulse.

A typical preamp circuit is shown on Honeywell Drawing 21012688, Sheet 1, in its entirety. (PREAMP 1). The input stage is a low noise transistor differential stage with the detector connected between DETH1 and DGNDA. The transistors are a dual pair within a single package to keep temperature drift at a minimum. The bias current for the detector is determined by the R106 select. The R107 select adjusts the offset so as to maintain linear circuit operation over the dynamic range of the detectors. Additional offset control is provided by the A-E connections on U101. U101 is a precision resistor network with a 5ppM/°C temperature tracking coefficient in order to keep temperature drift at a minimum. The C101 capacitor provides frequency stability.

The differential output is connected to an operational amplifier (AR101). The maximum overall DC gain of the preamp is 10^4 . The R109 select adjusts the gain to any desired value below 10^4 . C107 is selected to maintain a 50Hz signal bandwidth.

There is a positive feedback loop in the preamp via the R112 resistor. This in effect raises the input impedance of the preamp which minimizes the crosstalk between detectors by minimizing current flow in the ground line.

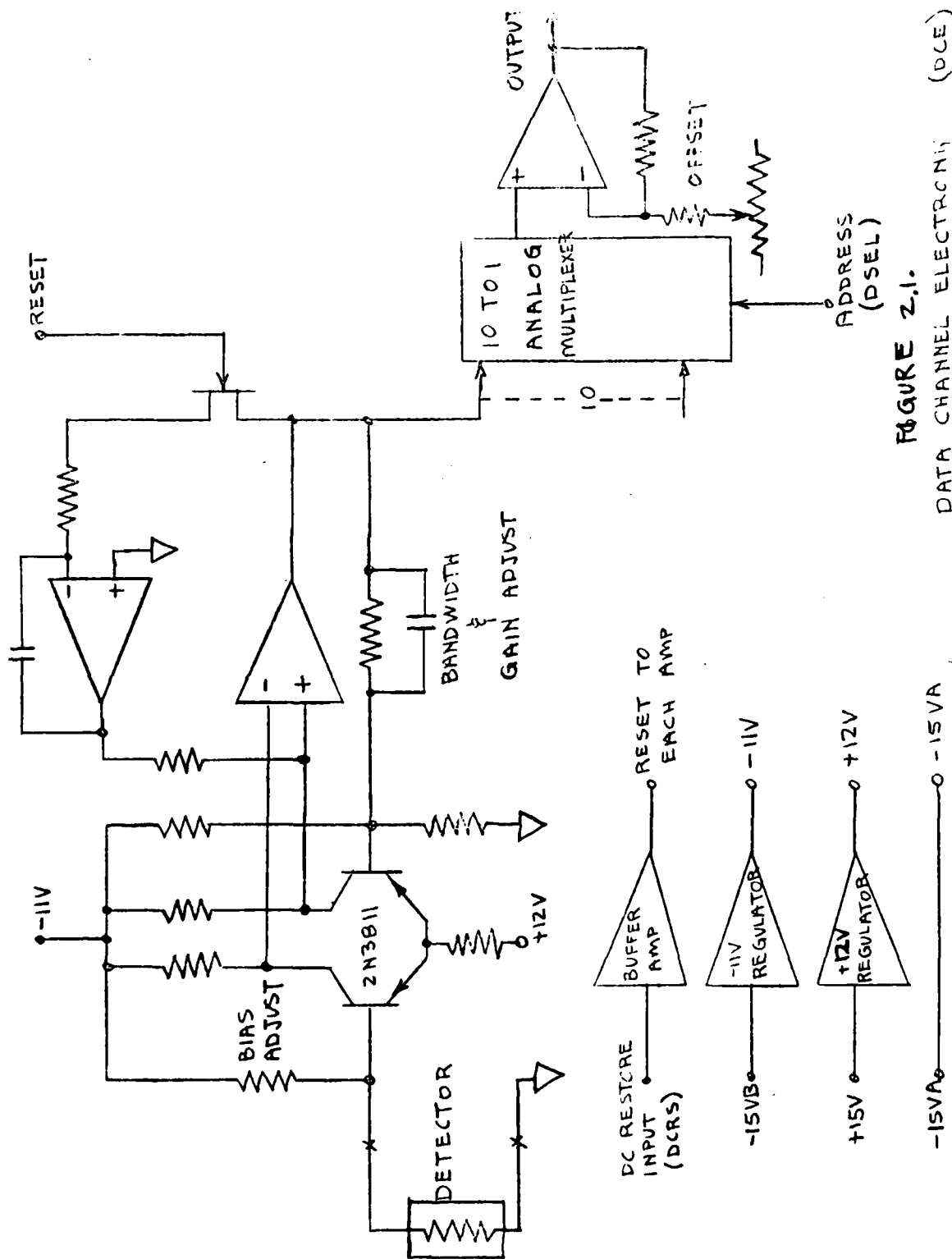


FIGURE 2.1.

DATA CHANNEL ELECTRONIC (DCE)

The output of AR101 is DC restored once every mirror scan (1 sec rate). This is accomplished by the feedback path composed of Q101, AR102 and associated passive components. The restoration occurs when the mirror is facing the cold stops. This restoration process minimizes the output drift, due to temperature effects, which is fairly large at high gain. Temperature drift effects look like $1/F$ noise. The total referred input noise of the preamp was measured in the laboratory using an engineering model PC board. The results are shown in Figure 2.2

All ten preamp outputs are connected to a 10 channel analog multiplexer (U1). The output of the multiplexer is buffered by an amplifier (AR3) with a gain of 2. The network composed of R12-R14 and CR4 provides a DC offset adjustment from 40mV to 70mV.

The low noise -11V regulator is composed of AR1, Q1 and associated passive components. The R2-R3 network divides down the -15V to -11V at the non-inverting input of AR1. AR1 drives Q1 which supplies the -11V current needed to operate all ten preamps. The +12V regulator has the configuration except no transistor drive because the +12V current requirements for the 10 preamps is low. The network composed of Q2 and associated components is a TTL to JFET level converter. The RSET signal drives 10 JFETS (one in each preamp).

The address lines for the multiplexers will be derived from the Logic board which shall be designed at a later time.

100 nV/√Hz

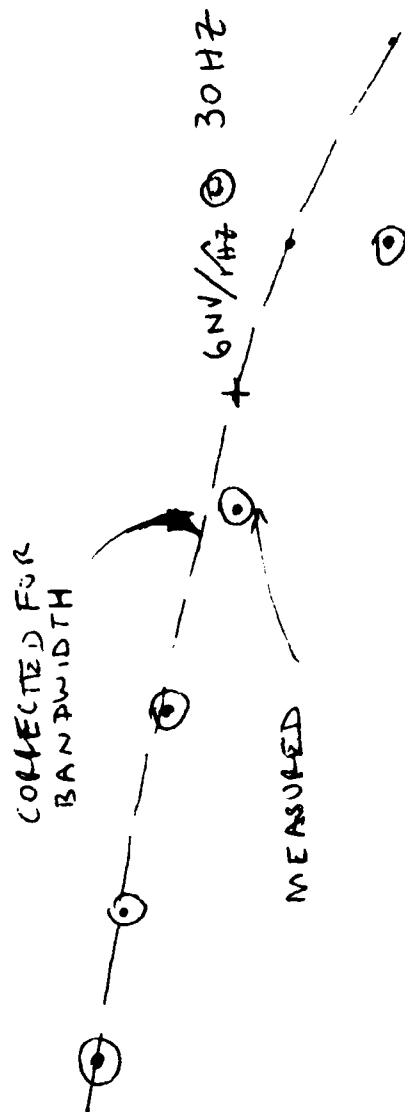
7902-4

FIG. 2.2.

REFERENCED INPUT NOISE
SPATIAL RADIOMETER AMP
AMP BANDWIDTH = 30 Hz

P.C. BOARD TEST - AVERAGE OF
FOUR CHANNELS

5/76



2-12

nV/√Hz

ALL

0CH2

3.0 HOUSEKEEPING

3.1 Applicable Documents

Schematic No. 21016517

Detail No. 21016518

Assembly No. 21016519

3.2 Interfaces

3.2.1 Inputs

| | |
|------------|---|
| TM1A, C | Motor Servo board temp. sensor |
| TM2A, C | Tank-top right front temp sensor |
| TM3A, C | Brazement - front temp sensor |
| TM4A, C | Focal plane temp sensor |
| TM5A, C | Brazement - top inside fore entrance temp sensor |
| TM6A, C | Tank - rear lower left temp sensor |
| TM7A, C | Tank - rear upper right temp sensor |
| TM8A, C | Scan mirror temp sensor |
| HKH4, HKL4 | Hot Wire Voltage |
| HKH5, HKL5 | Blackbody Heater Voltage |
| HKH6, HKL6 | Spare Input |
| HKH7, HKL7 | +28V Supply Monitor |
| HKH8, HKL8 | -15V _B Supply Monitor |
| CSEL2 | Multiplexer address line - 67.5HZ |
| CSEL1 | Multiplexer address line - 125HZ |
| CSEL0 | Multiplexer address line - 250HZ |

3.2.2 Outputs

| | |
|------|---------------------------------|
| TMOT | Multiplexed Temperature Output |
| TMSG | Return for TMOT Signal |
| HKOT | Multiplexed Housekeeping Output |
| HKSG | Return for HKOT Signal |

3.2.3 Power (Ma)

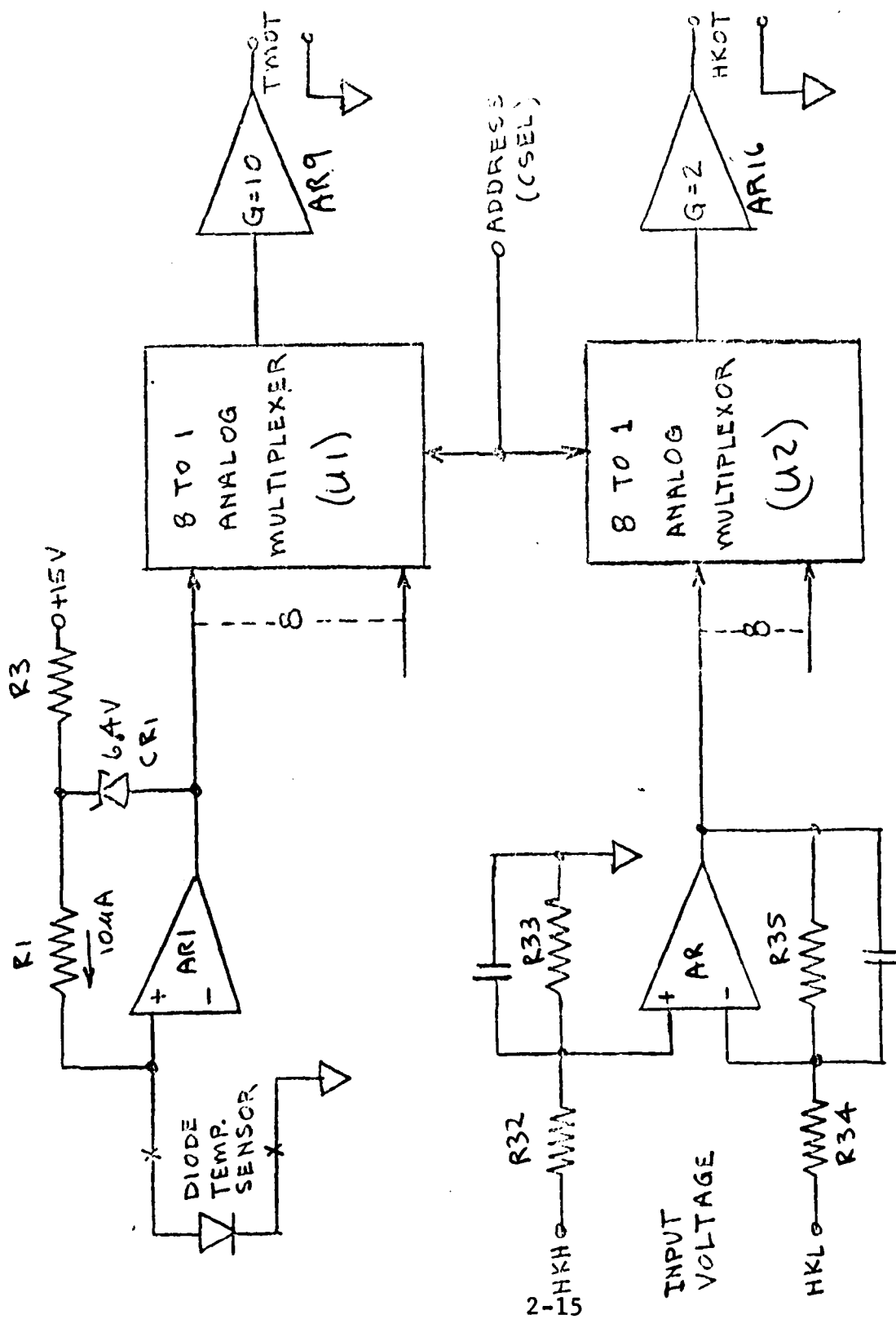
| | <u>Typical</u> | <u>Maximum</u> |
|------|----------------|----------------|
| +5 | 50 | 70 |
| +15 | 53 | 69 |
| -15A | 48 | 64 |

3.3 Description

Figure 3.1 is a block diagram of the Housekeeping board. Only two distinct circuits are shown.

The upper circuit is typical of circuits 1-8 on schematic No. 21016517. Circuit 1 is used as a reference in the following description.

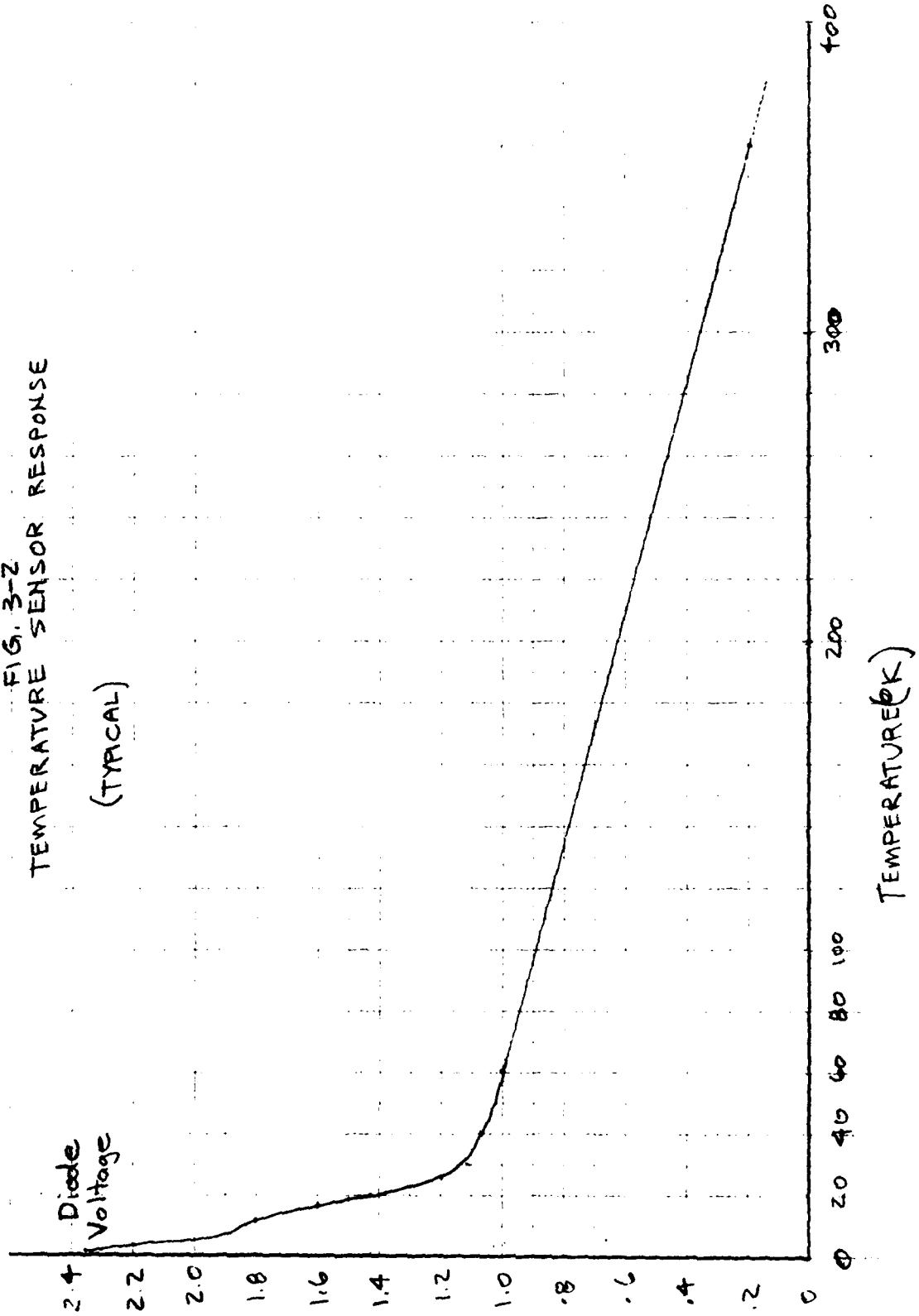
Diode CR1 and resistor R1 provide a constant current of 10mA to the silicon temperature sensor connected between TM1A and TM1C. The diode voltage is proportional to temperature and is shown in Figure 3.2. The voltage is buffered by AR1 (unit gain) and is transmitted to an 8-to-1 analog multiplexer (UL). The multiplexer output is buffered by a X2 amplifier (AR9).



HOUSEKEEPING BOARD
FIGURE 3.1.

FIG. 3-2
TEMPERATURE SENSOR RESPONSE

(TYPICAL)



2-16

The lower circuit on Figure 3.1 is typical of circuit 9-11, 13, 14. Circuit 9 is used as a reference in the following description.

Circuit 9 is a differential input amplifier whose gain is adjusted by selects R32 and R34. The output of AR11 is transmitted to an 8-to-1 analog multiplexer (U2) whose output is buffered by a X3 gain amplifier (AR16). The inputs to circuits 9-11, 13, 14 are listed in Table 3.1 along with nominal voltages and overall gains. There are three additional dedicated inputs to the U2 multiplexer - 1) 5V supply (input 12), 2) +15V supply (input 11), 3) -15V supply (input 10). Both the +5V and +15 go through dividers. The -15V supply goes through an inverter (AR10) with a gain of .11.

The multiplexer address lines shall be derived from the Logic board which shall be designed at a later time.

TABLE 3.1

| <u>Circuit No.</u> | <u>Input</u> | <u>Nominal Input Voltage</u> | <u>Overall Gain</u> |
|--------------------|--------------------------|------------------------------|---------------------|
| 9 | Hot Wire Voltage | .4 | 3 |
| 10 | Blackbody Heater Voltage | 5 | 1 |
| 11 | Spare | 28 | 3 |
| 13 | +28V Supply | -15 | .3 |
| 14 | -15V _B Supply | | .3 |

4.0 MOTOR SERVO

4.1 Applicable Documents

Schematic No. 21016591

Detail No. 21016592

Assembly No. 21016593

4.2 Interfaces

4.2.1 Inputs

| | |
|-------|--|
| BBT1H | Blackbody Thermistor Feedback HI |
| BBT1L | Blackbody On Command Feedback LO |
| CBBON | Blackbody On Command |
| CCAL | Calibrate Command (hot wire) |
| CSSEN | Enable Mirror Motor Single Step Command |
| CSP2 | Spare Input Command |
| COMR | Return for all Commands |
| DCRS | D.C. Restore Pulse (1Hz) |
| CRST | Calibrate Reset Pulse (hot wire) |
| B1N4 | Input to binary subcom |
| INCM | Increment Mirror Pulse |
| UPDN | Mirror Direction Control |
| MCEN | Enable Mirror Control |
| MNULL | Mirror Null Position Pulse |
| SSCLH | Single Step Command to Mirror |
| VDTH | Input From RVDT Secondary HI |
| VDTL | Input From RVDT Secondary LO |

| | |
|-------|---|
| DSELO | 6KHZ Square Wave to Drive RVDT Primary |
| COVH | Front Cover Switch Indicator HI |
| COVL | Front Cover Switch Indicator LO |
| HTWA | Hot Wire Calibrator HI |
| HTWB | Hot Wire Calibrator LO |

4.2.2 Outputs

| | |
|--------|--|
| CSP2F | Filtered Spare Command |
| BBH1 | Blackbody Heater HI |
| BBHLO | Blackbody Heater LO |
| ABIN | Analog Output From Binary Subcom (D/A) |
| ABINR | Return from ABIN |
| MTEMPH | Temp Sensing Diode On Servo Board HI |
| MTEMPL | Temp Sensing Diode On Servo Board LO |
| MNULLB | Null Signal To Mirror (buffered) |
| MPMH | Mirror Position Monitor HI |
| MPML | Mirror Position Monitor LO |
| VSCAN | Mirror Position Monitor to AGE HI |
| VSCR | Return for VSCAN |
| VDTA | Output Drive to RVDT Primary HI |
| VDTB | Output Drive to RVDT Primary LO |

4.2.3 Power (Ma's)

| | <u>Typical</u> | <u>Max</u> |
|-----|----------------|------------|
| +5 | 137 | 165 |
| +15 | 200 | 280 |
| -15 | 83 | 103 |

2-20

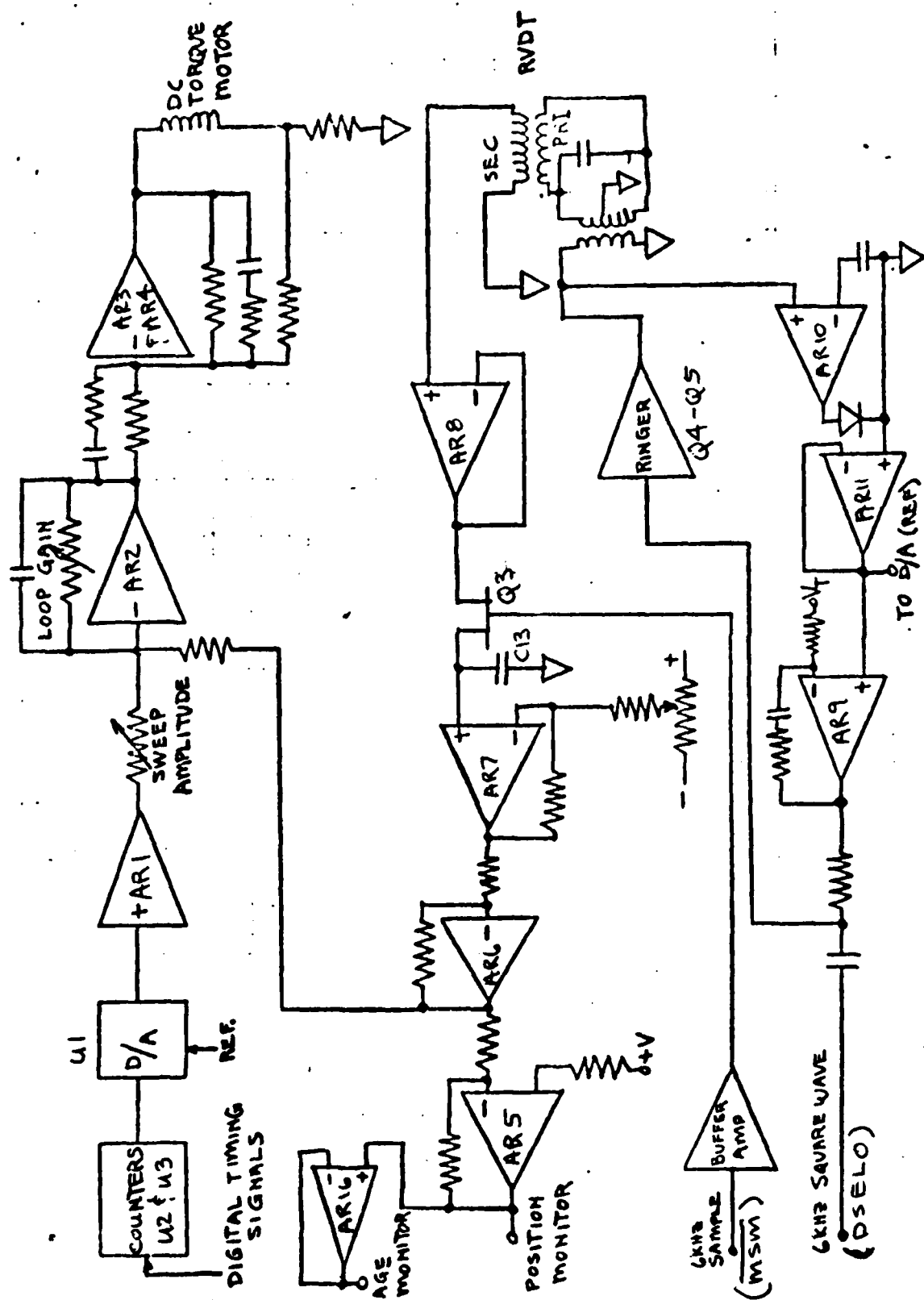
4.3 Description

The board is functionally divided into five separate circuits - 1) Mirror motor servo, 2) Blackbody controller, 3) Hot wire controller, 4) Command input buffers and 5) D/A converter for encoding digital information into analog form.

Figure 4.1 is a block diagram of the mirror servo electronics. Page 2 of Honeywell Drawing No. 21016591 shows the complete circuit. The analog reference waveform used to drive the mirror motor is derived from a D/A converter (U1) and two digital counters (U2, U3). The two counters are driven by a series of timing pulses (INCM, UPDN, MCEN, MVLL, SSCLH) from the Logic board. (to be designed). The counter outputs drive the D/A converter which produces the desired analog reference waveform at AR1. By properly programming the above five timing pulses, a number of different waveforms can be obtained to drive the mirror. The amplitude of the reference waveform and the thus the amplitude of the mirror motor sweep is adjusted by the R5 select resistor.

The reference waveform and the motor position information derived from the RVDT (explained below) are summed at AR2 and an error signal, proportional to the difference, is produced at AR2. AR2 also adjusts the loop gain of the servo. A lag compensation network (R11, R12, C4, C5) maintains loop stability at high frequencies. A final drive stage composed of AR3 and AR4 provide the necessary current gain to drive the motor and more frequency selection. The motor is an Aeroflex brushless torque No. V18-44.

FIGURE 4-1.
MIRROR SERVO ELECTRONICS



A rotationally variable differential transformer (RVDT) is used to provide positional feedback information. A 6KHZ square wave (DSELO) is fed into an oscillator circuit composed of AR9 - AR11, Q4 and Q5. The resulting 6KHZ sine wave applied to the T1 transformer provides a balanced drive to the RVDT primary (VDTA, VDTB). This 6KHZ sine wave is coupled into the RVDT secondary and modulated by the mirror motor movement at a 1HZ rate. The modulated 6KHZ sine wave is fed back to the circuit (VDTH, VDTL) and the 1HZ information extracted by the sample and hold composed of Q3 and C13. The sampling JFET (Q3) is pulsed by Q2 and associated components. A 6KHZ sampling pulse (\overline{MSM}) which is synchronuous with DSELO drives the pulsing network. The \overline{MSM} pulse is derived on the Logic board (to be designed) and its phase relative to the DSELO can be changed to compensate for phase shifts in the oscillator and RVDT. AR7 and AR6 provide further gain and frequency adjustments. Buffered outputs of the position are provided through AR5 and AR16.

For test purposes a single step capability for the mirror has been provided. By using the command, Single Step Enable (CSSEN), U6 gates out all timing pulses to the counters U2 and U3 and gates in the single step command (SSCLH). Each time the SSCLH line is pulsed at the AGE panel the motor rotates one increment. Each increment is equal to the total angular rotation of the motor divided by 256.

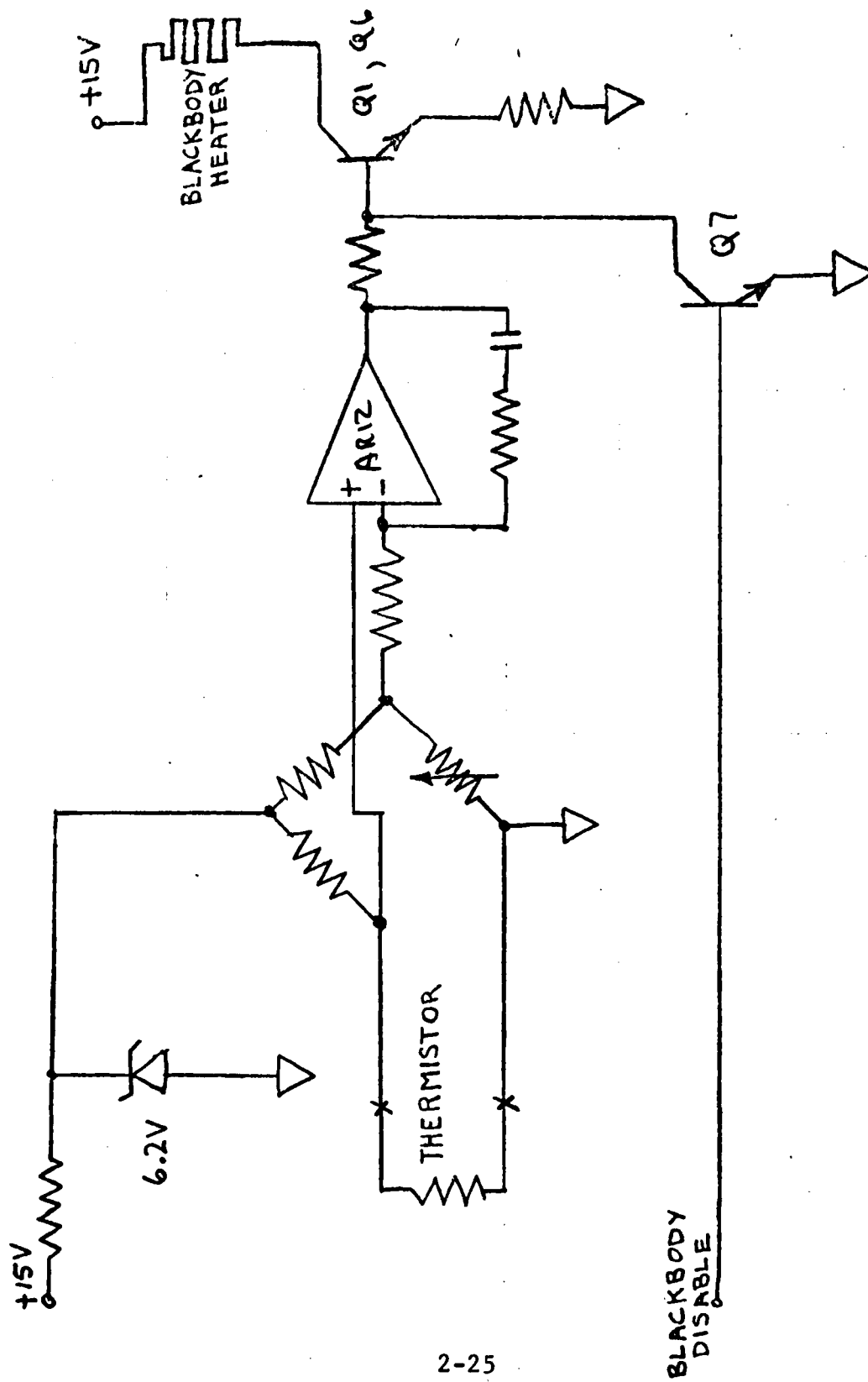
Refer to the Scan Mirror Design Report (Spatial Radiometer 032476-0004) for design analysis of servo.

Figure 4.2 shows a block diagram of the Blackbody Controller. The entire circuit is shown on Sheet 1 of 21016591.

The feedback thermistor is located in one leg of the bridge composed of R58, R59, R60 and R61. It drives the non-inverting input of AR12. The desired control point is set up at the inverting input by appropriate selection of R62. The lag network (R63-C35) around AR12 maintains frequency stability and high DC gain for high accuracy temperature control. Q1 and Q6 provide power gain. Q7 turns the blackbody on or off by ungrounding or grounding the bases of Q1 and Q6.

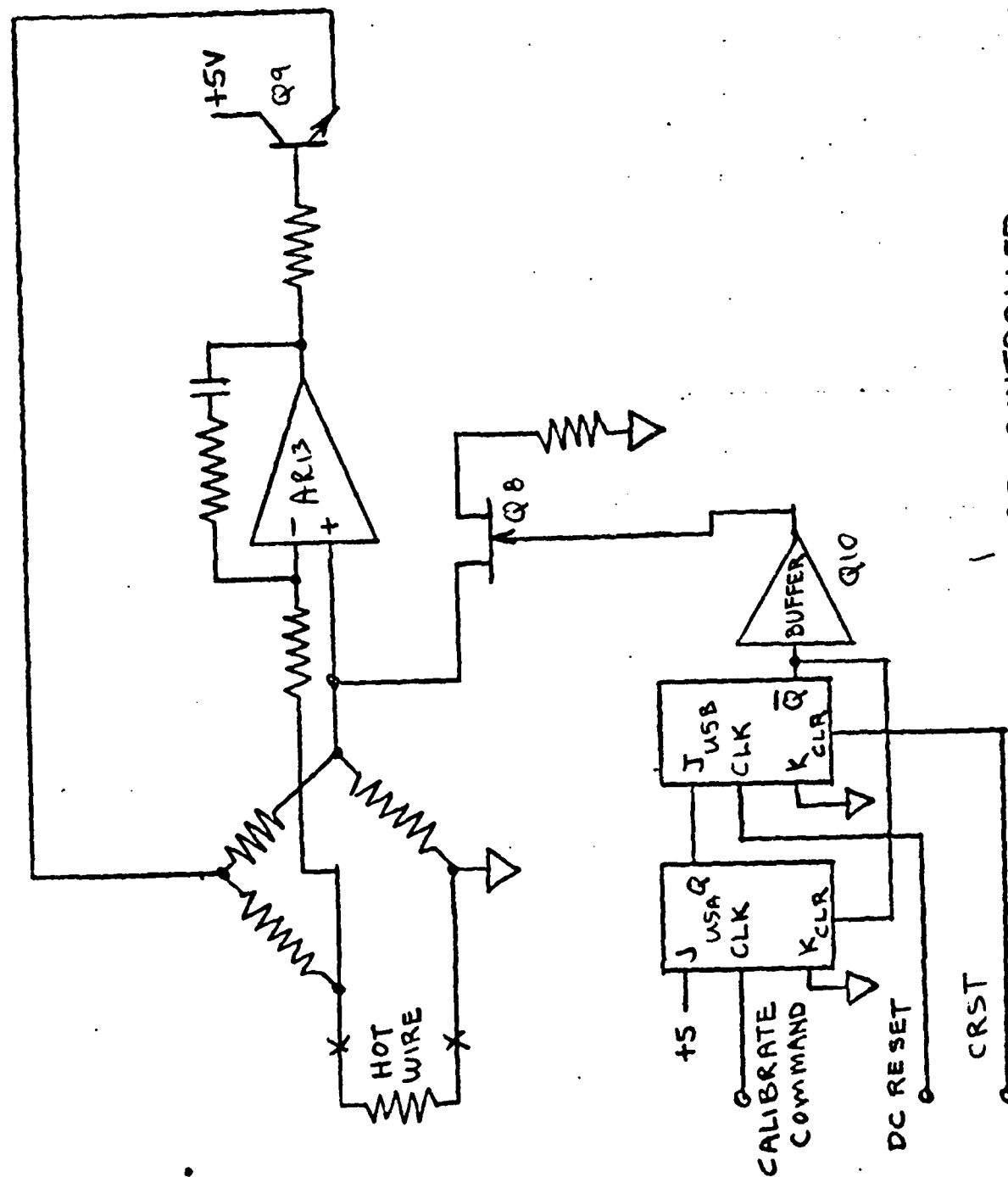
Figure 4.3 shows the block diagram of the Hot Wire Controller, Sheet 1 of 21016591 shows a complete circuit.

The Hot Wire is a piece of tungsten wire (about 10 25°C) and is used as a photon source. The wire is located in one leg of the bridge composed of R68 - R72, R78. It drives the inverting input of AR13. AR13 drives Q9 which regulates the current to the Hot Wire. The R74 - C27 lag network keeps the loop frequency stable and provides high DC gain for temperature accuracy. The normal operating temperature of the hot wire is determined by the R72 select since the Q8 JFET is normally on. If the Q8 JFET is turned off the operating temperature is elevated to a value determined by the R78 - R72 combination. The JFET is under the control of Q10, U5 and the associated input signals. (DCRS, CRST, CCAL). When the high temperature is desired the CCAL command is executed and at the proper time, synchronous with DCRS, the JFET is turned off and the temperature level goes up. The JFET is turned



BLACKBODY CONTROLLER

FIGURE 4.2



HOT WIRE CONTROLLER
FIGURE 4.3

back on again when CRST occurs which is about .5 secs. after DCRS.

The elevated temperature operation is used as a calibration point where-as the lower temperature operation is used as an optical bias. The low to high temperature transition takes about 100M secs. and the high to low transition takes about 50M secs.

The command input buffers are shown on Sheet 1 of 21016591. The inputs (CBBON, CCAL, CSSEN and CSP2) are relay switch closures to ground (COMR). The switch contact bounce is filtered by the R40-C43 (typical) network and buffered by the comparator (LM139-AR17). Table 4.1 list the four commands.

The binary encoder is also shown on Sheet 1 of 21016591. It consists of a D/A converter which forms discrete analog voltages at the output (ABIN) for certain digital inputs. Each digital input combination has a distinct analog output associated with it. The output of the binary encoder in volts (ABIN) is given by the following expression:

$$\begin{aligned} ABIN = & .2004 + (A_9 \times .3137) + (A_8 \times .6275) + (A_7 \times 1.2549) \\ & + (A_6 \times 2.5098) + (A_5 \times 5.0196). \end{aligned}$$

where $A_9 - A_5$ represents the digital value (1 or 0) of the inputs at pins 9 - 5, respectively, of U7.

TABLE 4.1

| | |
|-------|--|
| CBBON | Turns Blackbody on |
| CCAL | Causes Hot Wire to elevate to higher temperature value |
| CSSEN | Enables single step function of mirror motor, disables auto scanning |
| CSP2 | Spare command |

5.0 POWER SUPPLY

The Spatial Radiometer power supply is a modular supply made up of eight modules packaged in a 3.5" x 4.6" x 1.55" assembly. For ease of installation, this assembly has been packaged inside another container. The entire assembly is shown in Honeywell Drawing No. 21016526.

Figure 2 in Honeywell Drawing 21016523 shows a block diagram of the power supply. The 8111/FTA1 module is a special purpose EMI filter. The two 20sp50 modules (S1 and S2) are switching pre-regulators that drive the frequency generator module 20G90W40. This module drives the transformer isolated output regulators 15TR13, 15TRC10, and 5TR30. The Honeywell Drawing No. 21016523 gives all pertinent facts about the power supply.

PART B

REFERENCE DOCUMENT NUMBER 021777-0018

1.0 LOGIC

1.1 Applicable Documents

Schematic No. 21013288

Detail No. 21013289

Assembly No. 21013290

1.2 Interface

1.2.1 Inputs

SPIN - Spare Input

1.2.2 Outputs

| | |
|--------------|------------------------------|
| PRPCM | Programmed PCM |
| FYNC | Frame Start SyncPulse |
| EOFP | End of Frame Pulse |
| SUFP | Subframe Sync Pulse |
| OSW | Output Switch Select |
| MNULL | Mirror Null Position Pulse |
| INCM | Increment Mirror Pulse |
| UPDN | Mirror Direction Control |
| DCRS | DC Restore Pulse |
| MCEN | Enable Mirror Control |
| BCLK | 144KHZ Data Bit Clock |
| <u>SCONV</u> | A/D Converter Trigger |
| <u>MSM</u> | Mirror Position Sample Pulse |
| <u>B12</u> | Data Bit 12 |

| | |
|-------|------------------------------------|
| MXAD0 | LSB Interface Multiplexer Address |
| MXAD1 | Interface Multiplexer Address |
| MXAD2 | MSB Interface Multiplexer Address |
| DSEL0 | 6KHZ LSB Data Frame Word Counter |
| DSEL1 | 3KHZ LSB Data Frame Word Counter |
| DSEL2 | 1.5KHZ LSB Data Frame Word Counter |
| DSEL3 | 1KHZ Data Frame Word Counter |
| C500 | 500HZ |
| C250 | 250HZ MSB Data Frame Word Counter |
| CSEL0 | 125HZ LSB |
| CSEL1 | 62.5HZ Subcom Data Counter |
| CSEL2 | 31.25HZ MSB |
| DADD0 | LSB Data Word Select Line |
| DADD1 | Data Word Select Line |
| DADD2 | Data Word Select Line |
| DADD3 | Data Word Select Line |
| DADD4 | Data Word Select Line |
| DADD5 | Data Word Select Line |
| DADD6 | Data Word Select Line |
| DADD7 | Data Word Select Line |
| DADD8 | MSB Data Word Select Line |
| FSFS | Frame / Subframe Rate Select |
| SPIN | Spare Input |

1.3 Description

The Logic board provides data formatting and all required timing pulses for normal system operation. The Logic board is a hybrid 1 bit microprocessor consisting of discrete IC's. Logic operations are programmed from instructions stored in a 512 x 8 PROM utilizing a 6 instruction set. See Figure 1.1. Logic operations are obtained by an output of "1" or "0" on any of 16 outputs from the result of sensing any of 32 inputs. Instructions are coded in 8 bit words and are sequentially executed except for skip, branch or wait "true" instructions. Instructions are single or double byte and are executed at a 1.152MHZ rate. Input and Output lines are selected by the address field of the least significant bits of the IO instruction. The second byte of a double byte instruction is reserved for a 8 bit program PROM address. Each instruction cycle has 4 clock phases ($\overline{T1}$, $\overline{T2}$, $\overline{T3}$, $\overline{T4}$).

At $\overline{T1}$ "0" an instruction from the Program PROM (U4) is loaded into the Instruction Register (U5). See Figure 1.6. The 5 address lines from the Instruction Register control the data source input by an 8/1 multiplexer (U15) and 8 4/1 multiplexers on the Interface board. The 2 LSB bits address the 4/1 multiplexers while the next 3 bits selects a particular 4/1 multiplexer. Outputs are generated by 2 addressable latches (U14, 15) which are addressed from the 3 LSB's of the instruction word.

At $\overline{T2}$ "0" a sensed data bit from the multiplexed inputs is stored in a JK FF (U12A). The PC (Program Counter U3, and U11) is incremented and the next instruction or address is loaded into the B Register (U1, and U10).

At $\overline{T3}$ "0" the instruction is initiated by a Control PROM (U6). The OP code bits of the Instruction Register and feedback from the sensed input line stored in (U12A) address the Control PROM setting a control state for the duration of $\overline{T3}$. See Figure 1.2. The M Register (U2 and U9) is loaded directly from the Program PROM as the second byte of an LDM instruction. If a branch "true" instruction is initiated a second byte address is loaded from the B Register to the Program Counter. When a branch instruction "false" or skip instruction "true" is executed the Program Counter is again incremented. If a wait "true" instruction is executed the Program Counter is decremented. Branch instructions are "page" limited to the upper or lower half of the Program PROM due to the 8 bit address size. The JMPM instructions are not page limited since JMPMH or JMPML is possible. The H or L suffix sets or clears a "page" FF (U8B). The JMPM control (U8A) FF extends the active time of the tristate M Register by another clock interval to assure M data is stable during the Program Counter load interval.

A crystal controlled clock oscillator (U29) increments a countdown chain (U30, 12, 13, 17, 20, 21, 22, 23, 24 and 25). See Figure 1.5. The timing PROM (U31) is addressed by a binary counter (U30) which generates the 4 phase clocks pulses and $\overline{\text{CINC}}$. The contents of the timing PROM is a cyclical code modified by 2 address lines $\overline{\text{INC}}$ and $\overline{\text{LDM}}$. See Figure 1.3. Another timing PROM (U18) is addressed by the modulo 24 count lines from U12B and U17 in the counter chain. The PROM generates $\overline{\text{B12}}$, $\overline{\text{SCONV}}$ and $\overline{\text{MSM}}$. See Figure 1.4. The 4 8/1 Input Multiplexers (U32, 33, 34 and 35) input the counter lines to the processor for synchronized PCM generation. See Figure 1.7.

The program begins at location 0 and continues until a 4MS data frame is generated. When complete an interrupt pulse CL (U28) is triggered and clears the program counter to begin another data frame.

BASIC INSTRUCTION SET

| | |
|------|---|
| WAIT | Wait if line selected is "true". |
| SKIP | Skip next instruction if line selected is "true". |
| CNDB | Branch to second byte address if line selected is "true". |
| OUT | Output a "0" or "1" on line selected. |
| LDM | Load 2nd byte in M Register. |
| JMPM | Jump to M address in hi or lo page. |

Figure 1.1

| ADDRESS | OUTPUTS | | | | | | | | | |
|---------|---------|---|---|---|---|---|---|---|-------|-----------|
| | 1 | 2 | 3 | 4 | 5 | 6 | 7 | 8 | | |
| 1 | 1 | 0 | 1 | 1 | 1 | 1 | 1 | X | WAITL | L TRUE |
| 2 | 1 | 1 | 1 | 1 | 1 | 1 | 1 | X | WAITH | |
| 3 | 0 | 1 | 1 | 1 | 1 | 1 | 1 | X | SKIPL | |
| 4 | 1 | 1 | 1 | 1 | 1 | 1 | 1 | X | SKIPH | |
| 5 | 1 | 1 | 1 | 0 | 1 | 1 | 1 | X | CNDBL | |
| 6 | 0 | 1 | 1 | 1 | 1 | 1 | 1 | X | CNDBH | |
| 7 | 1 | 1 | 0 | 1 | 1 | 1 | 1 | X | OUTA | |
| 8 | 1 | 1 | 1 | 1 | 0 | 1 | 1 | X | LDM | |
| 9 | 1 | 1 | 1 | 1 | 1 | 1 | 1 | X | WAITL | H TRUE |
| 10 | 1 | 0 | 1 | 1 | 1 | 1 | 1 | X | WAITH | |
| 11 | 1 | 1 | 1 | 1 | 1 | 1 | 1 | X | SKIPL | |
| 12 | 0 | 1 | 1 | 1 | 1 | 1 | 1 | X | SKIPH | |
| 13 | 0 | 1 | 1 | 1 | 1 | 1 | 1 | X | CNDBL | |
| 14 | 1 | 1 | 1 | 0 | 1 | 1 | 1 | X | CNDBH | |
| 15 | 1 | 1 | 0 | 1 | 1 | 1 | 1 | X | OUTA | |
| 16 | 1 | 1 | 1 | 1 | 0 | 1 | 1 | X | LDM | |
| 17 | 1 | 0 | 1 | 1 | 1 | 1 | 1 | X | WAITL | L TRUE |
| 18 | 1 | 1 | 1 | 1 | 1 | 1 | 1 | X | WAITH | |
| 19 | 0 | 1 | 1 | 1 | 1 | 1 | 1 | X | SKIPL | |
| 20 | 1 | 1 | 1 | 1 | 1 | 1 | 1 | X | SKIPL | |
| 21 | 1 | 1 | 1 | 0 | 1 | 1 | 1 | X | CNDBL | |
| 22 | 0 | 1 | 1 | 1 | 1 | 1 | 1 | X | CNDBH | |
| 23 | 1 | 1 | 1 | 1 | 1 | 1 | 0 | X | OUTB | |
| 24 | 1 | 1 | 1 | 0 | 1 | 0 | 1 | X | JMPM | |
| 25 | 1 | 1 | 1 | 1 | 1 | 1 | 1 | X | WAITL | H TRUE |
| 26 | 1 | 0 | 1 | 1 | 1 | 1 | 1 | X | WAITH | |
| 27 | 1 | 1 | 1 | 1 | 1 | 1 | 1 | X | SKIPL | |
| 28 | 0 | 1 | 1 | 1 | 1 | 1 | 1 | X | SKIPH | |
| 29 | 0 | 1 | 1 | 1 | 1 | 1 | 1 | X | CNDBL | |
| 30 | 1 | 1 | 1 | 0 | 1 | 1 | 1 | X | CNDBH | |
| 31 | 1 | 1 | 1 | 1 | 1 | 1 | 0 | X | OUTB | |
| 32 | 1 | 1 | 1 | 0 | 1 | 0 | 1 | X | JMPM | |

INC DEC AOUT LOAD LDM M BOUT

X = DON'T CARE

FIGURE 1.2

U6 - INSTRUCTION CONTROL PROM
2-37

| ADDRESS | OUTPUTS | | | | | | | |
|---------|---------|---|---|---|---|---|---|---|
| | 1 | 2 | 3 | 4 | 5 | 6 | 7 | 8 |
| 1 | | | | 1 | 1 | 1 | 1 | 1 |
| 2 | | | | 1 | 1 | 1 | 1 | 1 |
| 3 | | | | 1 | 1 | 1 | 1 | 1 |
| 4 | | | | 1 | 1 | 1 | 1 | 1 |
| 5 | | | | 1 | 1 | 1 | 1 | 1 |
| 6 | | | | 1 | 1 | 1 | 1 | 1 |
| 7 | | | | 1 | 1 | 1 | 1 | 1 |
| 8 | | | | 1 | 1 | 1 | 1 | 1 |
| 9 | | | | 1 | 1 | 1 | 1 | 1 |
| 10 | | | | 1 | 1 | 1 | 1 | 1 |
| 11 | | | | 1 | 1 | 1 | 1 | 1 |
| 12 | | | | 1 | 1 | 1 | 1 | 1 |
| 13 | | | | 1 | 1 | 1 | 1 | 1 |
| 14 | | | | 1 | 1 | 1 | 1 | 1 |
| 15 | | | | 1 | 1 | 1 | 1 | 1 |
| 16 | | | | 1 | 1 | 1 | 1 | 1 |
| 17 | | | | 1 | 1 | 1 | 1 | 1 |
| 18 | | | | 1 | 1 | 1 | 1 | 1 |
| 19 | | | | 1 | 1 | 1 | 1 | 1 |
| 20 | | | | 1 | 1 | 1 | 1 | 1 |
| 21 | | | | 1 | 1 | 1 | 1 | 1 |
| 22 | | | | 1 | 1 | 1 | 1 | 1 |
| 23 | | | | 0 | 1 | 0 | 1 | 1 |
| 24 | | | | 1 | 1 | 1 | 1 | 1 |
| 25 | | | | 1 | 1 | 1 | 1 | 1 |
| 26 | | | | 1 | 1 | 1 | 1 | 1 |
| 27 | | | | 0 | 1 | 0 | 1 | 1 |
| 28 | | | | 1 | 1 | 1 | 1 | 1 |
| 29 | | | | 0 | 1 | 1 | 1 | 0 |
| 30 | | | | 1 | 1 | 1 | 0 | 1 |
| 31 | | | | 1 | 1 | 0 | 1 | 1 |
| 32 | | | | 1 | 0 | 1 | 1 | 1 |

LDM

INC

T1

T2

T3

T4

CINC T4 T3 T2 T1

FIGURE 1.3
U31 - TIMING PROM
2-38

| ADDRESS | OUTPUT | | | | | | | |
|---------|--------|---|---|---|---|---|---|---|
| | 1 | 2 | 3 | 4 | 5 | 6 | 7 | 8 |
| 1 | | | 1 | 1 | 1 | | | |
| 2 | | | 1 | 1 | 1 | | | |
| 3 | | | 1 | 1 | 1 | | | |
| 4 | | | 1 | 1 | 1 | | | |
| 5 | | | 1 | 1 | 1 | | | |
| 6 | | | 1 | 1 | 1 | | | |
| 7 | | | 1 | 1 | 1 | | | |
| 8 | | | 1 | 1 | 1 | | | |
| 9 | | | 1 | 1 | 1 | | | |
| 10 | | | 1 | 1 | 1 | | | |
| 11 | | | 1 | 1 | 1 | | | |
| 12 | | | 1 | 1 | 1 | | | |
| 13 | | | 1 | 1 | 1 | | | |
| 14 | | | 1 | 1 | 1 | | | |
| 15 | | | 1 | 1 | 1 | | | |
| 16 | | | 1 | 1 | 1 | | | |
| 17 | | | 1 | 1 | 1 | | | |
| 18 | | | 1 | 0 | 0 | | | |
| 19 | | | 1 | 1 | 1 | | | |
| 20 | | | 1 | 1 | 1 | | | |
| 21 | | | 1 | 1 | 1 | | | |
| 22 | | | 1 | 1 | 1 | | | |
| 23 | | | 1 | 1 | 1 | | | |
| 24 | | | 0 | 1 | 1 | | | |
| 25 | | | 1 | 1 | 1 | | | |
| 26 | | | 1 | 1 | 1 | | | |
| 27 | | | 1 | 1 | 1 | | | |
| 28 | | | 1 | 1 | 1 | | | |
| 29 | | | 1 | 1 | 1 | | | |
| 30 | | | 1 | 1 | 1 | | | |
| 31 | | | 1 | 1 | 1 | | | |
| 32 | | | 1 | 1 | 1 | | | |

B12 MSM SCNV
 | | |

FIGURE 1.4
 U18 - TIMING PROM
 2-39

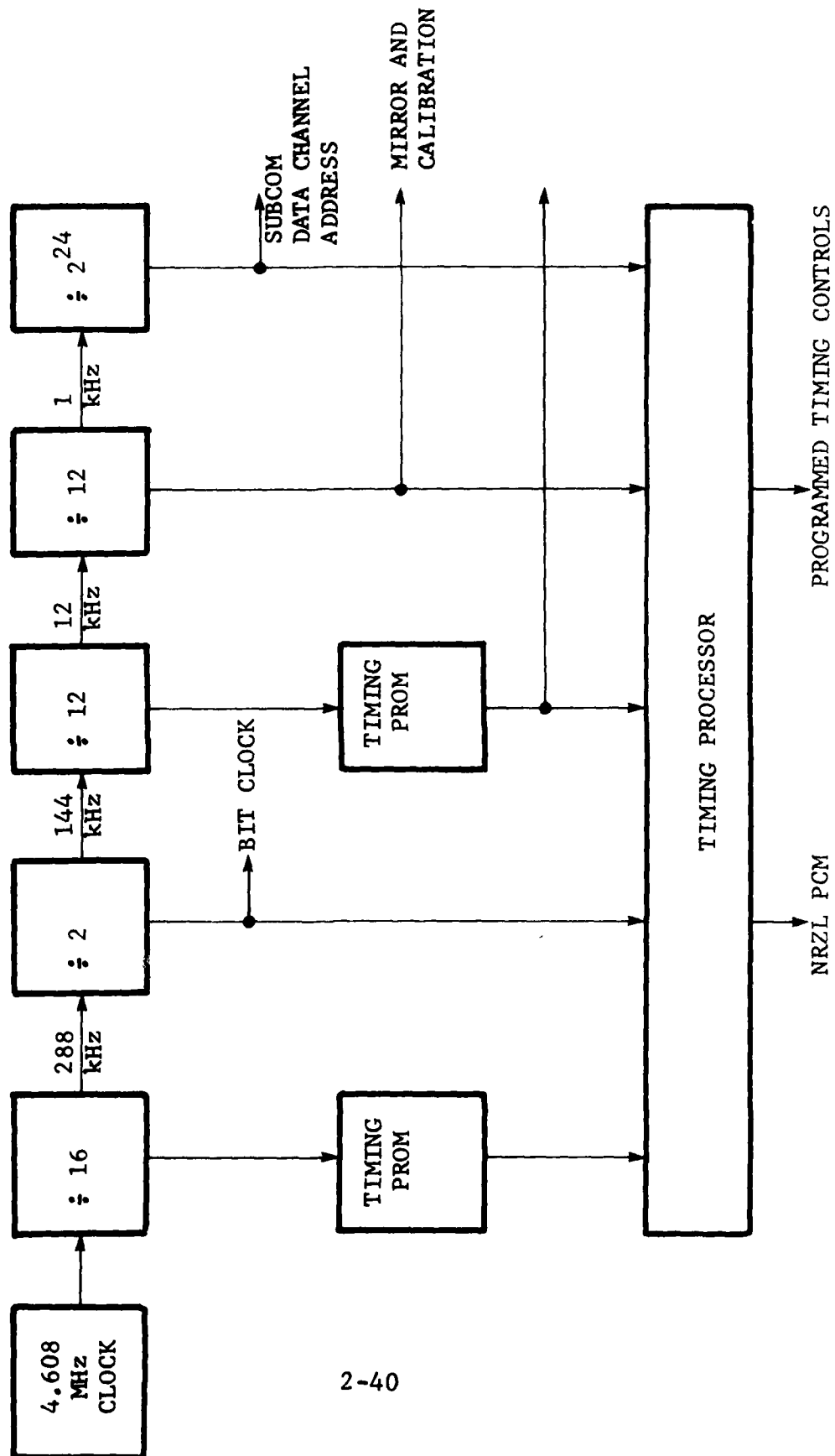


Figure 1.5 LOGIC BLOCK DIAGRAM

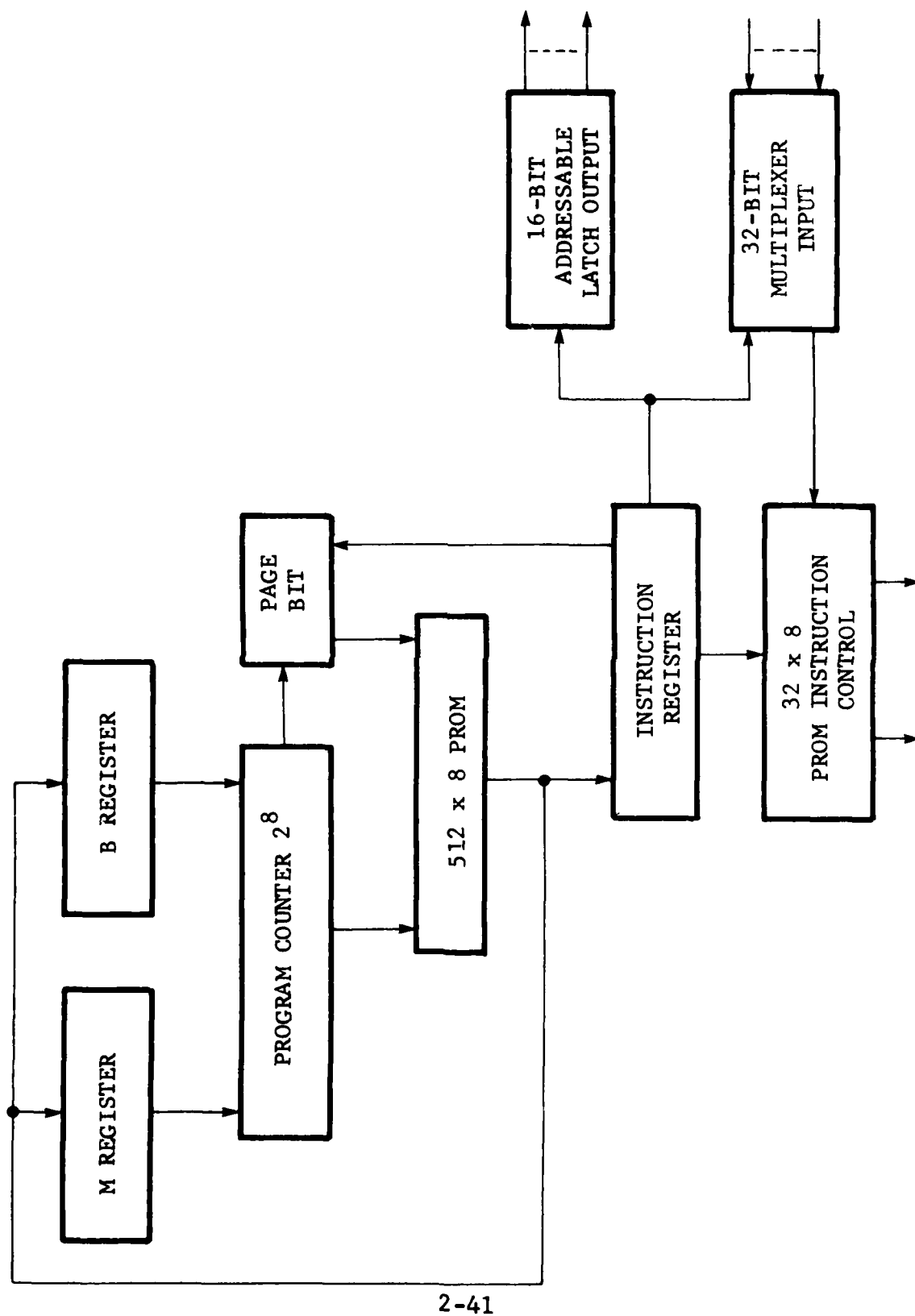


Figure 1.6 1-BIT PROCESSOR BLOCK DIAGRAM

| 25 | 26 | 27 | 28 | 29 | 30 | 31 | 32 | 33 | 34 | 35 | 36 | 37 | 38 | 39 | 40 | 41 | 42 | 43 | 44 | 45 | 46 | 47 | 48 |
|----------|----------|----|----|----|----|----|----|----|----|----|----|-----|------|----|----|----|----|----|----|----|----|----|----|
| MARKER | BURRY | MS | MS | MS | MS | MS | MS | MS | MS | MS | MS | | | | | | | | | | | | |
| POSITION | ADJUSTED | 1 | 2 | 3 | 4 | 5 | 6 | 7 | 8 | 9 | 10 | HK1 | TMP1 | 1 | 2 | 3 | 4 | 5 | 6 | 7 | 8 | 9 | 10 |

[illegible]

TMP1 - MOTIV SRAVO
 TMP2 - TANK-TOP RIGHT FRONT
 TMP3 - BRACEMENT FRONT
 TMP4 - FSCAL PLANE
 TMP5 - SCAN MIRROR
 TMP6 - TANK - REAR UPPER RIGHT
 TMP7 - TANK - REAR LOWER - LEFT
 TMP8 - BRACEMENT TOP INSIDE - FORWARD

BIT RATE - 144 Kbps - 6.94 MS
WORD RATE - 12 MS - 83.3 MS
FRAME RATE - 250 MS - 4 MS
MAIN FRAME RATE - 31.25 MS - 32 MS

CODE 15 NRZ-M
NRZ-M-0000100101011011
DATA-0000101110100110

BOOLEAN - DATA 3.7.3 NRZ-M ($B_i T_n \oplus B_i T_{n-1}$)
ALL MAGNITUDE DATA WORDS ARE TRANSMITTED MID FIRST

RIM DATA - LAMIE
 SPATIAL ANALYTICS
 1/20/77 G.S.

Figure 1.7

BASIC INSTRUCTION SET

| | |
|------|--|
| WAIT | Wait if line selected is "true" |
| SKIP | Skip next instruction if line selected is "true" |
| CNDB | Branch to second byte address if line selected is "true" |
| OUT | Output a "0" or "1" on line selected |
| LDM | Load 2nd byte nn M Register |
| JMPM | Jump to M address in hi or lo page |

2.0 INTERFACE

2.1 Applicable Documents

Schematic No. 21014163

Detail No. 21014164

Assembly No. 21014165

2.2 Interfaces

2.2.1 Inputs

| | |
|-----------------|-------------------------------------|
| MXADO - MXAD2 | Interface multiplexer address lines |
| DC1OUT - DC4OUT | Four multiplexed data channel lines |
| 15VARTN | 15V-A return for DC-OUT |
| TMOT | Temperature multiplexer output |
| TMSG | Return for TMOT |
| HKOT | Housekeeping multiplexer output |
| HKSG | Return for HKOT |
| MPMH | Mirror motor position Hi |
| MPML | Mirror motor position Lo |
| ABIN | Analog - binary data output |
| BCLK | Data bit clock - 144KHZ |
| <u>B12</u> | Data bit 12 |
| <u>SCONV</u> | A/D converter trigger |
| OSW | Output switch select |
| PRPCM | Programmed PCM |
| DSELO | 6KHZ LSB Data Frame Word Counter |
| DSEL1 | 3KHZ " " " " |
| DSEL2 | 1.5KHZ " " " " |

| | | |
|---------------|-----------|--|
| DSEL3 | 1KHZ | Data Frame Word Counter |
| C500 | 500HZ | Data Frame Word Counter |
| C250 | 250HZ MSB | " " " " |
| CSELO | 125HZ | Subcom Data Counter |
| CSEL1 | 62.5HZ | " " " |
| CSEL2 | 31.25HZ | " " " |
| DADD0 - DADD8 | | Data Word Select Lines (word stripper) |
| FSFS | | Frame / Subframe Rate Select |

2.2.2 Outputs

| | |
|--------------|---|
| ABCLK | Data Clock to AGE (buffered) 144KHZ |
| PCMA | PCM Data Stream to AGE NRZL |
| TPCMH | PCM Data to Transmitter (6 poles filtered) Hi |
| TPCML | PCM Data to Transmitter Lo |
| DECO - DEC11 | 12 bits of data word |

2.3.3 Power (Ma's)

| | <u>Typical</u> | <u>Maximum</u> |
|---------|----------------|----------------|
| +5VDC | 283 | 368 |
| +15VDC | 58 | 64 |
| -15VADC | 52 | 68 |

2.3 Description

Figure 6.1 shows a block diagram of the Interface board. The board contains analog multiplexer, A/D converter for conversion of all sensor data, a premodulation filter for digital PCM data and a 12 bit word stripper.

U1 is an eight channel analog differential multiplexer. It has four inputs from the four DCE boards (DC1OUT-DC4OUT), two inputs from the Housekeeping board (HKOT, TMOT) and two inputs from the Motor Servo board (MPMH, ABIN). The output of U1 is buffered by AR1 - AR3 and goes to the 12 bit A/D converter. (U4). The twelve digital bits of each word go to a parallel in - serial out shift register U3 and U5. These are shifted out through gating (U7). Additional digital data from the processor (PRPCM) is multiplexed into the bit stream through the gating (U7). The multiplexed bit stream goes to the premodulation filter and to the word stripper

The premodulation filter is composed of AR2 - AR4 and associated passive components. It is a six pole low pass Butterworth type with the break frequency at 100.8KHZ (.7 x bit rate). The output amplifier (AR5) provides an isolated output at unity gain.

The word stripper is composed of U8-U15. The desired word and subcom are selected at the AGE panel via lines DADD0 - DADD8 and FSFS. These go to bit comparators (U12 - U14) which compare the DADD0 - DADD8 lines with the data frame word counter lines from the Logic board (DSELO - DSEL, CSELO - CSEL2, C500, C250). When a comparison is made, indicating that the desired data

is in the serial to parallel shift registers (U8, U10), the hex D Flip - Flops (U9, U11) are loaded (via DEN). The desired data is continually up-dated at either the frame or subframe rate. The hex-D Flip-Flops drive LED displays on the AGE panel.

A 50 Ω driver circuit (21018824) is provided in order to drive the 50 Ω termination at the telemetry interface. The driver (AR1) and associated passive components are mounted on a separate metal bracket in the electronics assembly.

The data frame format is shown in Section 1.0 (Figure 1.7) and represents the sensor data stream.

3.0 TWO STATE CALIBRATOR

The Spatial Radiometer in-flight calibrator consists of a short piece of tungsten wire mounted at the base of the focal plane. A feedback control loop in the electronics controls the temperature of the wire. The original design maintained the wire at a certain temperature in order to provide a photon bias for the detectors. This bias alters the frequency response of the detectors, so that a flat frequency response over the bandwidth of the system (0 - 50 Hz) can be achieved. In addition, by in-flight command, the temperature of the wire could be increased to a pre-determined level, for calibration purposes.

The design was changed to include a second calibration level. A single in-flight command is needed to achieve the two levels of calibration. Figure 3.1 shows the calibration timing relative to the mirror position.

The command input can be completely asynchronous with respect to the system. After the command is executed the system waits until after the first DC restore pulse occurs. The first calibration level is then done. The time limit of the level is alterable (0 - .9 secs). The second level is done after the next DC restore pulse and the time limit is the same as the first one. After shut down of the second level, no more calibration is performed and the wire return to its optical biasing temperature. The two calibration levels will be adjusted so that all detectors will have a signal-to-noise ratio of at least 10 for one or the other level.

The hardware implementation of the calibrator is on two boards - Interface and the Motor Servo Electronics. The calibration command (CCAL) is Filtered and buffered by AR17-B on the Motor Servo board. The command then goes to the U5 Flip-flop on the Motor Servo and the Flip-flop on the interface board which provide the necessary timing to control the Q8 and Q11 FET switches. The state of these switches determines which calibration state the wire is in or if it is in the optical bias state. The AR13 amplifier and the associated components comprise the feedback controller for the hot wire. Refer to Motor Servo Board description in Document Number Spat. Radiometer-073076-0007. It should be noted that the description that appears in the above document is for the initial one state calibrator which was modified to the two state calibrator.

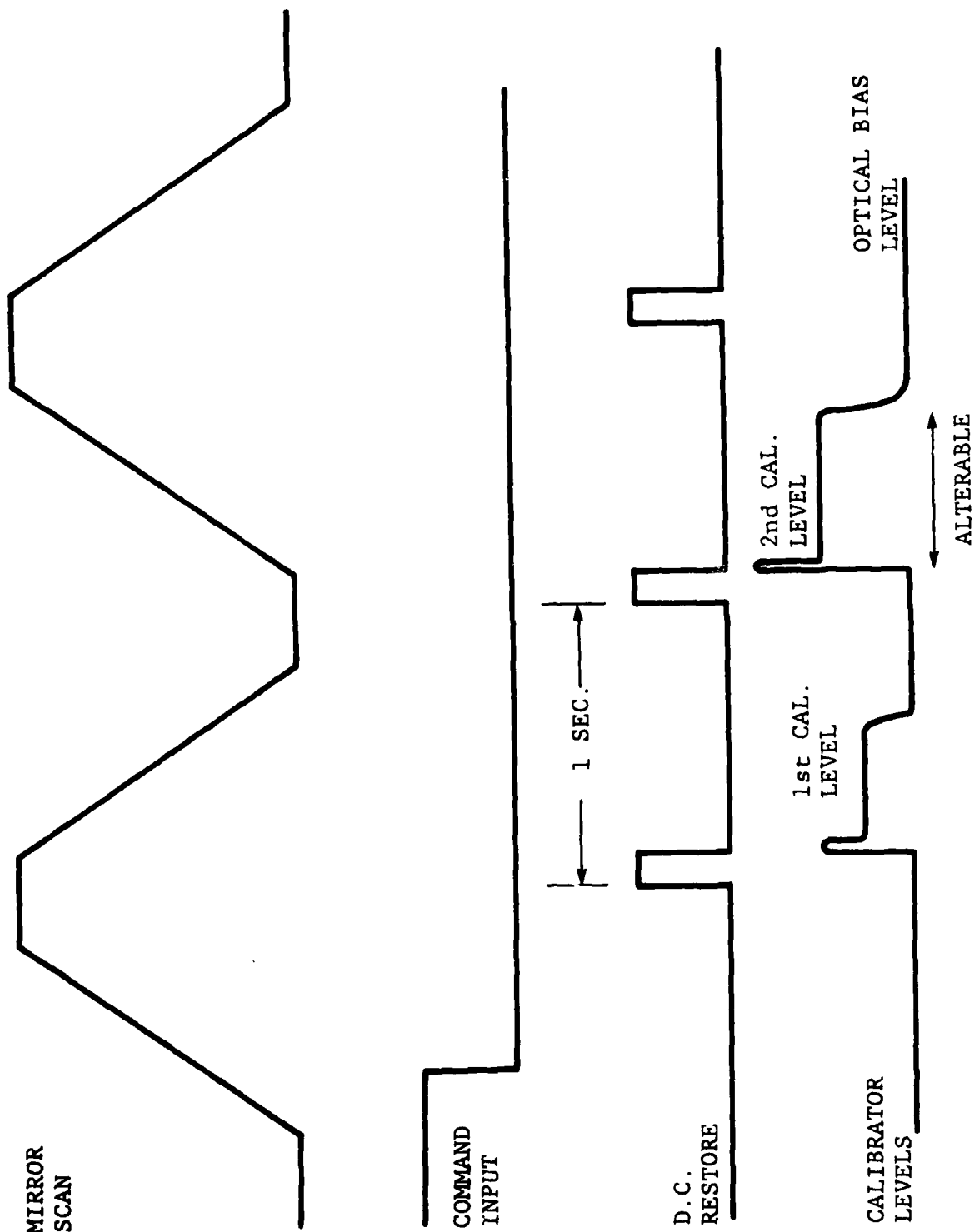


Figure 3.1 CALIBRATION TIMING

SECTION III

SCAN MIRROR DESIGN

REFERENCE DOCUMENT NUMBER 032476-0004

SUMMARY

The complete report of the scan mirror is included in Volume II of this report. This section will address the Design Analysis portion of the complete report. Page numbers have been changed to conform to this report.

1.0 INTRODUCTION

The Spatial Radiometer measures extended source radiation over a 4×6 degree field of view. The emissions are monitored in two color bands and at two resolutions, requiring four linear arrays of detectors. These arrays are scanned through an angle of 24° to produce a two dimensional scene. The sweep is accomplished by placing a folding flat mirror at 45° to the path of the recollimated beam off the secondary mirror and rotating the mirror $\pm 12^\circ$ around the axis parallel to the collimated beam. The beam is swept over focusing optics and imaged at the detectors, having the effect of sweeping the detector arrays across the scene as defined by the field stop of 6° and an additional 3° to either side of the stop.

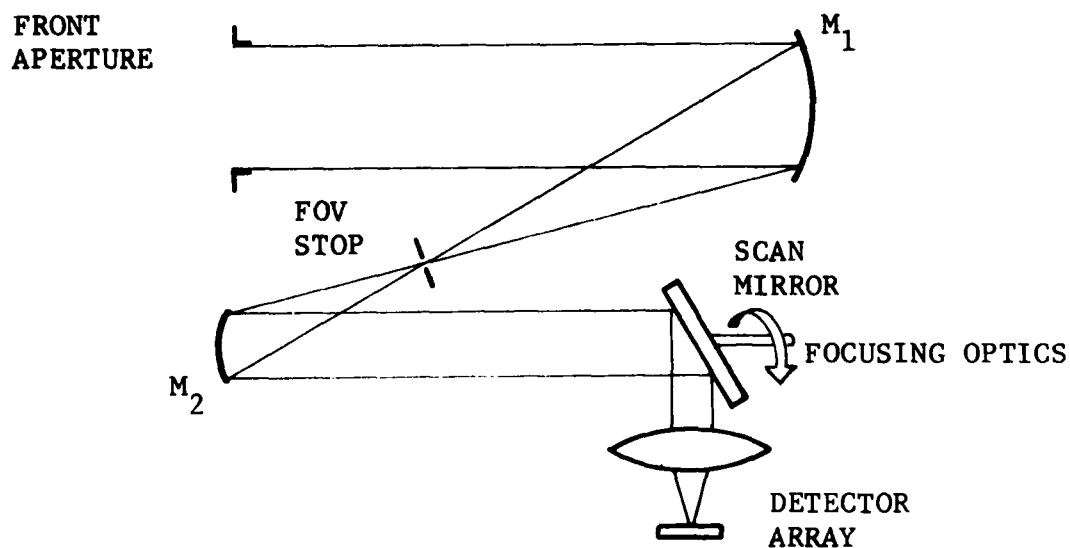


Figure 1

Since the mirror itself would be a source of IR photons, it must be cooled to 80K. In addition, its position must be known to a high resolution, (0.1°), and its motion must be smooth, controlled, and synchronized to such functions as clamping and calibration.

A lab test scanner was assembled using stock parts and lab machining. The housing and mirror were made of steel to minimize contraction and allow for operation from 300K to 80K paired Bartemp bearings were used with standard preloading. An Aeroflex brushless dc torque motor (V10Y-30) was used in conjunction with a Pickering rotary variable differential transformer (20600) for position pickoff.

A servo drive circuit was designed and breadboarded. The circuit was checked out electrically, and then the scanner was operated at cryogenic temperatures. The means of sealed cooling was found to be important since moisture can damage the bearing races. In addition, the quality of the bearing used and the manner of mounting them was critical to achieving proper operation at cold temperatures. After several iterations the lab test scanner was successfully operated through three thermal cycles with no bearing damage. Servo performance was satisfactory. A good design margin will be provided in the flight version, by using a motor with 3.5 times the torque sensitivity. (Aeroflex V18-44.)

2.0 SERVO LOOP

The motor current loop was modeled as follows:

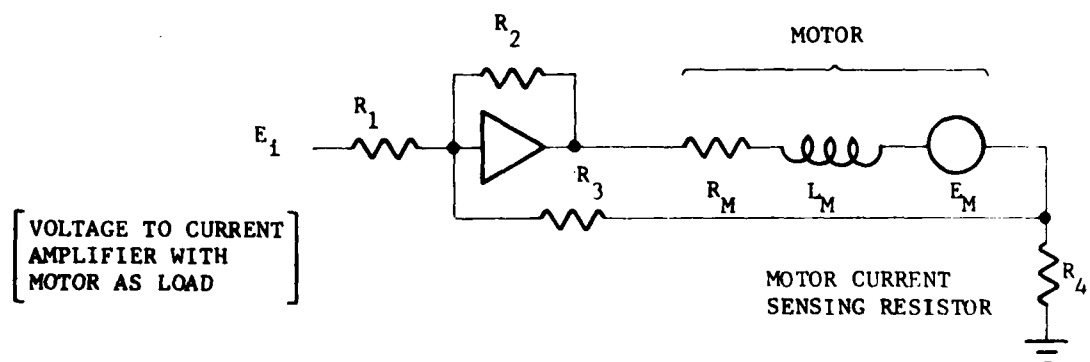


Figure 2

DRIVEN VOLTAGE

E_1

$\frac{R_2}{R_1}$

Σ

VOLTAGE

Σ

$\frac{1}{L_{MS} + R_O}$

CURRENT

K_T

Σ

TORQUE

$\frac{1}{J S}$

DRAG

B

ANGULAR VELOCITY

$\dot{\theta}_M$

K_V

VOLTAGE PROPORTIONAL TO MOTOR CURRENT

BACK EMF PROPORTIONAL TO SPEED

$(R_4 + R_M = R_O)$
 $(S = \text{LAPLACE TRANSFORM})$
 $(R_4 \ll R_3)$

Working from right to left:

- 7902-4

Thus, the loop produces a motor current proportional to command voltage.

The following physical values were used in the stability calculations:

$$R_O = R_4 + R_M \approx 40\Omega \quad (\approx 80^\circ) \quad (10\Omega \text{ sensing resistor plus motor windings})$$

$$L_M = 10^{-2} \text{ Henries (motor inductance)}$$

$$K_T = 9 \text{ oz-in./A (motor torque sensitivity) (Aeroflex V18-44)}$$

$$K_V = 0.07 \text{ V/rad/s (motor back EMF)}$$

$$B = 0.1 \text{ oz-in./rad/s (frictional drag)}$$

$$J = 3 \times 10^{-3} \text{ oz-in./s (mirror/shaft moment of inertia)}$$

A flurry of manipulations allow the preceding block diagram to be presented in the following, more manageable format with no overlapping loops and only the unity feedback closure around the current loop:

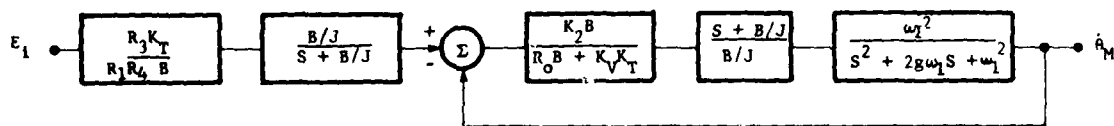


Figure 4

The following assignments have been made to provide this convenient form:

$$K_2 = \frac{R_2}{R_3} R_4$$

$$\omega_1^2 = \frac{R_O B + K_T K_V}{J L_M} = 1.54 \times 10^5$$

$$2g\omega_1 = \frac{R_O}{L_M} + \frac{B}{J} = 4.033 \times 10^3$$

The poles of the quadratic solve to

$$S = 4000 \text{ rad/s and } 41 \text{ rad/s}$$

The dc gain ($S=0$) in the current loop is

$$K_{CL} = \frac{BK_2}{R_O B + K_V K_T} = 2.16 \times 10^{-2} K_2$$

The damping lead (zero) is at $B/J = 33.3 \text{ rad/s}$. The Bode plot looks like this:

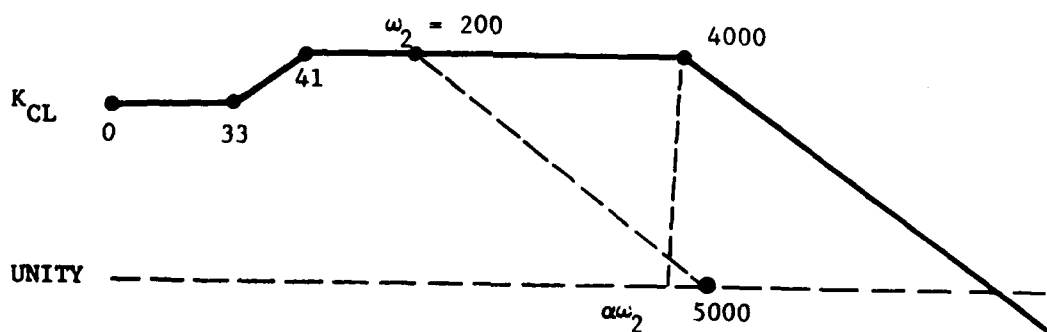


Figure 5

A reasonable current gain would result in a unity crossover far beyond 4000 rad/s which is undesirable. Thus, a lag is introduced around the current amplifier to produce the plot shown by a dotted line. Assuming a current loop gain of 20 we find:

$$K_{CL} = 20 = 2.16 \times 10^{-2} K_2$$

$$K_2 \approx 1000$$

If we set $R_4 \approx 10\Omega$ and $R_2 = 200K\Omega$, then $R_3 = 2K\Omega$. Assume $\sigma = 20$ to put unity crossover near 4000 rad/s. Then, ω_2 is 200 which is accomplished by a $0.025\mu F$ capacitor in parallel with R_2 .

The first two blocks of Figure 4 represent position information being fed to the current amplifier summing point. Assuming 1V/rad sensitivity from the RVDT and introducing K_A as the gain of the RVDT detector/amplifier, then the dc position loop gain ($S=0$) becomes

$$K_{PL} = \frac{K_A K_T R_3}{R_1 R_4 B}$$

The Bode plot is:

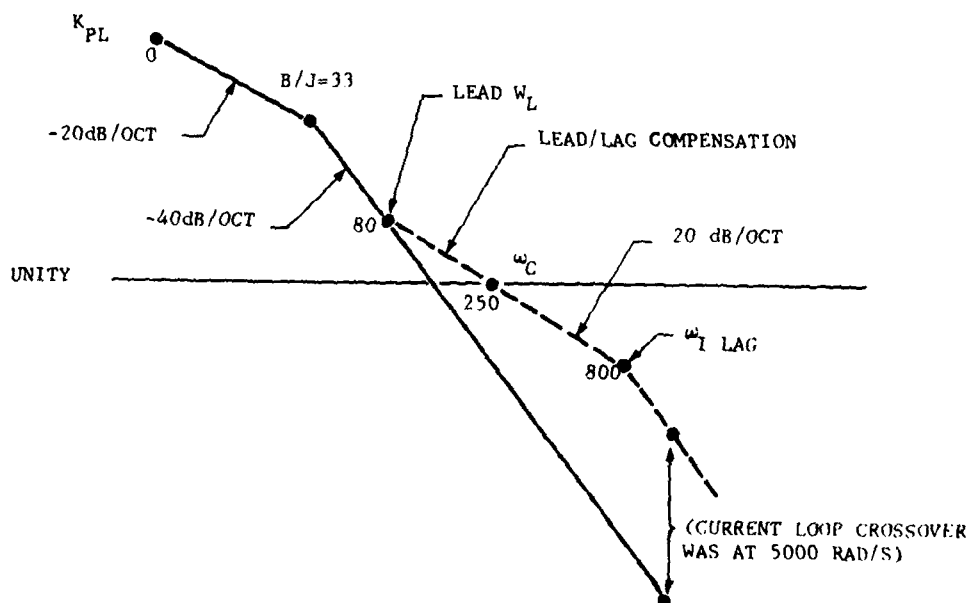


Figure 6

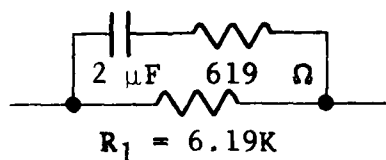
The uncompensated plot has a crossover at 40 dB/oct. A lead/lag must be introduced as shown in the dotted lines. A rule of thumb is to pick $\omega_C = 1/20 \times$ current loop bandwidth: $\omega_C \approx \frac{5000}{20} = 250$ rad/s. A lower number would be less accurate; a higher number less stable.

Pick $\omega_L \approx 1/3 \omega_C$ and $\omega_I \approx 3 \omega_C$. Therefore, $\omega_L \approx 80$ and $\omega_I \approx 800$. To get a crossover at 250 with a plot which (when compensated) is roughly linear ≈ -20 dB/oct one should start with a gain of 250, i.e. $K_{PL} = 250$. Thus,

$$K_{PL} = \frac{K_A K_T R_3}{R_1 R_4 B} = 250$$

$$\frac{(K_A)(2000)(9)}{(R_1)(10)(0.1)} = 250, K_A = 0.01389 R_1$$

Pick R_1 to be 6200Ω ; then $K_A \approx 85$. The lead resistor is picked at $R_1/10 = 620\Omega$. The lead/lag network is formed around R_1 thusly:



The lead is at $\omega_L = \frac{1}{R_1 C} = \frac{1}{(6.19K)(2\mu F)} = 80$ rad/s, and the lag is at $\omega_I = \frac{1}{(619\Omega)(2\mu F)} \approx 808$ rad/s. These are plotted in Figure 6 with dotted lines with the unity crossover at 250 rad/s at -20 dB/oct. A simplified representation of the resulting circuit is shown in Figure 7.

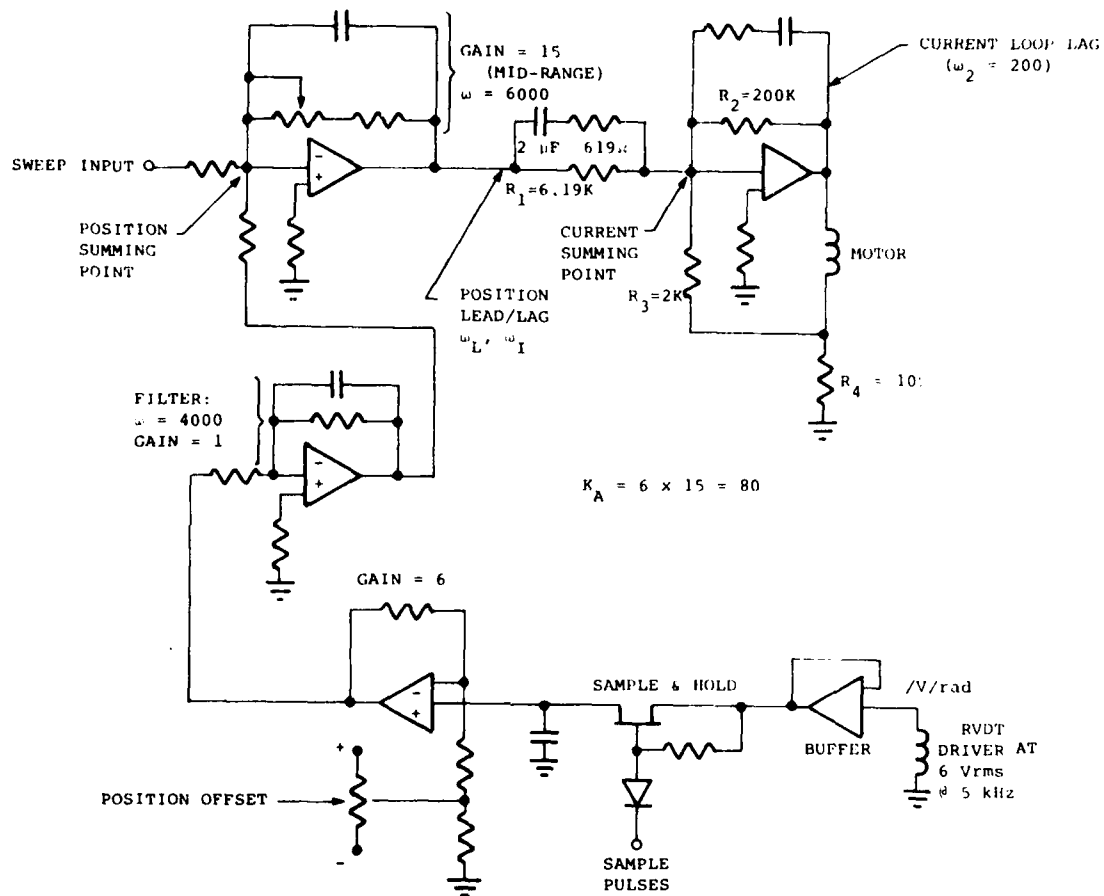


Figure 7

SECTION IV

OPTICAL DESIGN

SUMMARY

Two designs for the recollector optics were considered originally and the final configuration was the reflective system outlined in this section.

1.0 INTRODUCTION

The spatial radiometer optics consists of a reflective fore optics section which performs the functions of radiation acquisition, field of view definition, and straylight rejection, and a recollector optics section which focuses the energy onto a detector array to be scanned over a field of view of $\pm 3^\circ$ in object space. Since the length of the array subtends an angle of 4° , the instrument total field of view is $4^\circ \times 6^\circ$.

The fore optics section has been designed and analyzed thoroughly enough to start procurement. Two designs are under investigation for the recollector optics; a refractive one using two silicon lenses and a sapphire field flattener, and a reflective one using a single parabolic mirror. The advantages of each approach are given in the sections below.

2.0 FORE OPTICS

The telescope components are shown in Figure 1. Mirrors M1, M2 and the field stop constitute the fore optics.

3.0 STRAYLIGHT REJECTION

In order to achieve high rejection of unwanted off-axis radiation, we use an optical design which eliminates all such radiation propagated geometrically, and most of that propagated via diffraction as well. By placing baffles as shown in Figure 1, all stray radiation that enters the entrance aperture is vignetted by either the primary mirror M1, or by the field stop, according to the laws of geometrical optics. However, since an image falling on the opaque portion of the field stop consists of a diffraction pattern which extends to infinity, a certain portion of the outer rings of the pattern will always pass through the field stop opening.

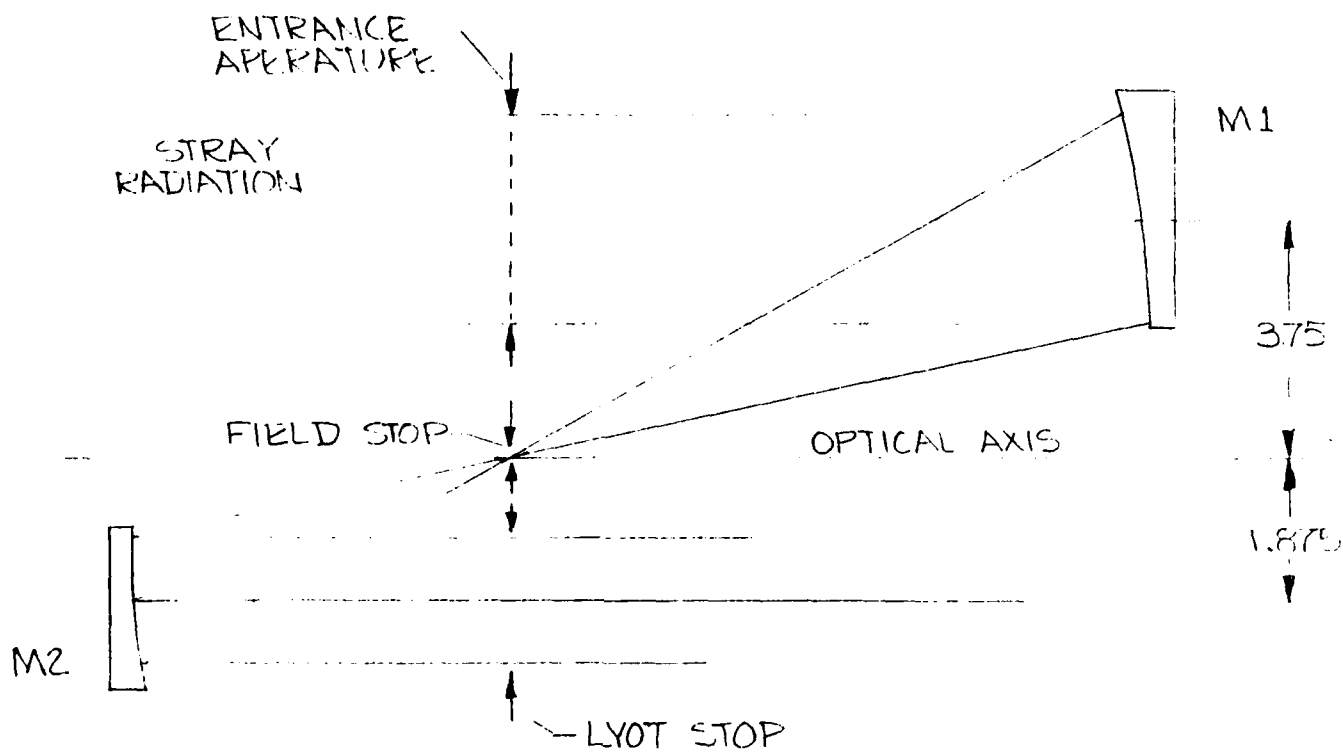


FIGURE 1
BAFFLES IN S.R. FORE OPTICS

4-4

This diffracted energy appears to originate at the diffracting aperture, according to the boundary wave diffraction theory. Since an image of the edge is formed, a baffle placed at the latter location will block most of the diffracted energy, achieving very high system rejection. As a further refinement we may eliminate radiation which undergoes a second diffraction at the boundary of the field stop, at any subsequent focal plane or field mask. Such a combination of rejection baffles represents the best approach to eliminating unwanted off-axis radiation developed so far.

4.0 SPECIFICATIONS

The fore optics specifications are given in Table I. The entire system is summarized in Table II.

TABLE I
FORE OPTICS SPECIFICATION

| Surface No. | Radius of Curvature | Spacing | Comments |
|-------------|---------------------|---------|------------------------|
| 1 | ∞ | 12.0 | Entrance aperture |
| 2 | -24.0 | -12.0 | Parabolic primary M1 |
| 3 | ∞ | - 6.0 | Field stop |
| 4 | -12.0 | 6.0 | Parabolic secondary M2 |
| 5 | ∞ | 1.0 | Lyot stop |

TABLE II
SPATIAL RADIOMETER SPECIFICATIONS SUMMARY

| | |
|---|-----------|
| Total field of view | 6° x 4° |
| Effective entrance pupil dia. | 2.8 in. |
| Dia. of diffracting aperture | ≈3.1 in. |
| Spectral band peaks | SW and MW |
| Total focal length, including recollector optics | 3.0 in. |
| Final F/number | 1.0714 |

The common optical axis of M1 and M2 is decentered 3.75" from the entrance aperture, and 1.875" from the Lyot stop, as shown in Figure 1.

5.0 ELEMENT SIZES

The sizes and shapes of the optical elements were determined by tracing rays backwards from the detectors for various scan mirror positions, and mapping their intersections with the surfaces. Since M1 and M2 constitute a 2X afocal telescope, the 3° scan pattern is accomplished by rotating the scan mirror through an angle of plus and minus 6°. The sizes of M1 and the field stop opening for this scan position are shown in Figures 2 and 3. Only these rays starting at the top and bottom center of the 4° long detector array were considered for these surfaces, since the other points within the array utilize the same apertures ahead of the field stop as do the centered elements, but do so at different instants during the scan.

These points are indicated in Figure 4, which shows the overall dimensions of the array. Due to the presence of pupil aberrations within the afocal telescope, the Lyot stop does not become imaged sharply in the plane of the entrance aperture. This causes no degradation to its diffraction rejection properties, since it is sufficient merely to provide an opening greater than that used by the actual radiation bundle. This size is given in Figure 5.

The sizes of the elements between the field stop and the detector were determined for points at the extreme corners of the detector array and for a scan mirror angle of 12° instead of 6°. There are two reasons for the differing conditions; the detector array will be scanned past the field stop edge to provide a dc restoration signal, and the apertures needed for the entire array must be provided at this larger scan angle. At this extreme, the portion of the field stop imaged onto the detectors is as shown in Figure 6. The area of mirror M2 that is used for this case is shown in Figure 7.

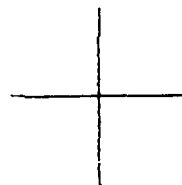
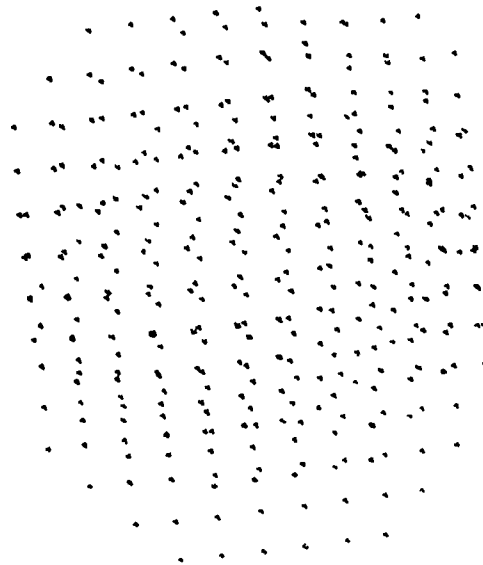


FIGURE 2
UTILIZATION MAP

M_1
6° Scan
Centered Array

4-7

5169
PLOT 13 1
7902-4

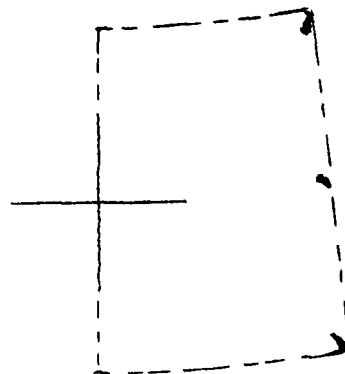


FIGURE 3
UTILIZATION MAP
Field Stop
6° Scan
Centered Array

S169
PLOT 12 2
7902-4

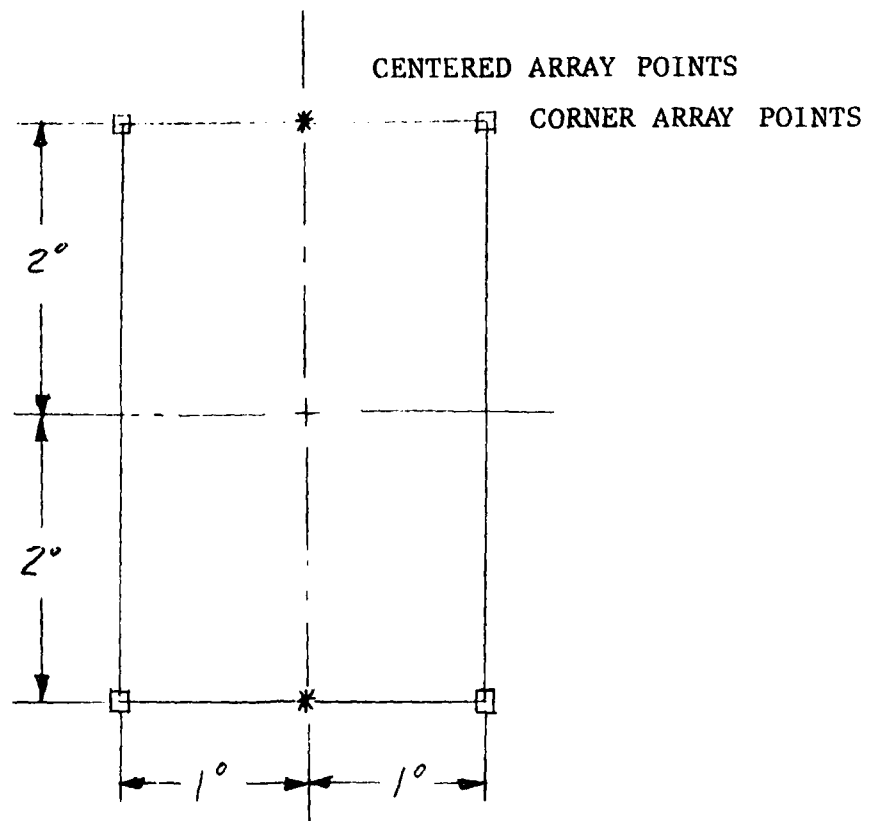


FIGURE 4
SIZE & SHAPE OF FOCAL PLANE AREA

AD-A061 584

HONEYWELL ELECTRO-OPTICS CENTER LEXINGTON MA
SPATIAL RADIOMETER. VOLUME 1.(U)

F/G 17/5

MAR 79 R SULLIVAN
7902-4-VOL-1

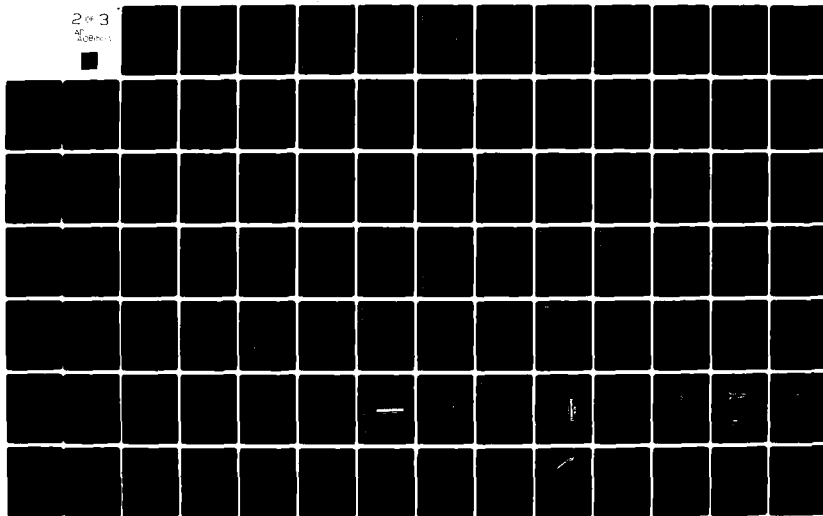
F19628-75-C-0179

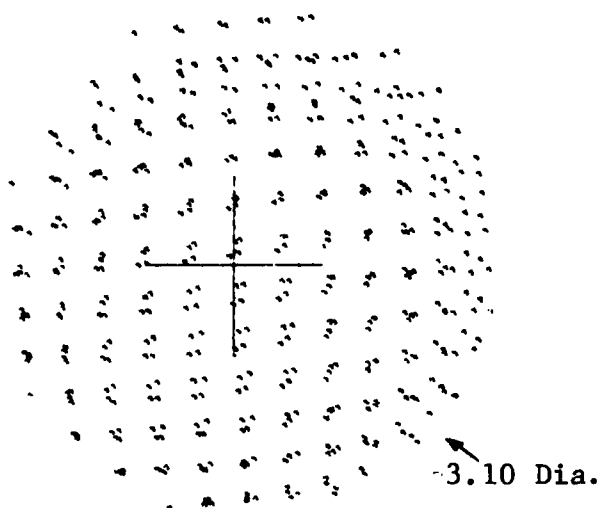
UNCLASSIFIED

AFGL-TR-80-0061-VOL-1

NL

2 of 3
AFGL-TR-80-0061-VOL-1





Entrance A

1X

6° Scan

FIGURE 5
UTILIZATION MAP

4-10

5135
PLOT 14 1
7902-4

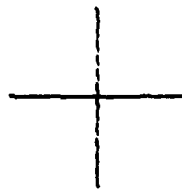


FIGURE 6
UTILIZATION MAP
Field Stop
12° Scan
4-11

5185
PLOT 13 2
7902-4

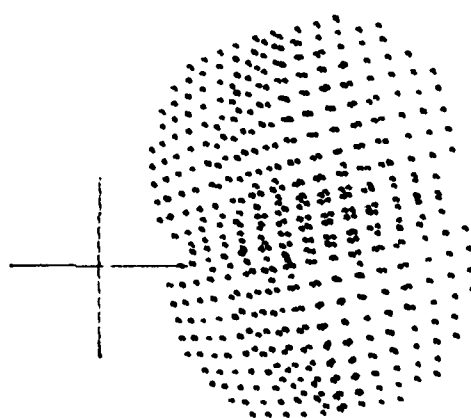


FIGURE 7
UTILIZATION MAP

M_2
12° Scan

5185
PLOT 11 1 0 -1.875

4-12

7902-4

To insure that adequate beam clearance is provided by the housing, the apertures needed at several places, other than at the elements themselves, were computed. The locations analyzed are shown in Figure 3, and the resulting apertures in Figures 8, 9, 10, 11, and 12.

6.0 RECOLLECTOR OPTICS

6.1 Reflective Recollector

A reflective recollector optics design employing a single parabolic mirror has been substituted for the two-lens refractive design. The chief reason for this design is the absence of ghost images in the reflective design. The distribution and intensities of the ghost images in the refractive design were found to conflict with the requirement for low veiling glare. Any ghost images formed by the filters or by reflection off of the detector substrate in the reflective design will appear nearly coincident with the actual image, and will therefore not contribute to the veiling glare.

This approach also has drawbacks: the detector assembly must be physically small so as to present a minimum obscuration to the incoming beam. The spider support must be thick enough to provide adequate thermal conductivity to cool the detectors, and yet must not give rise to excessive diffraction effects which would, in turn, cause veiling glare.

Our analysis indicates that none of these drawbacks are serious. The energy loss caused by the 1/2" obscuration is about 13%, and another 12% is obstructed by the 0.1" wide spider support. This thickness gives adequate thermal conductivity and negligible diffraction. The intensity of the diffracted energy collected on a detector of .010" on a side at a distance of .047" from the image, is 2×10^{-4} of the energy in the image.

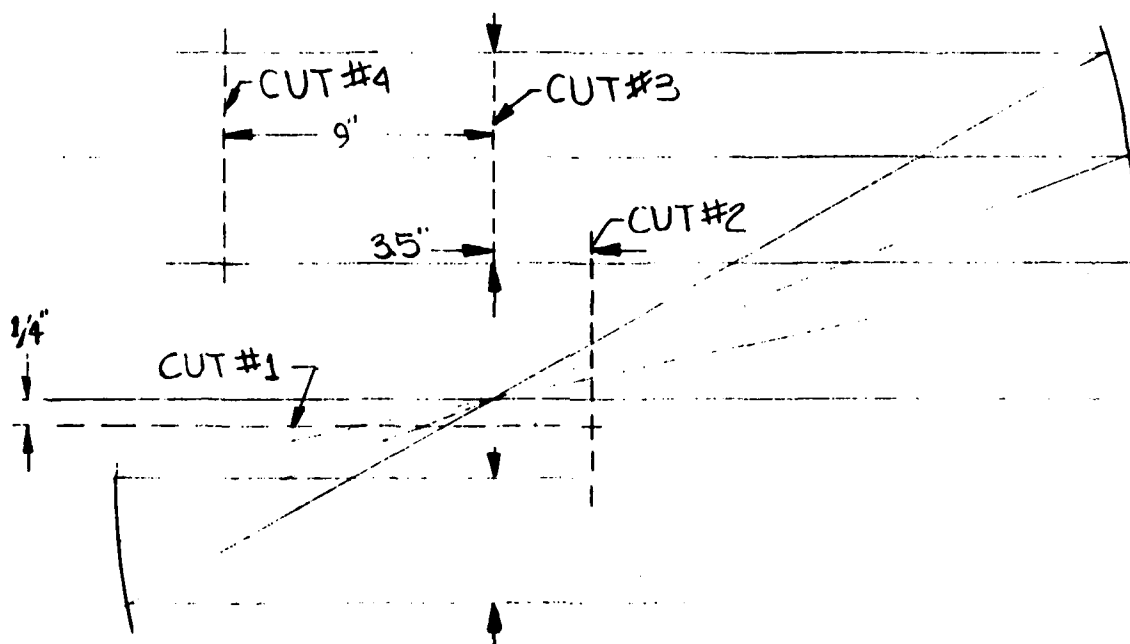


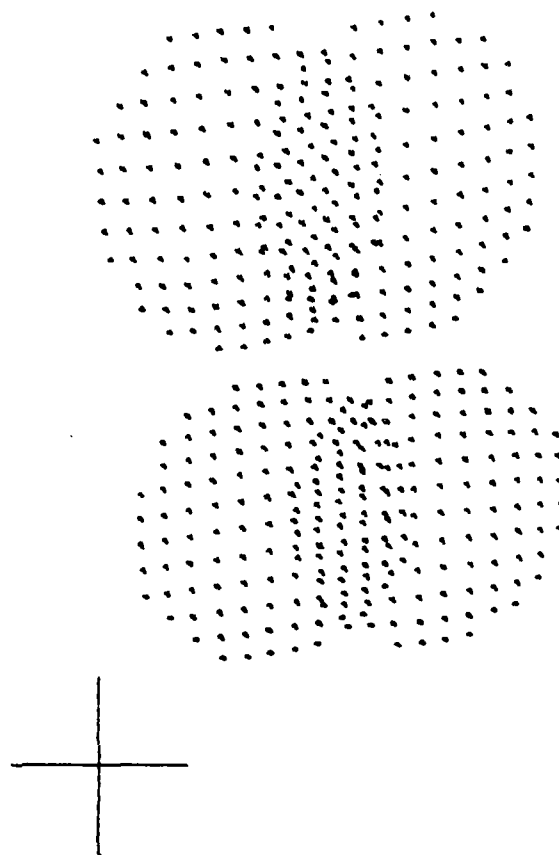
FIGURE 8
LOCATION OF CROSS-SECTION CUTS



FIGURE 9
UTILIZATION MAP - CUT NO. 1
Horiz. Cut
1/4" Below Axis
12° Scan

S185
PLOT 12 1
7902-4

4-15



3.5 In Fwd. Of Field Stop
2X

FIGURE 10
UTILIZATION MAP - CUT NO. 2

4-16

5139
PLOT 13 2

7902-4

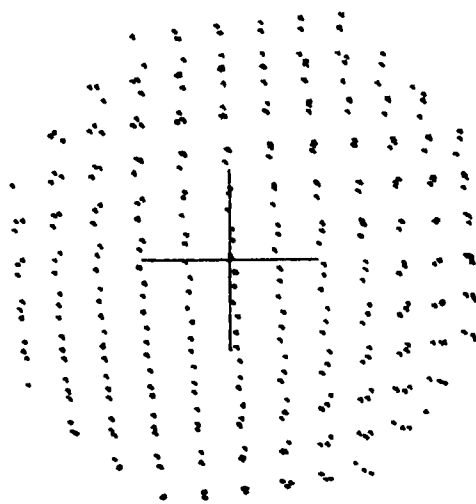


FIGURE 11
UTILIZATION MAP - CUT NO. 3
Entrance A
6° Scan
Centered Array

5169
PLOT 14 1

4-17

7902-4

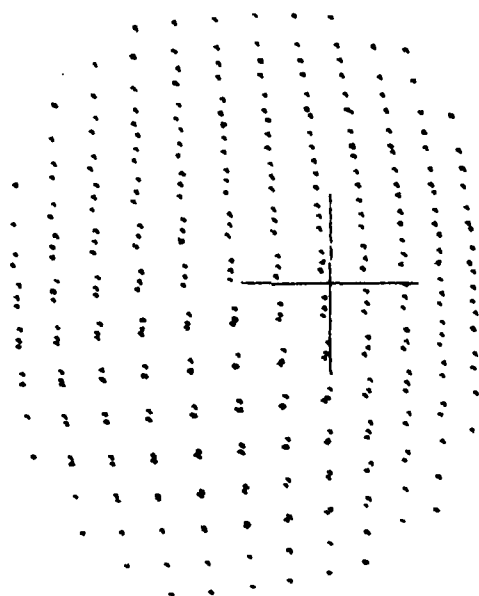


FIGURE 12
UTILIZATION MAP - CUT NO. 4
Cover
6° Scan
Centered Array
4-18

5169
PLOT 15 1

7902-4

A further advantage of using reflective optics is that the system design is not dependent on wavelength. With different filters, the same instrument may be used at any wavelength desired. A sketch of the reflective design is given in Figure 13.

The image quality of the single parabolic mirror is slightly poorer than that of the two-lens design, since it suffers from uncorrected coma, which varies linearly with field angle. The image size is very small near the axis, as shown in Figures 14 and 15; the smaller detectors will therefore be located closest to the axis.

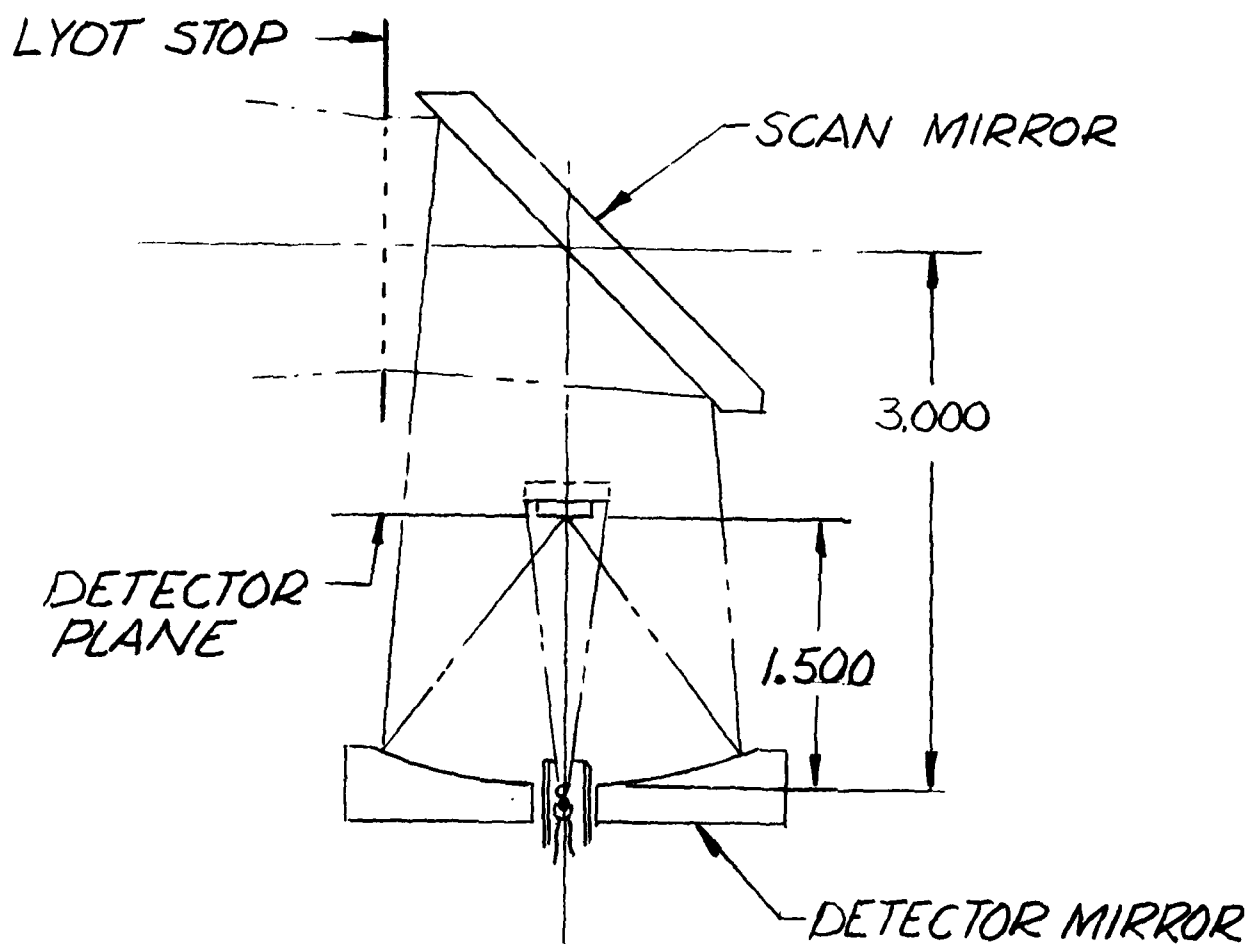


FIGURE 13

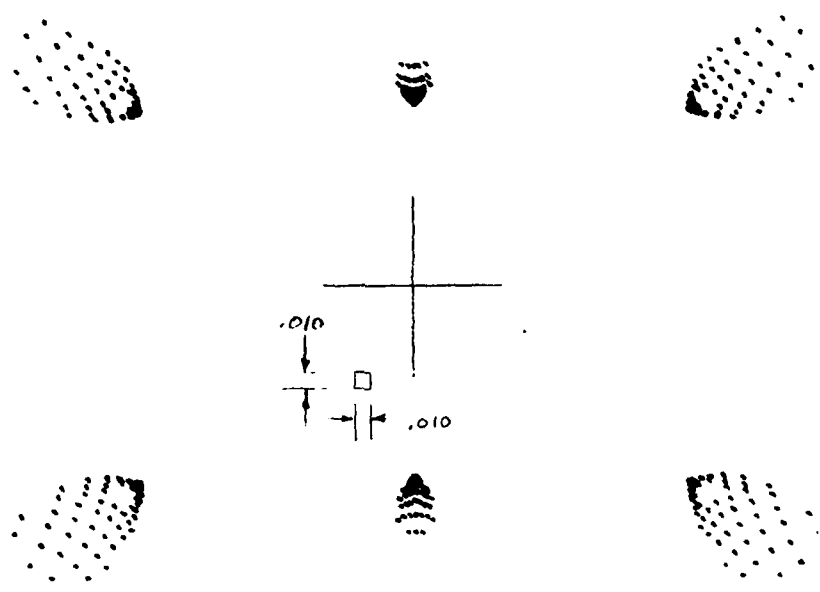


FIGURE 14
REFLECTIVE RECOLLECTOR
IMAGE - ON AXIS SCAN
4-21

5557
PLOT 11 10

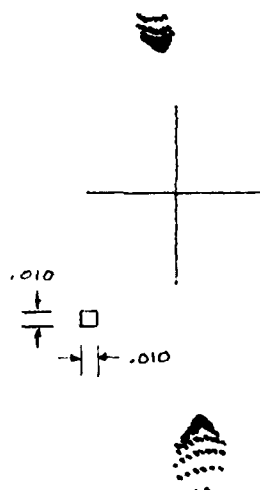


FIGURE 15
REFLECTIVE RECOLLECTOR
IMAGE - SCANNED 6°

5557
PLOT 11 10

4-22

7902-4

SECTION V

OFF AXIS REJECTION ANALYSIS

SUMMARY

This section will include the analysis criteria and a section of the OAR Test Report from system no. 1. The complete reports will not be included in Volume II because of classified information contained in the reports. Page numbers will be changed to conform to this report.

1.0 INTRODUCTION

An off axis rejection analysis for the Spatial Radiometer is performed to determine the capability of the sensor to reject bright background. An optical block diagram of the sensor is shown in Figure 1. The sensor components consist of external and internal baffles, low scatter primary and secondary optics and diffraction stops to suppress diffraction effects and an array of detectors.

1.1 System Description

The purpose of the baffles is to control the spurious light in both the forward and aft chamber. The external baffle is arranged with three cylindrical sharp knife edges while the internal baffle contains four sharp knife edges. Both baffles are concentric with the optical axis. The knife edges are used to trap off axis rays entering the sensor. The external baffle is 9.2 inches long. Knife edges are placed at the exit of the baffle and at 3.22 and 5.97 inches from the exit. The internal baffling unit is 9.0 inches long with baffles placed 2.95, 4.49, 6.12 and 9.0 inches from the exit of the external baffle.

Figure 2 shows various off axis rays entering the system and illuminations of the knife edges. The baffle walls are coated with cat-a-lac black paint to reduce the scattering off the walls of the baffle. The off axis rejection analysis assumed a five percent reflectivity off the baffles wall at high grazing angles. Specular reflection of the walls are trapped by the knife edge baffles. At the

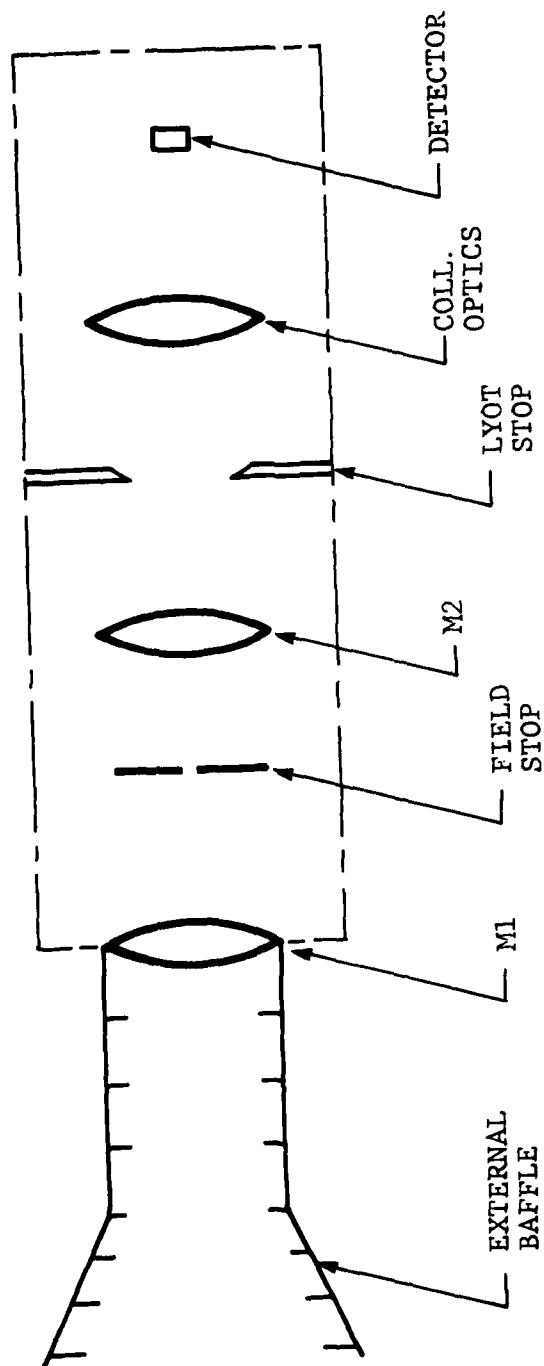


Figure 1 Optical Block Diagram of Spatial Radiometer

5-4

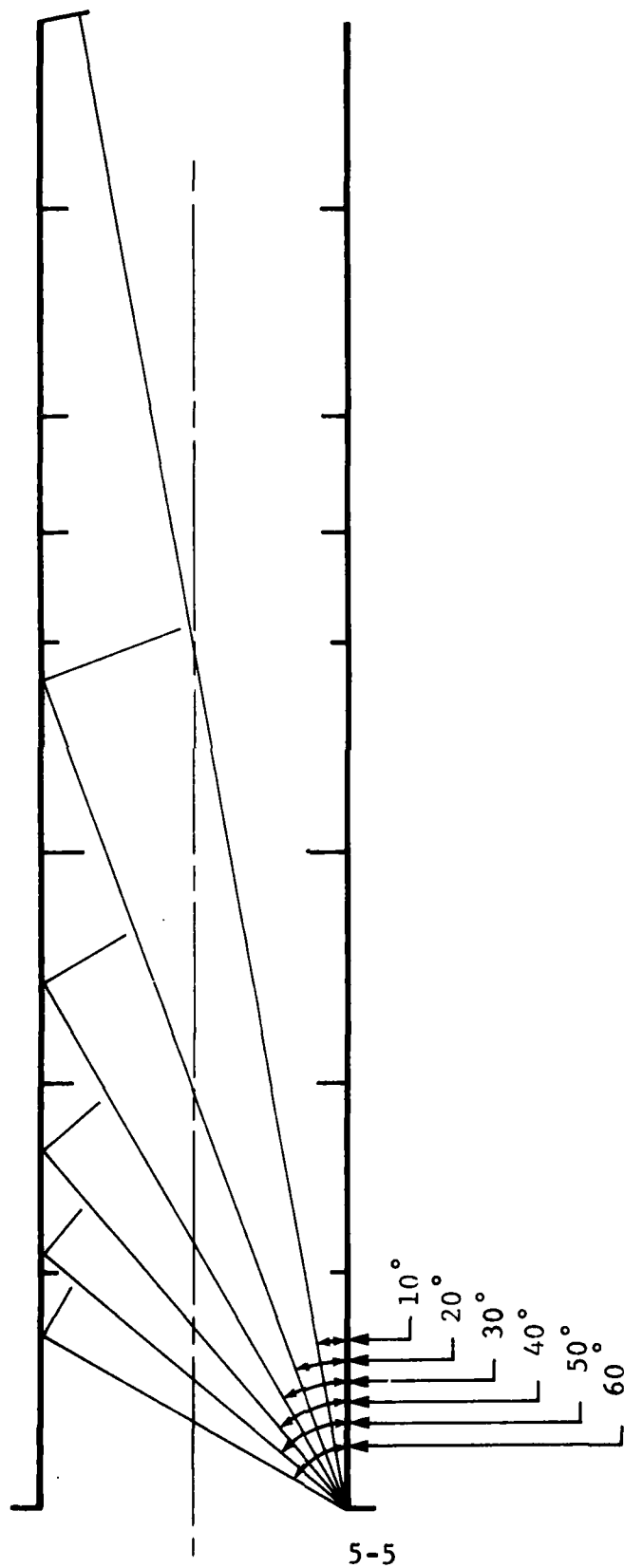


Figure 2 Baffle Layout Depicting Trapping of Off-Axis Rays

baffle edge, there is both reflection and diffraction, both of which produce stray light to the system. The edge diffracted light can be multiply reflected before entering the field stop but is very weak compared to the diffracted light directed into the FOV.

Light entering the aperture at an angle off axis is imaged as a point outside of the field stop. Diffraction, however spreads the image and some of the light is unavoidably passed on into the system. The field stop essentially blocks off main lobes of the diffraction pattern of the image which is produced by the finite extent of the entrance aperture. The field stop in the Spatial Radiometer has angular measurements of 4.76 by 6.5° . A ray entering the system thirty degrees off axis will image outside the field stop. Only the tails of the diffraction pattern will be passed on, while the major portion of the energy will be blocked. The field stop will also contribute to diffraction because of its finite extent. This field stop is placed one focal length distance from M1.

For off axis rays the image of the entrance aperture is at the Lyot stop. Diffraction, however will spread this image and some of the light is further passed on into the sensor. This stop effectively blocks the main lobes of the diffraction pattern produced by the entrance aperture. The Lyot stop is circular with a physical diameter of 1.4 inches. The system has a magnification factor at the Lyot stop of 0.5 . This magnification is determined from the ratio

of the focal length of M2 to that of M1. Therefore, the Lyot stop when projected to the entrance aperture is 2.8 inches. The Lyot stop will cause additional diffraction in the sensor due to its finite extent.

The focal plane consists of 40 (Hg,Cd)Te detectors, arranged in four linear arrays. Each detector has a 0.2 degree IFOV in the near field and a 0.4 degree IFOV in the far field. Each detector has dimension of 10.5 x 2 mils and 21 x 21 mils for the near and far field respectively. These detectors offers high detectivity in the SW and MW micron band. They operate at liquid nitrogen temperature.

The primary mirror (M1) collects the incoming rays and focusses them at the first field stop plane. This is a confocal parabola mirror with a 12 inch focal length. The surface scatter, BRDF, has been measured at 2×10^4 /sr at 1 degree from the mirrors geometrical center. Reflective scattering occurs at every mirror in the optical train, and thus each mirror is accountable for a scattering contribution to detector background. Scattering at the primary mirror must be kept small to reduce stray light.

The collimated light passing through the first field stop is reimaged onto the detector array by a reflecting telescope which uses a flat secondary mirror and a parabolic primary (M2). The focal length of M2 is 6 inches causing the image at the Lyot stop to be reduced by one half.

2.0 ANALYSIS

The point source rejection as a function of off axis angle is shown in Figure 3. Point source rejection is defined as the ratio of a point source with the source at an angle θ to the signal with the source in field. This ratio can be considered as the rejection of an elemental solid angle of an extended source. The main components of this ratio are scatter and diffraction. A point source is taken to be a distant source geometrically small compared to the IFOV of the sensor. For a mirror with a scatter coefficient of $10^{-4}/\text{sr}$ at 1 degree the scatter off the primary mirror and baffles in the point source rejection is predominant from 1 to 20 degree off axis. Thereafter, the major contributor is diffraction.

The extended source rejection as a function of off axis angle is given in Figure 4. This rejection is obtained by integrating the contributions of the individual point sources over the extension of the extended source when the source is off the edge of the field of view by an angle θ . An extended source is regarded to be large when compared to the IFOV of the detector. The extended sources to be considered here are the earth and the sun. The extended source rejection scatter and diffraction contribute equally for the first 10 degrees, thereafter, diffraction is predominant. Table 1 contains the required extended and the predicted extended flux density at the aperture in the two wavelength bands of interest for both the sun and the earth. From the table it is very evident that the Spatial Radiometer will perform well within the system requirements.

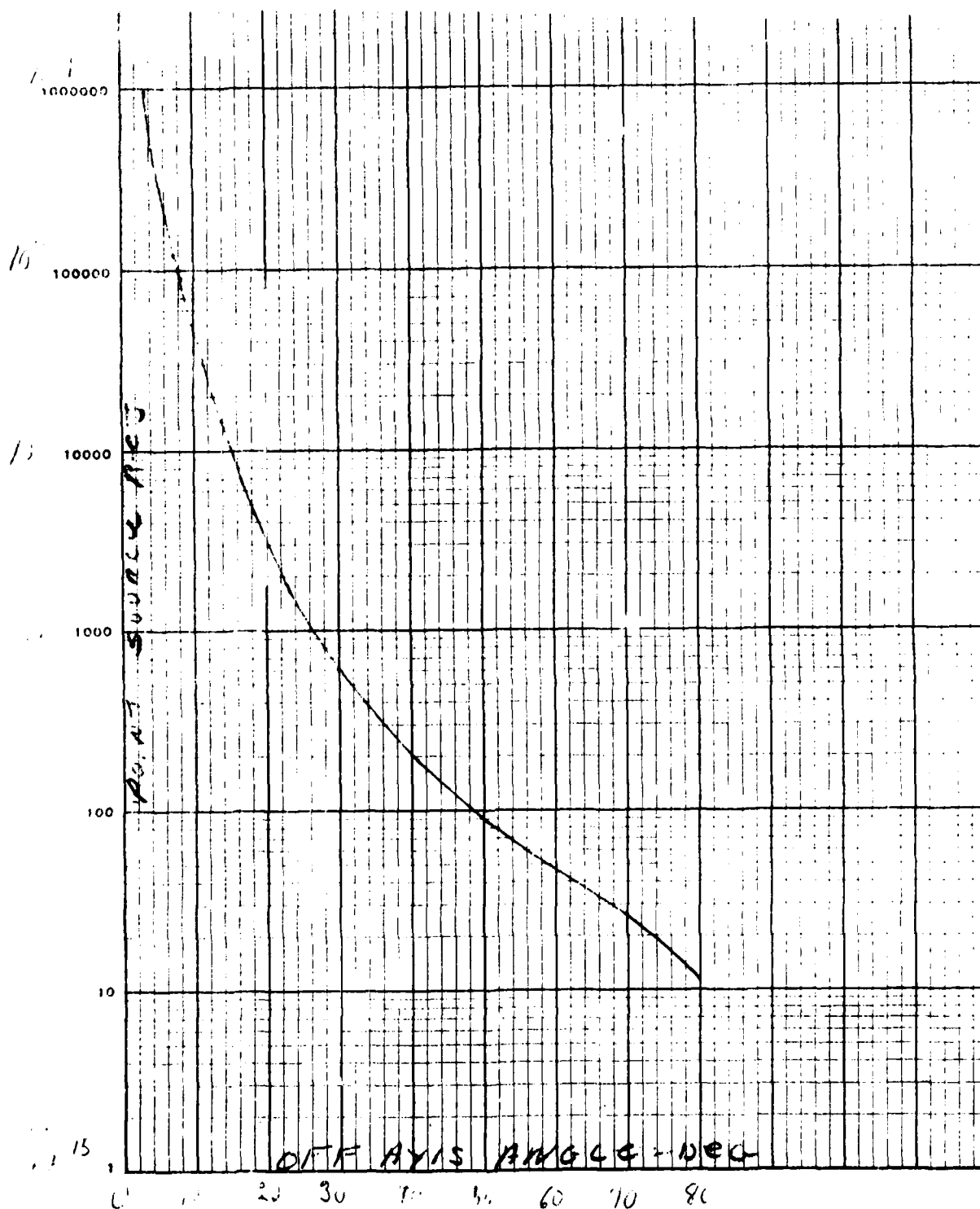


Figure 3 POINT SOURCE REJECTION VS OFF-AXIS ANGLE

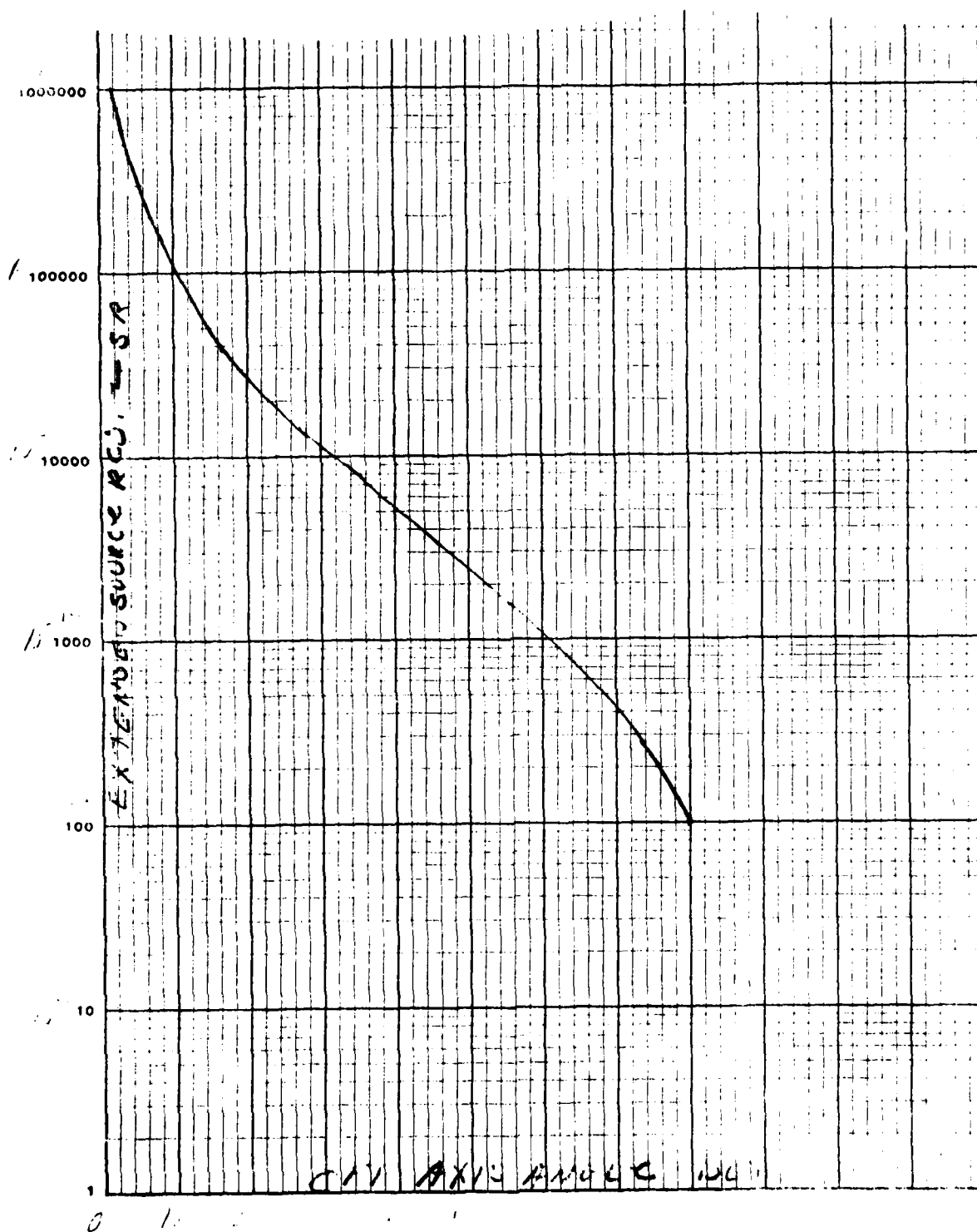


Figure 4 EXTENDED SOURCE REJECTION VS OFF-AXIS ANGLE

SECTION VI
OFF AXIS REJECTION
TEST DATA AND ANALYSIS

The results of the 1.06 micrometer rejection measurement testing on the spatial radiometer test vehicle are shown in Figures 1 through 8. Several general characteristics of the data are immediately apparent, the most notable of which is the minimum amount of variation among the eight scans. All the data reaches a measurement floor in the mid -10^{-10} range and shows the same discontinuities at far off-axis angles. While the near-axis data rolls off with angle in close agreement with the predictive performance model, once the mid -10^{-10} range is reached, all the data looks alike. Both the abruptness of the slope change and the replicated variations beyond 10° dictate the conclusion that background scatter is limiting the measurements at this point, better than two orders above the detector preamp noise floor.

The near-axis measurement limit is influenced by two factors: the use of the lens assembly as the final converging element and the position of the source-defining iris. The former affects the measurements since all specular rays passing through the $4.8^\circ \times 6.5^\circ$ field stop also pass through the lens. The image of the source, many orders higher in power than the rejected component, generates considerable forward scatter within the multi-element lens assembly and as such overpowers the rejection level. The source-iris causes both diffuse and "specular" scatter at its edges. As such, as long as its edges are within the sensor's field of view, radiation not associated with the collimated off-axis source is introduced through the sensor down onto the focal plane. Prior experience has demonstrated that this contribution can be much higher than the seven-orders attenuated source. As a result, the near-axis limit is defined to be that angle at which the trailing edge of the sensor's field of view goes off the source iris. This angle is a function of both the sensor configuration and the test facility geometry. For our situation, this limit is 4.2° in azimuth and 3.4° in elevation. The 4° azimuth data has been presented, however it must be considered higher than the true performance characteristics.

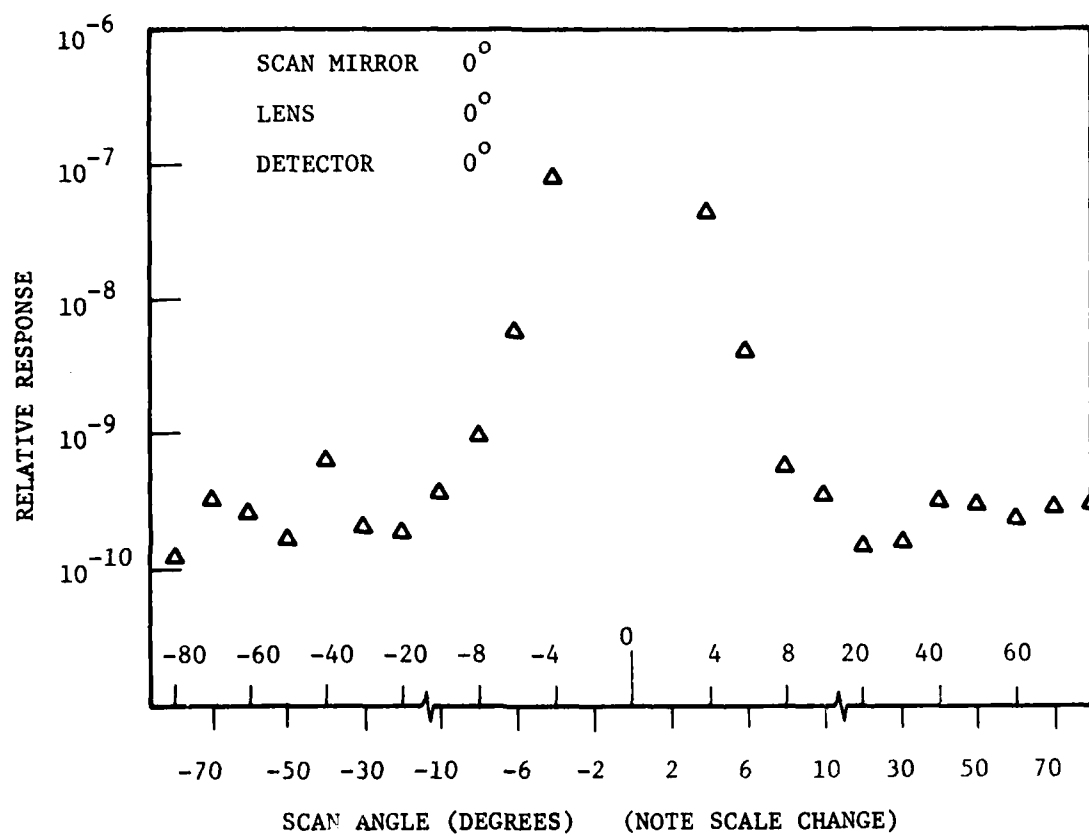


Figure 1 SPATIAL RADIOMETER OFF-AXIS REJECTION AZIMUTH SCAN

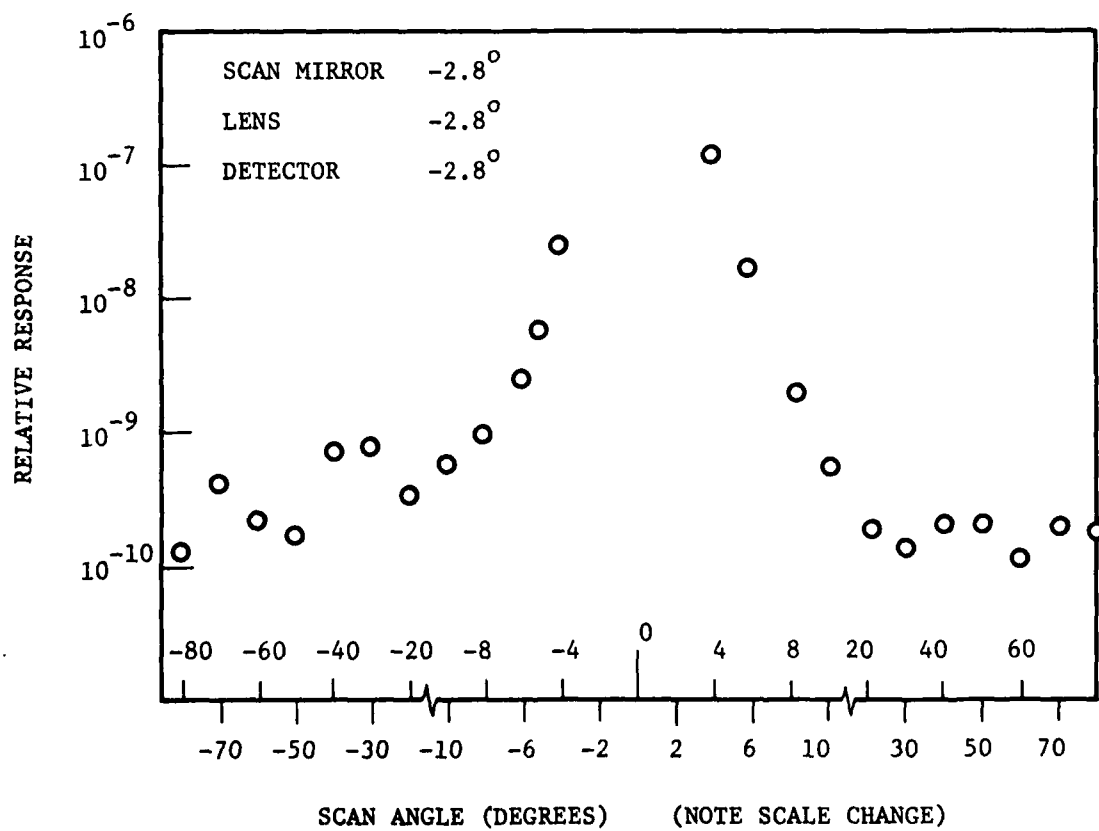


Figure 2 SPATIAL RADIOMETER OFF-AXIS REJECTION AZIMUTH SCAN

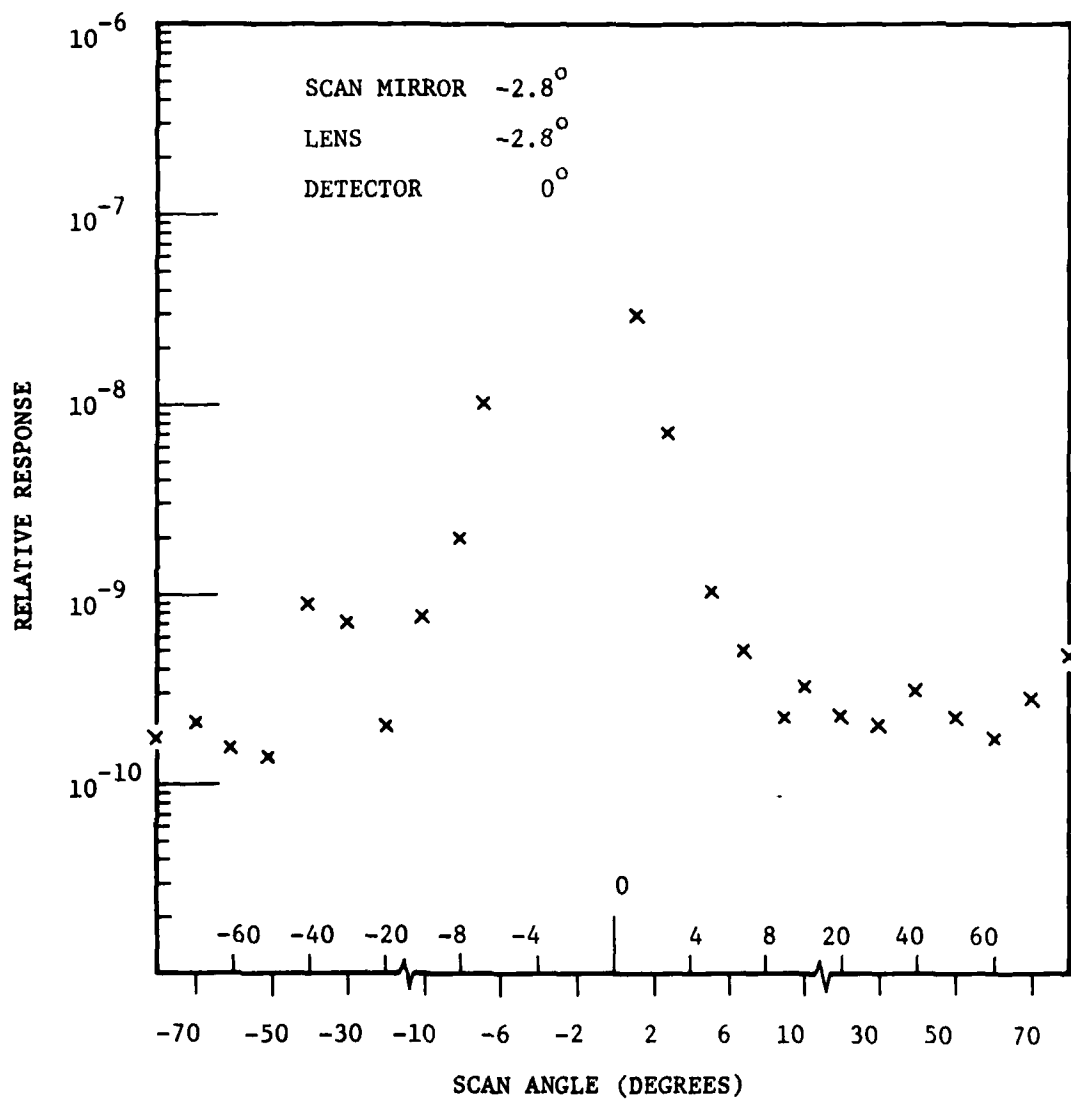


Figure 3 SPATIAL RADIOMETER OFF-AXIS REJECTION AZIMUTH SCAN

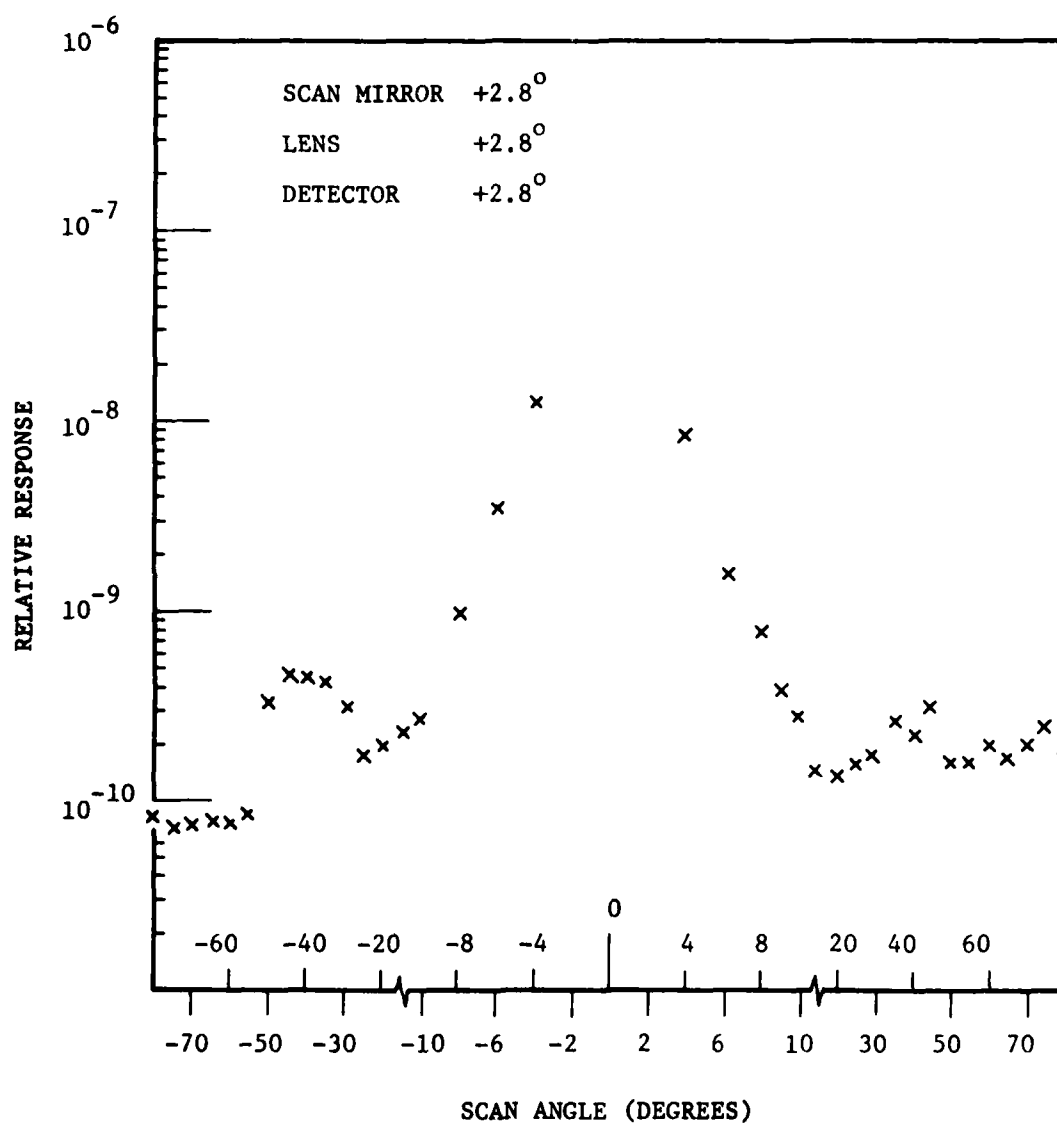


Figure 4 SPATIAL RADIOMETER OFF-AXIS REJECTION AZIMUTH SCAN

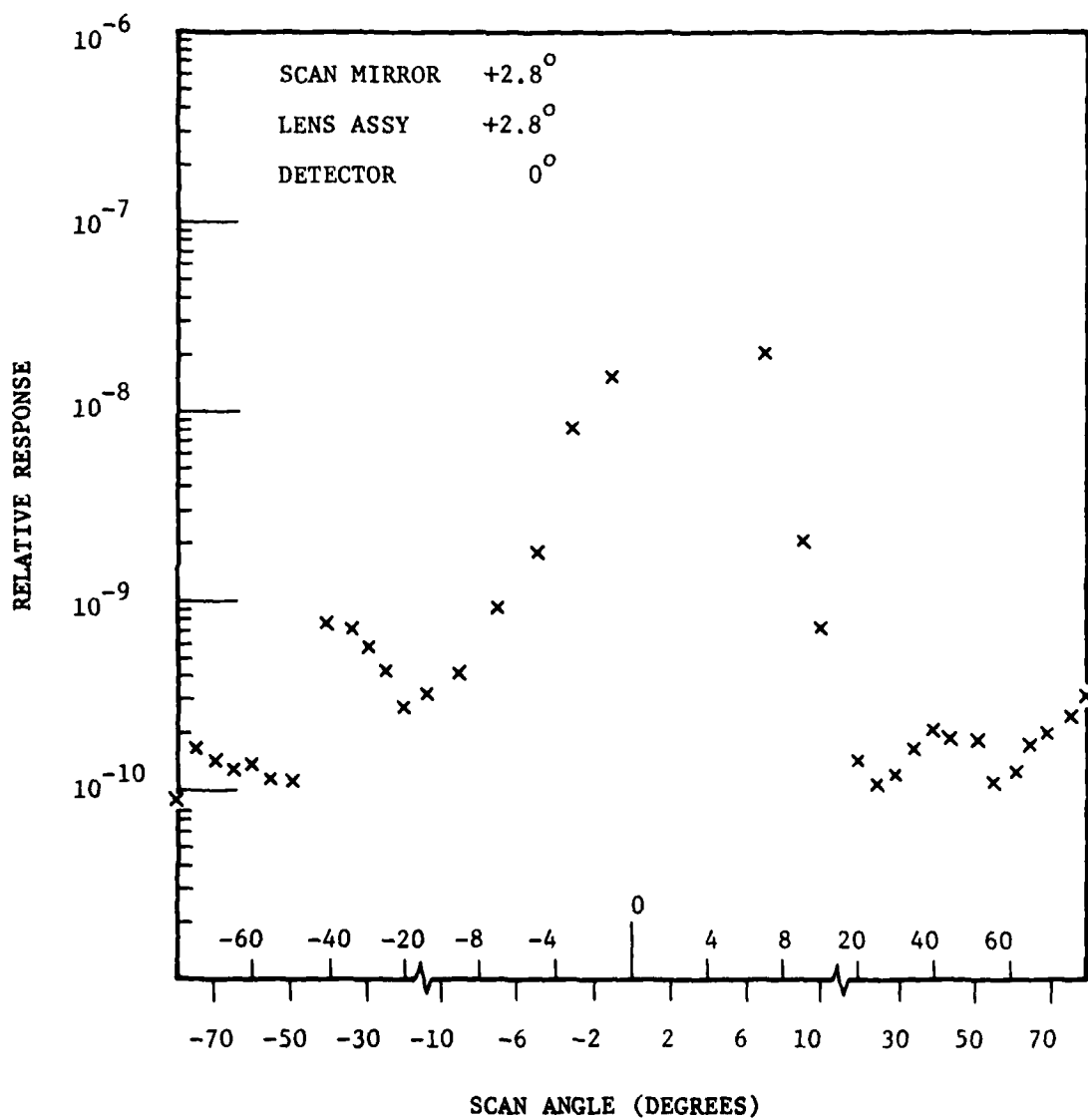


Figure 5 SPATIAL RADIOMETER OFF-AXIS REJECTION AZIMUTH SCAN

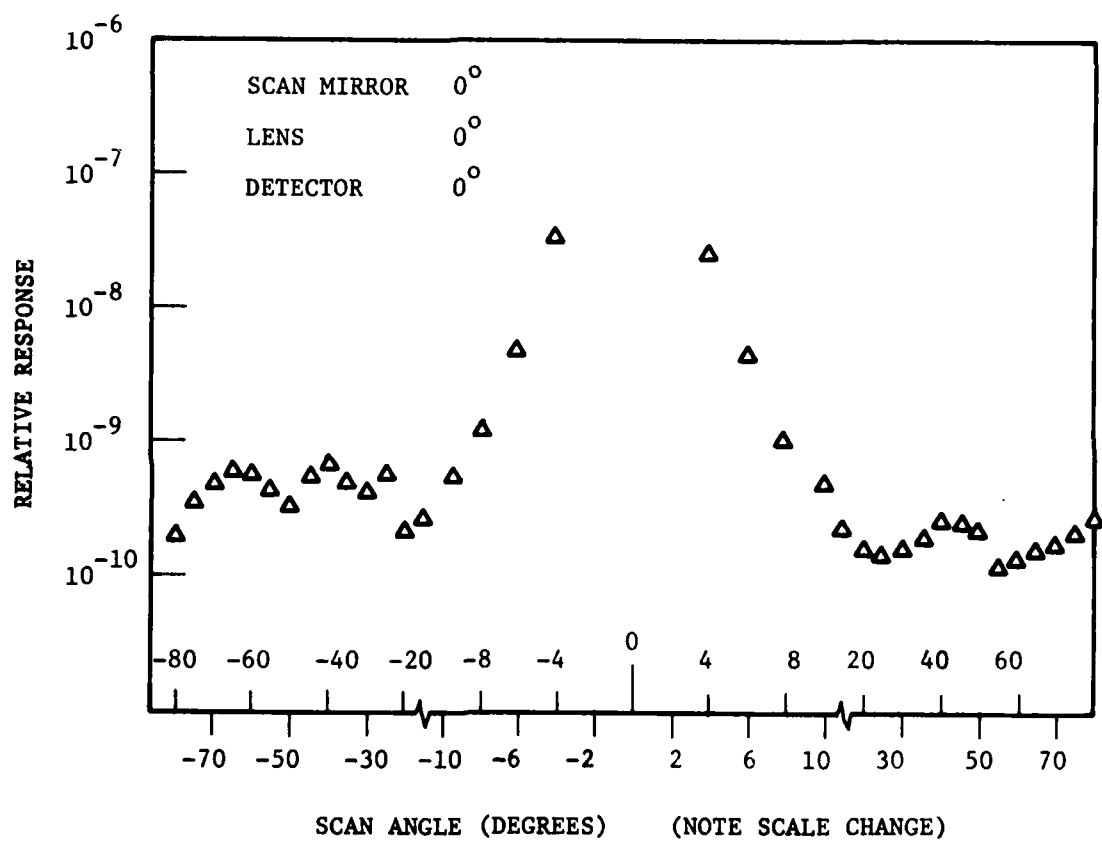


Figure 6 SPATIAL RADIOMETER OFF-AXIS REJECTION ELEVATION SCAN

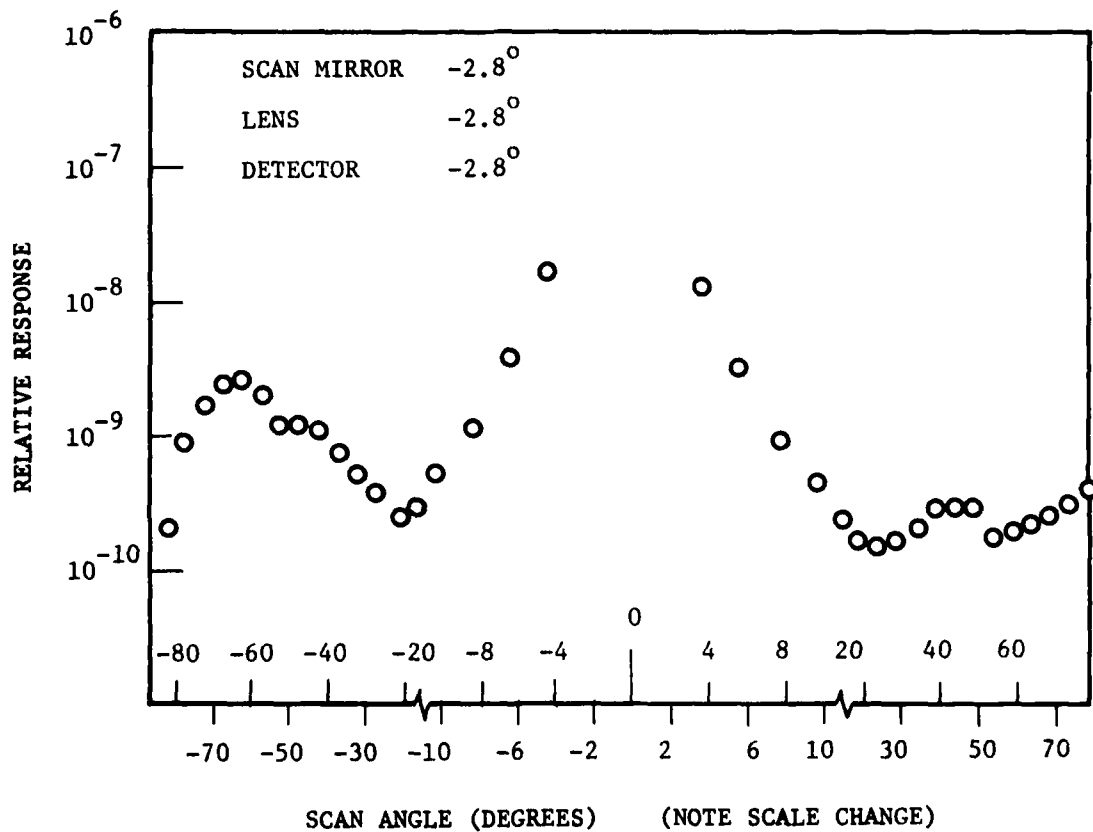


Figure 7 SPATIAL RADIOMETER OFF-AXIS REJECTION ELEVATION SCAN

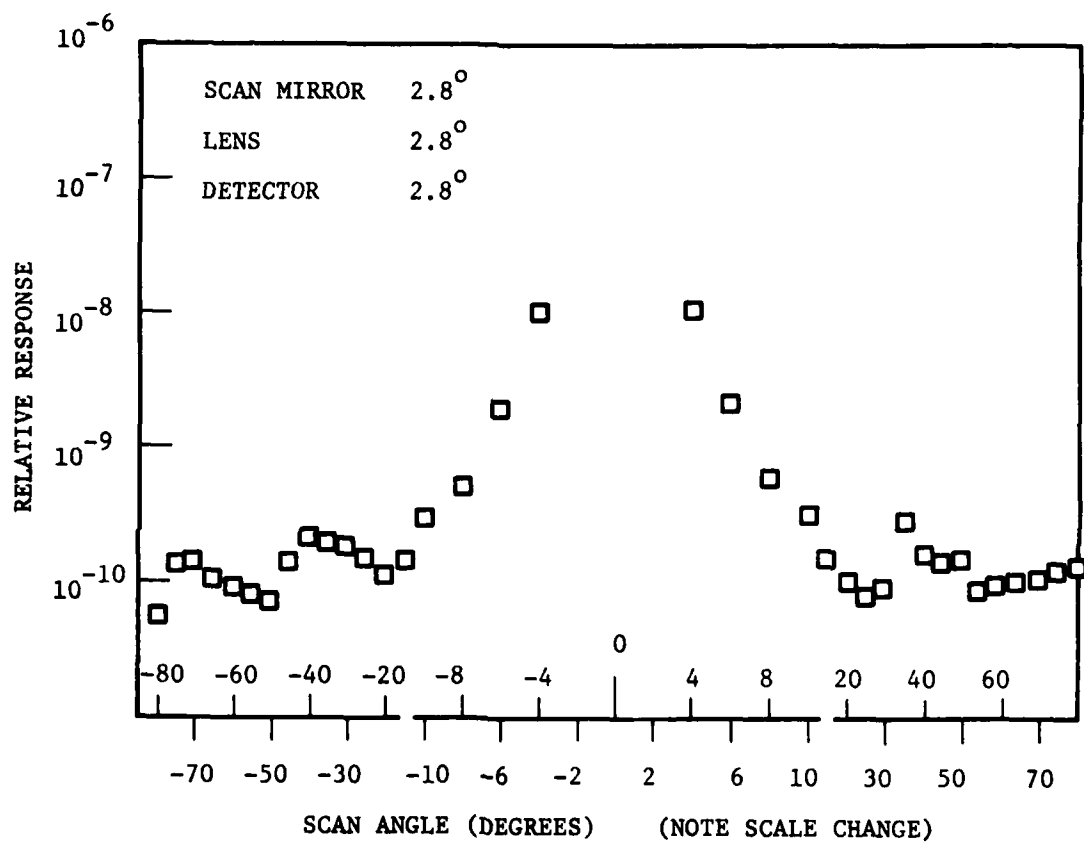


Figure 8 SPATIAL RADIOMETER OFF-AXIS REJECTION ELEVATION SCAN

In light of these facts, the data must be interpreted in the following fashion. The 4° to 10° range data are representative of the sensor performance capability. These are approximately one and one-half orders higher than the projected performance levels at 1.06 micrometers, however, their rolloff especially in the 6° to 10° range fits the projected data quite well. An extension of this $1/\theta^2$ rolloff with off-axis angle θ from the 10° data point gives a good assessment of the 1.06 micrometer sensor performance characteristics. The projected performance in terms of point source rejection for 1.06 micrometers beyond 10° and the resultant assessments for the sensor's in-band performance are shown in Figures 9 and 10. The integration of these curves weighted by the earth function over the earth's geometry provides the extended source rejections as a function of earth off-axis angle shown in Figure 11.

The resultant NEFD performance based on these data and the in-band source radiances are presented in Table 1. The required rejection sensitivities are readily satisfied in all cases except for the lower band solar rejection at 60° off axis. Based on these data two system alternatives exist: accept a 40% reduction in sensitivity for operation with the sun at 60° or structure the data acquisition for the lower band to preclude measurement with the sun within approximately 70° of the sensor boresight. The latter technique will allow for recovery of the required sensitivity.

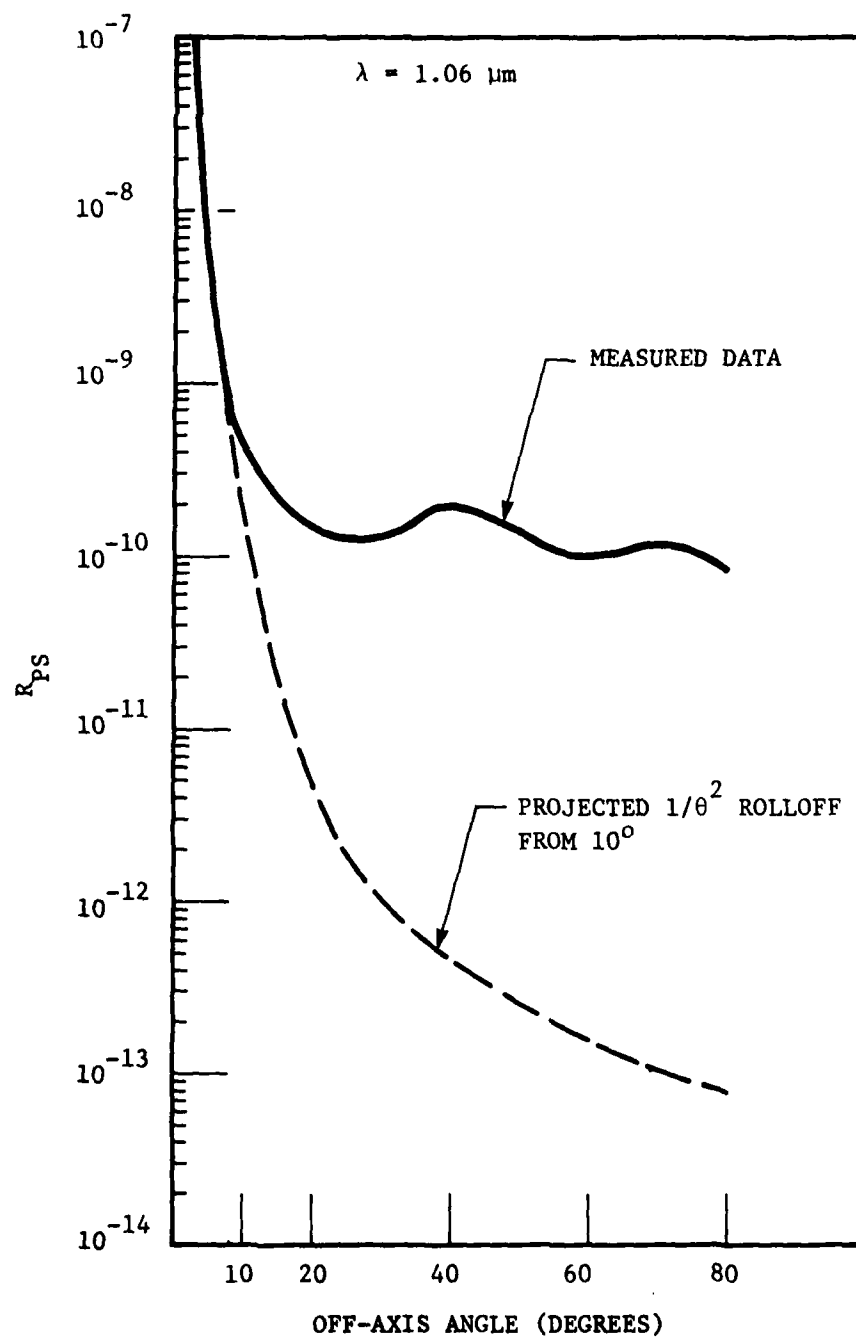


Figure 9 POINT SOURCE REJECTION VERSUS OFF-AXIS ANGLE

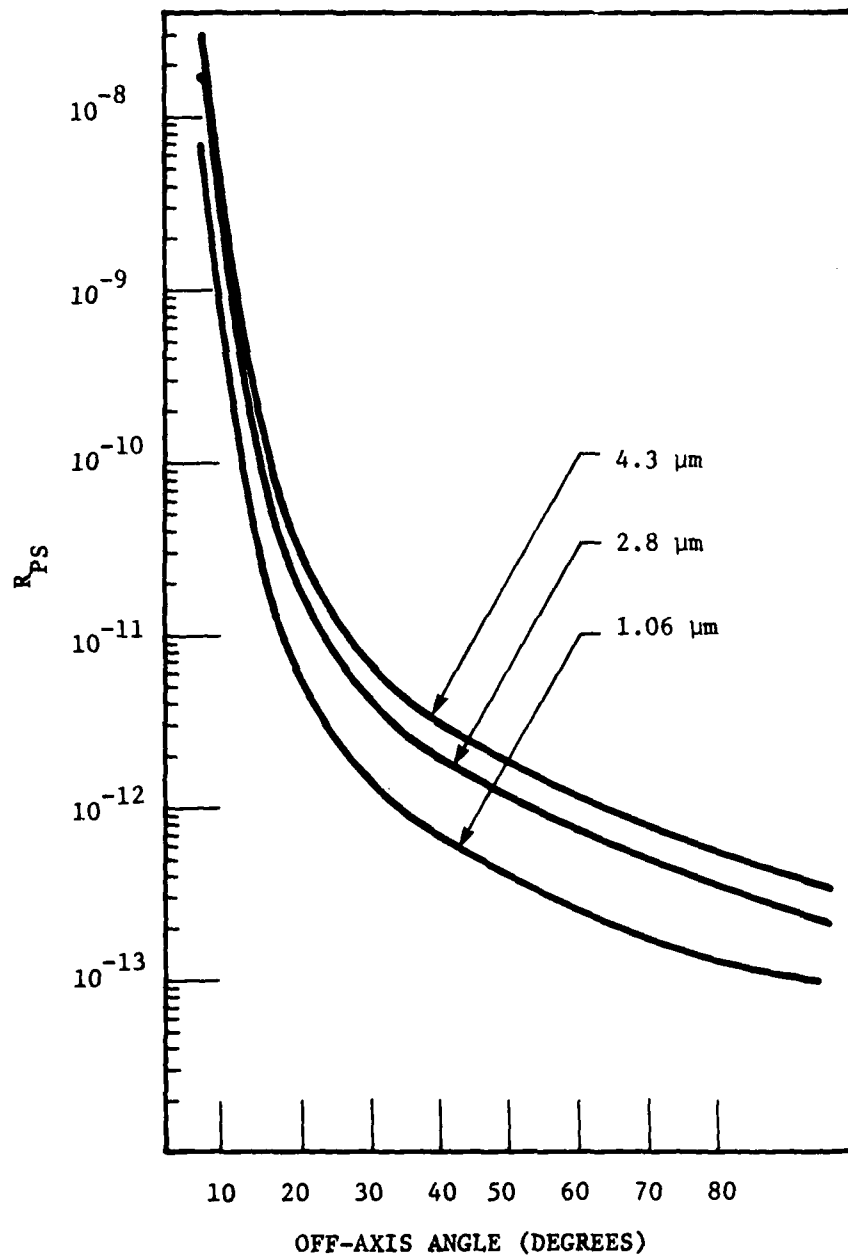


Figure 10 POINT SOURCE REJECTION (IN-BAND) VERSUS OFF-AXIS ANGLE

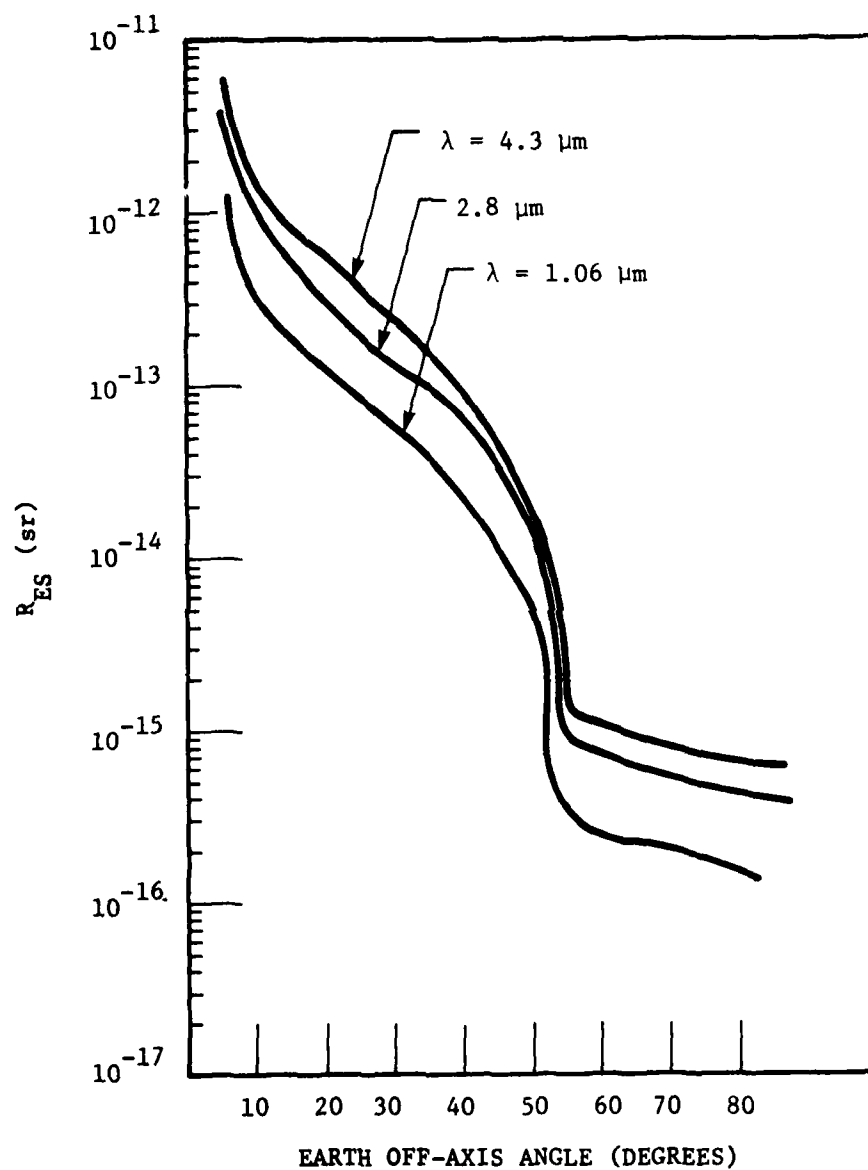


Figure 11 EXTENDED SOURCE REJECTION VERSUS OFF-AXIS ANGLE (EARTH GEOMETRY)

Table 1
SPATIAL RADIOMETER REJECTION SENSITIVITY PERFORMANCE

| | SW MICROMETERS | MW MICROMETERS |
|--------------------------------------|-------------------------|-------------------------|
| Earth Source - 30°: | | |
| R _{ES} (sr) | 1.4 x 10 ⁻¹³ | 2.5 x 10 ⁻¹³ |
| Measured NEFD (W/cm ²) | 1.0 x 10 ⁻¹⁹ | 6.8 x 10 ⁻¹⁸ |
| Required NEFD (W/cm ²) | 4.9 x 10 ⁻¹⁶ | 4.8 x 10 ⁻¹⁶ |
| Measured NER (W/cm ² -sr) | | |
| Near-field | 4.1 x 10 ⁻¹⁴ | 2.8 x 10 ⁻¹² |
| Far-field | 2.0 x 10 ⁻¹⁵ | 1.4 x 10 ⁻¹³ |
| Solar Source - 60°: | | |
| R _{PS} | 7.2 x 10 ⁻¹³ | 1.2 x 10 ⁻¹² |
| Measured NEFD (W/cm ²) | 6.9 x 10 ⁻¹⁴ | 2.1 x 10 ⁻¹⁶ |
| Required NEFD (W/cm ²) | 4.9 x 10 ⁻¹⁶ | 4.9 x 10 ⁻¹⁶ |
| Measured NER (W/cm ² -sr) | | |
| Near-field | 2.8 x 10 ⁻¹⁰ | 1.8 x 10 ⁻¹⁰ |
| Far-field | 1.4 x 10 ⁻¹¹ | 4.3 x 10 ⁻¹² |

SECTION VII

CRYOGENIC DESIGN AND TEST RESULTS

SUMMARY

Reference Document No. 061576-0005 and No. 061576-0006

The above two documents include the test plan and results on system no. 1. The complete documents are included in Volume II of this report. Page numbers have been changed to conform to this report.

1.0 INTRODUCTION

1.1 Acceptance Criteria

Acceptable thermal performance criteria shall be determined on the basis of the thermal measurements.

1.2 Authority

This test will be performed under authority of Contract No. F19628-75-C-0179.

2.0 TEST OBJECTIVES

The test objectives are as stated below:

1. To determine the thermal performance of sensor during the ground hold period and during a simulated entrance heat load.
2. Obtain parametric thermal data on the focal plane and the scan motor.

3.0 TEST PROGRAM

3.1 Test to be Performed

3.1.1 Cool down time of the sensor.

3.1.2 Flow rate and sensor temperatures during a ground hold period.

3.1.3 Flow rate and sensor temperatures for 3 heat loads on the focal plane and 3 heat loads on the scan motor. Temperature data to be sampled every 10 minutes until steady state conditions are achieved, see data sheets (Section 6.0 ref.).

3.1.4 With a simulated earth load applied to aperture section of the telescope, determine the maximum structural temperature of the sensor just after it has been depleted of liquid nitrogen. Scan motor and focal plane shall be energized.

3.2 Test Duration

Each test will be continued until steady state conditions are reached.

3.3 Instrumentation Calibration and Readout

All temperature sensors except at the door plate in the spatial radiometer sensor are matched at three points (LHe, LN₂, and room temperature). The matching is within ± 2.75 MV at LN₂. The door plate sensor is calibrated every degree from 4.2°K to 30°K, every 2° from 40°K to 75°K, and every 10° from 80° to 300°K.

A mass flowmeter will be used to determine the nitrogen flow rate in scc/min. The expected error is $\pm 1\%$ of the instrument range (0-50,000 scc/min) for a 20% variation in pressure and temperature.

3.4 Environmental Test Conditions

Environmental temperature of the sensor unit shall be at room temperature and the sensor/telescope shall be at liquid nitrogen temperature. The test vacuum shall be less than 1×10^{-5} Torr.

3.5 Equipment Functional Check and Verification

Following assembly of necessary test and monitoring equipment the plumbing shall be leak checked. The thermometry shall be checked for electrical continuity and temperature response. Mass flowmeter used for measuring the mass flow rate shall be checked for proper hook-up to the sensor. Refer to Figure 3.5 for thermal test set-up schematic.

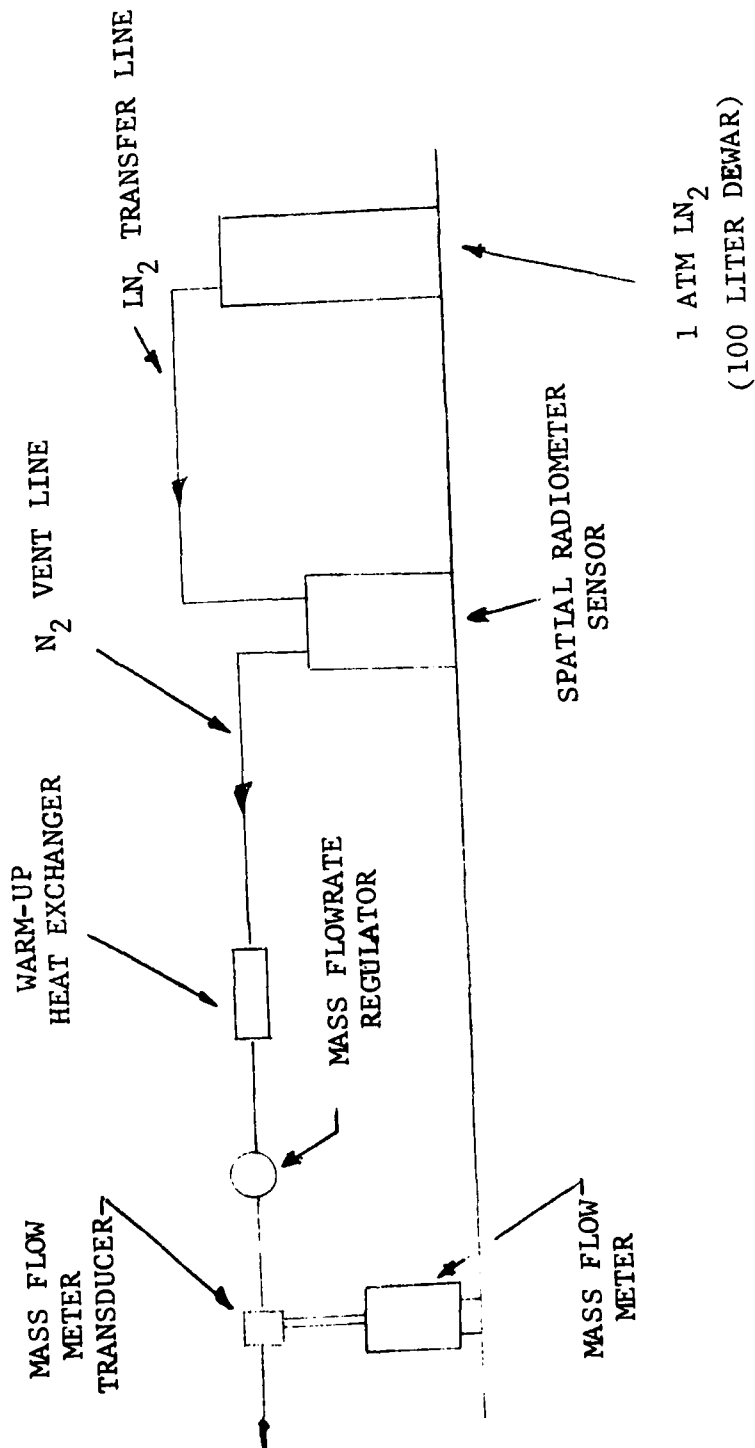


FIGURE 3.5
SCHEMATIC OF TEST SET-UP

3.6 Test Monitoring and Data Recording

Test data sheets will be used to record all measurements.

3.7 Test Report and Data Review

At the conclusion of testing the test data shall be reviewed by engineering. A test report containing test data, analysis of data, and acceptable thermal performance shall be published following this effort.

4.0 INSTRUMENTATION

The following instrumentation shall be used to measure, monitor and record data.

4.1 Lakeshore Cryotronics Temperature Diodes

There are 10 silicon diodes, model number DT-500K-T05 which are located at the following places:

1. Telescope - front, upper left
2. Telescope - front, middle
3. Telescope - front, lower right
4. Telescope - front, upper inside right
5. Telescope - back, lower left
6. Telescope - back, upper right
7. Scan motor mounting flange
8. Scan motor
9. Focal plane
10. Door plate

4.2 Hastings Digital Mass Flowmeter

Model No. NALL-50-KPG Serial No. 63, using Hastings Mass Flow Transducer Model No. H-50K serial number 2973, calibrated for nitrogen gas.

5.0 TEST EQUIPMENT

The following items of test equipment of their functional equivalents will be used to perform the test outlined in this plan:

1. Spatial Radiometer Sensor
2. Liquid Nitrogen Supply Dewar
3. Vacuum Jacketed Transfer Line
4. Vacuum Pumping Station
5. AGE Power Supplies
6. Temperature Sensor Electronics

6.0 RESULTS

The raw data from the tests performed on the spatial radiometer sensor are presented in Table II. Table I correlates the case number to the parametric powers applied to the various components. The first line data on Table II (time = 10:20) are the typical temperatures for the various components and structure during a ground hold period with no power applied. Figure 1 shows the output voltage of the mass flowmeter plotted as a function of time by a Brush recorder. The typical time for cool down of the sensor from room temperature till it is topped off with LN_2 is approximately one half hour. The average flow rate during the ground hold period is 0.042 gm/sec, which is equivalent to a total heat load of 8.4 watts. Results of Case 1 (Table II) reflects the typical temperatures of the structure and components during the ground hold period with expected power dissipations for the various components. The hold time for the present sensor is approximately 22 hours.

Figures 2 and 3 present the scan motor and focal plane temperatures as a function of input power. These plotted results were taken from Table II.

TABLE 1

TEST CASES FOR PARAMETRIC STUDY
OF FOCAL PLANE AND SCAN MOTOR

| TEST CASE | COMPONENT POWER (WATTS) | | |
|--------------|-------------------------|----------------|-----------|
| | Scan Motor | Focal Plane | Blackbody |
| 1 | 0.02 | 0.08 | ON |
| 2 | 0.10 | 0.08 | ON |
| 3 | 0.20 | 0.08 | ON |
| 4 | 0.02 | 0.10 | ON |
| 5 | 0.02 | 0.15 | ON |
| 6 | 0.02 | 0.04 | ON |
| 7 | 0.0 | 0.0 | 0.0 |

(Expected
Values)

0.05 mm/s

0.01 VOLTS/LINE

1 VOLT = 7.13×10^3 SCC/min

7.13×10^3 SCC/MIN = 0.135 gm/s

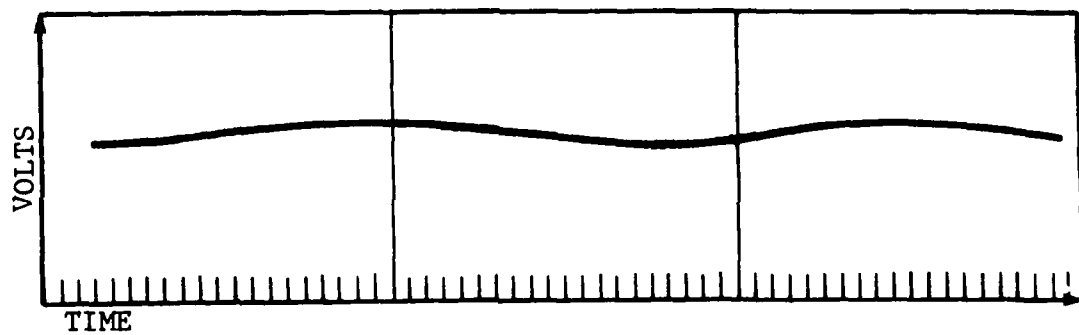


Figure 1 TYPICAL MASS FLOWRATE VS TIME

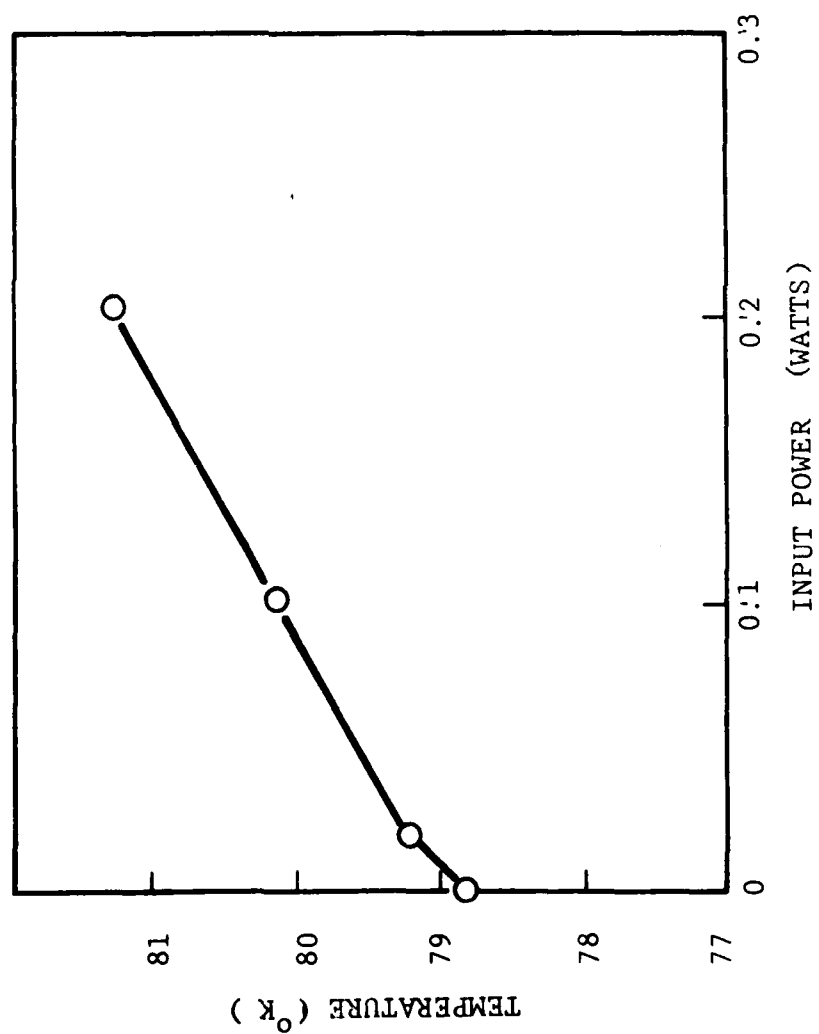


Figure 2 SCAN MOTOR TEMPERATURE VS INPUT POWER

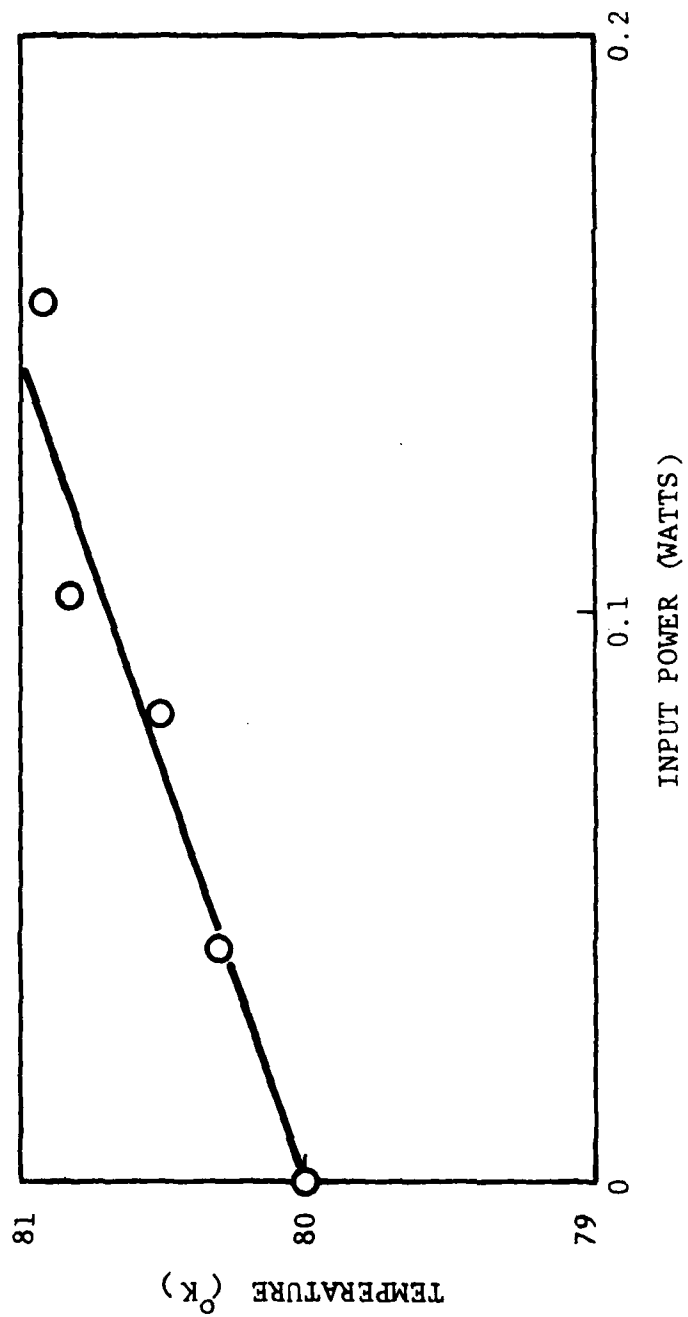


Figure 3 FOCAL PLANE TEMPERATURE VS INPUT POWER

7.0 DISCUSSION AND CONCLUSIONS

The long ground hold period experienced by the spatial radiometer is due to two reasons.

- a) The tank volume is approximately 3.7 times as large as was originally specified. The increased tank size was employed because of the ease of manufacturing and because it also helped distribute the LN_2 uniformly over the structure.
- b) The expected heat load of 12.47 watts is down to 8.4 watts. The reduced heat load is largely attributed to the increased performance of the MLI above what was anticipated. Also the penetration gaps in the MLI were minimized below the original expected values.

Therefore, multiplying the original ground hold period by the ratio of tank volume and the ratio of heat loads, one finds that the expected hold time is 22 hours. Measurements show a hold time of 21.7 hours.

This is in good agreement with the new expected value.

Temperatures of the structure during a ground hold period with no internal power dissipation are slightly elevated above the normal boiling point of LN_2 approximately 2K. This is due the pressure value on the vent for the tank. It is set at a pressure of 4 psi above the atmosphere and this pressure corresponds to an LN_2 boiling point of 79.5K. Temperatures of the structure and components during ground hold period with the expected power dissipations are within normal operating ranges. The temperature rise of the scan motor and focal plane as a function of power do not reflect a severe temperature rise for such large power dissipations. Compare expected values with the maximum values applied (see Table 1).

7.1 Conclusions

The conclusions reached as a result of the spatial radiometer thermal tests are:

- a) The 4 hour ground hold requirement is met.
- b) The thermal performance of the spatial radiometer meets and/or exceeds its expected design performance.
- c) The focal plane and scan motor are adequately heat sunk to the structure.

8.0 FUTURE THERMAL TESTING

A future thermal test of the spatial radiometer will be performed. This test will determine the structural and components temperatures during a simulated flight with the maximum earth and solar load applied to the telescope for a flight period of 600 seconds. The test will be conducted just after the sensor is depleted of cryogen.

SECTION VIII

STRUCTURE DESIGN ANALYSIS

SUMMARY

This section will include a portion of the Design Analysis Report. A complete copy of the report is included in Volume II. The page numbers have been changed to conform to this report.

1.0 CRYOGENIC TANK

The cryogenic tank received the most attention since the structural modification required that the side walls of the telescope also serve the purpose of being integral parts of the cryogenic tanks.

To assess the inherent problems associated with this design, an analysis of the cylindrical walls of the cryogenic tank was performed assuming that the cylindrical shell walls were fixed at the side wall-cylinder juncture. This analysis is contained in Appendix A and indicated extremely high stress levels at the juncture for a one atmosphere internal pressure.

Since the results of the initial analysis (see Appendix A) clearly indicated a potential problem in the design of the cryogenic tank, a more detailed investigation was required. Hence, a two-dimensional (3 DEGREE OF FREEDOM) finite element model of the cryogenic tank was generated and input to the Stardyne Structural Analysis Program. The Finite Element Model used is shown in Figure 1.

Because the behavior of the tank depended on the constraint offered by the top and bottom covers against lateral motion, the following conditions were investigated:

Case 1: Covers "effective" in constraining lateral motion.

Case 2: Covers not effective in constraining lateral motion.

The tank distortions resulting from the boundary conditions imposed in cases 1 and 2 are shown in Figures 2 and 3 respectively.

For both cases the maximum stress occurred in the 1/8" side wall of the telescope, and are given below for an 18 psi internal pressure.

Case 1: $\sigma = 15130$ psi

Case 2: $\sigma = 24138$ psi

FIGURE 1
CRYO TANK STRUCTURAL MODEL

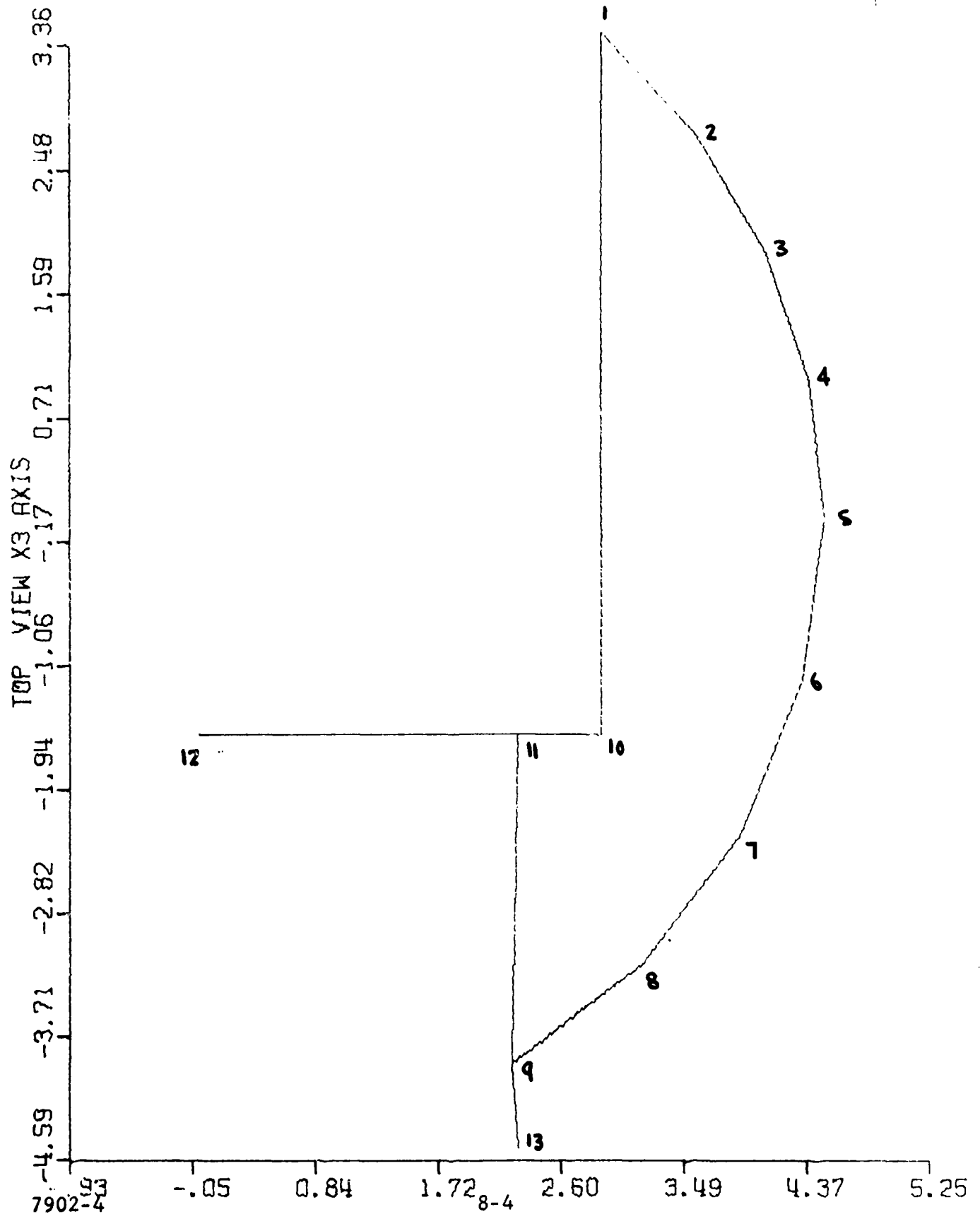


FIGURE 2
CRYO TANK DEFORMED SHAPE

2

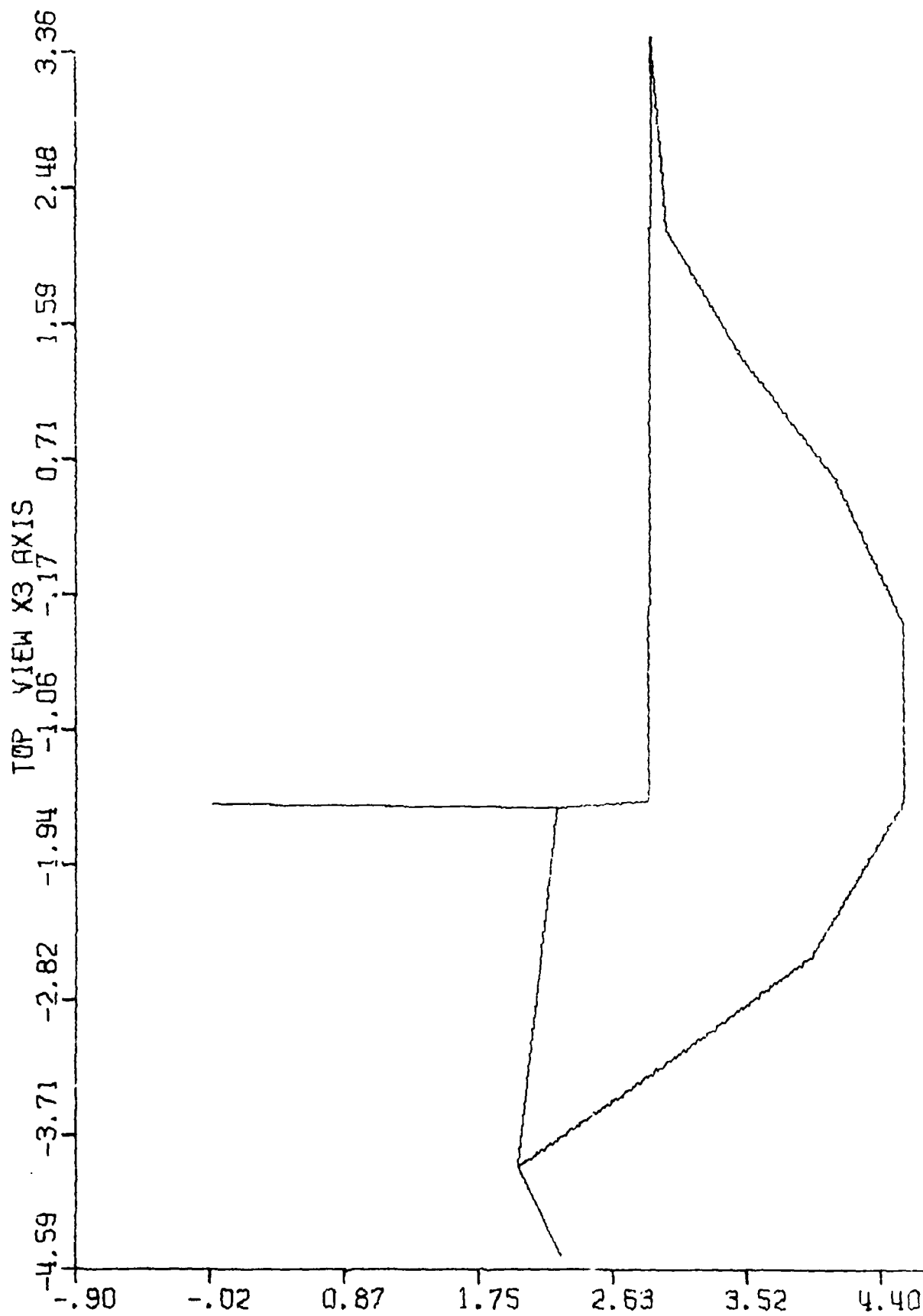
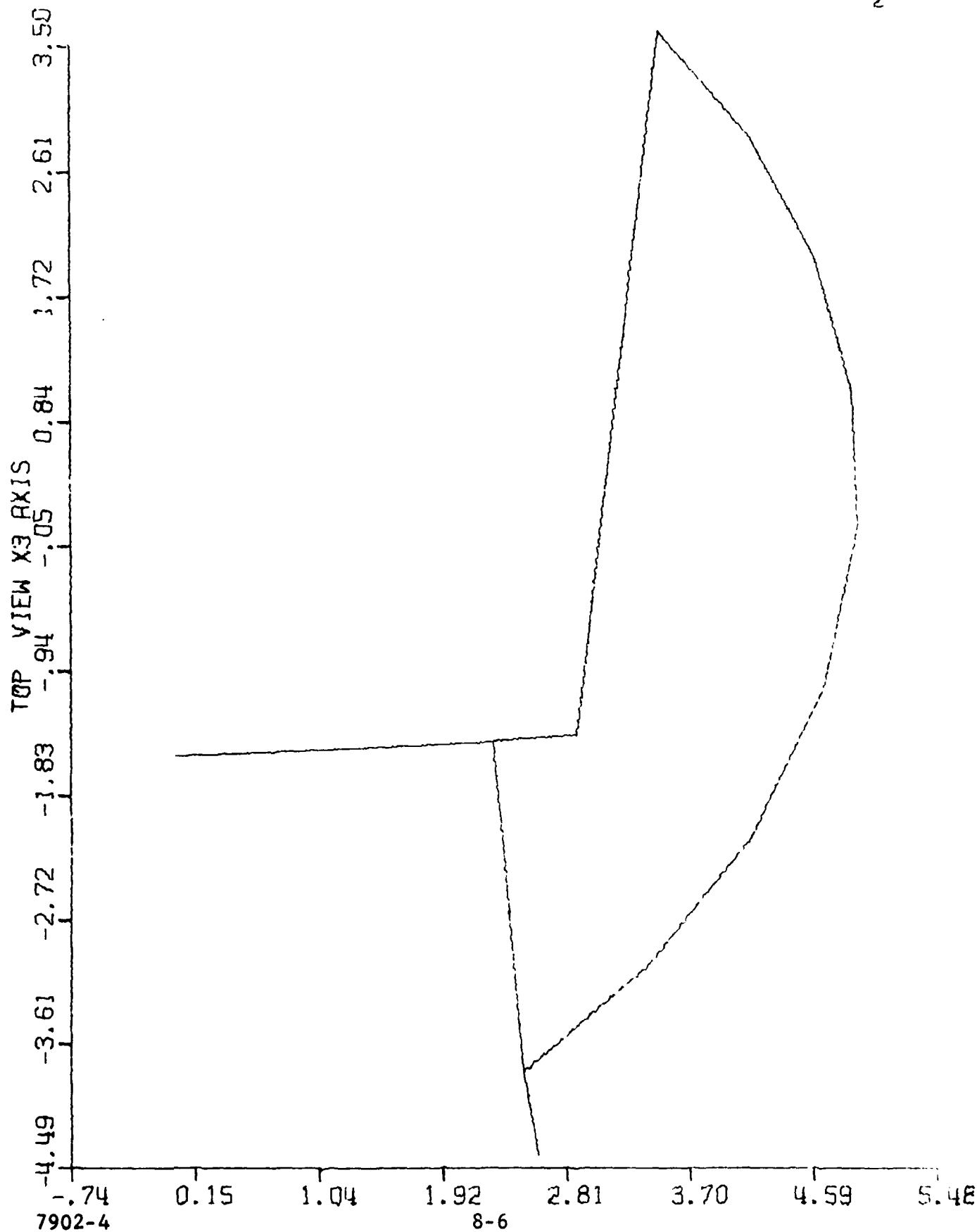


FIGURE 3
CRYO TANK DEFORMED SHAPE

2



The results of cases 1 and 2 analyses indicated that the tank configuration as designed was unacceptable.

Since baffles were required thermally to facilitate the flow of tank cryogen, it was decided to use the baffles to stiffen the tank by arranging the hole pattern in the truss configuration, shown in Figure 4. A two-dimensional Stardyne analysis was then performed on the modified cryogenic tank stiffened by baffles spaced 2.2" on center.

Figures 5 and 6 show the finite element truss model in its undeformed and deformed states respectively.

The results of the analysis show that the stress levels in the cylindrical and telescope walls were reduced significantly due to the addition of the baffles. A maximum stress of 2850 psi occurs in the cylindrical shell wall (at the juncture) due to an internal pressure of 18 psi.

Although the structural integrity of the cryogenic tank appears assured as a result of the above analysis, the reliability of the design is dependent on the quality of the brazement between the walls and 0.1" baffle. In addition stress concentrations abound at each joint within the brazed tank. Hence, adequate inspection of the brazed joints is essential for acceptable performance.

2.0 PRESSURE VESSEL

The pressure vessel was analyzed for a one-atmosphere vacuum and a three-atmosphere design pressure.

It was found that a high margin of safety exists with respect to buckling of the cylindrical shell wall.

The discontinuity stresses at the cylinder-nozzle juncture were found to be in the order of 2500 psi for a one atmosphere pressure differential. (Appendix C.)

FIGURE 4
BAFFLE "STRUT" DESIGN

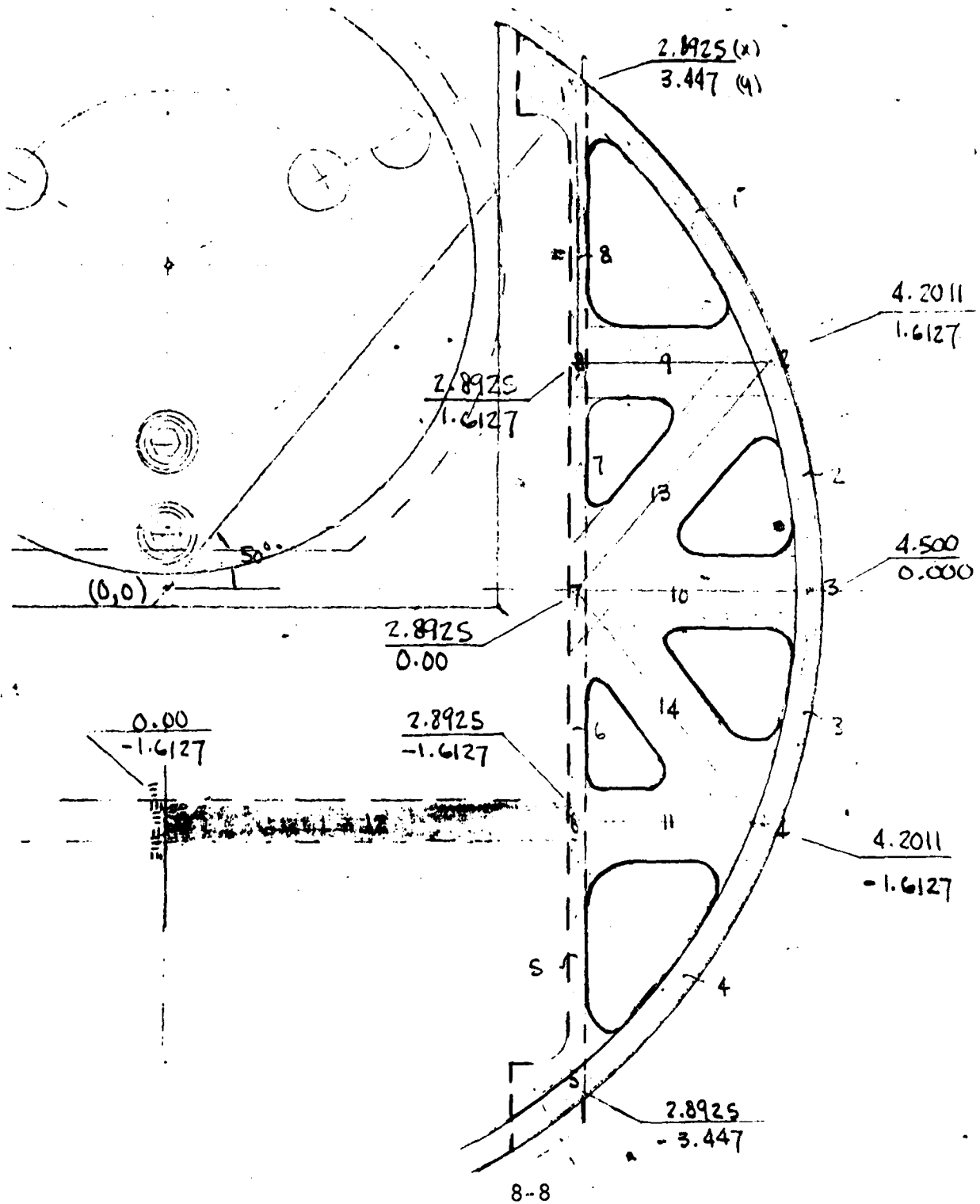


FIGURE 5
BAFFLE STRUCTURAL MODEL

TOP VIEW X3 AXIS

3.37

2.60

1.84

1.07

0.31

-0.46

-1.23

-1.99

-2.76

-3.52

-5.51

0.26

1.02

1.79

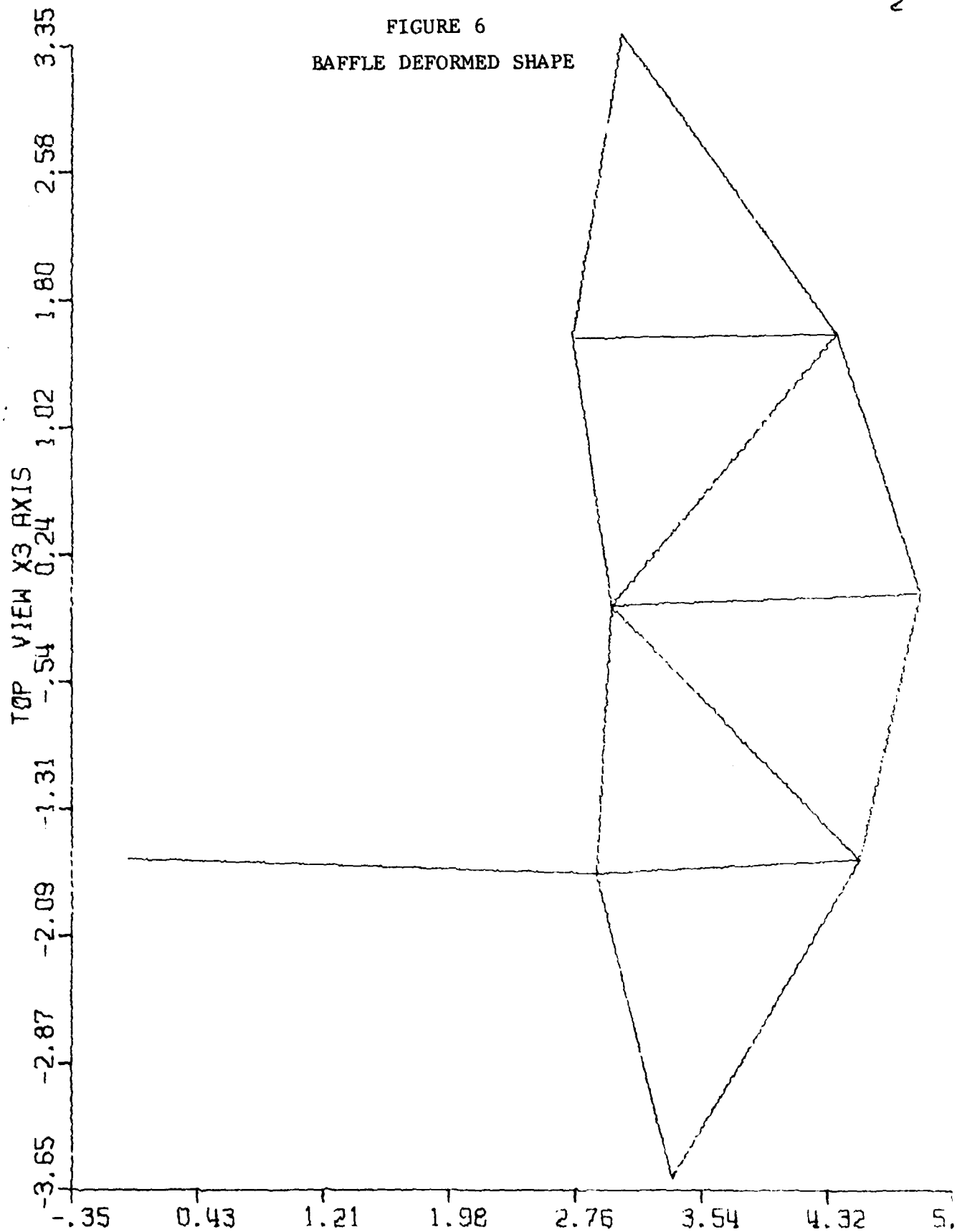
2.56

3.32

4.09

4.85

FIGURE 6
BAFFLE DEFORMED SHAPE



The front cover was not analyzed since it is identical to a previous application. In addition, the seals were not checked for leakage due to excessive deformation.

No problems are expected with the pressure vessel.

3.0 G-10 SUPPORTS

Previous experience with a G-10 cylinder bonded to an aluminum ring indicates that the most sensitive area exists at the bonded juncture (ref. Figure 7) where local discontinuity stresses arising from a thermal strain differential generally exceed primary stresses resulting from typical dynamic environments.

The local juncture discontinuity shell stress as in the G-10 were determined using programs ASSA and ARRA developed for Honeywell by EAB Associates.

The results of the analysis shown in Table 1 below clearly indicate that the G-10 Support is adequate for this application.

TABLE 1
JUNCTURE AND PRIMARY STRESSES

| LOADING CONDITION | JUNCTURE STRESSES, psi | | | | PRIMARY STRESSES, psi | |
|----------------------------|------------------------|-----------------|------------|-----------------|--------------------------|--------|
| | G-10 | | Aluminum | | G-10 | G-10 |
| | σ_x | σ_θ | σ_x | σ_θ | σ_x | τ |
| Thermal | 6500 | -3450 | 1475 | -1780 | -- | -- |
| (Assumed) 100 G Axial | 835 | -- | 6550 | -- | 2400 | -- |
| (Assumed) 100 G Lateral | 1290 | -- | 10250 | -- | 5260 | 4820 |

PROJECT NO.

EA NO.

PREPARED BY

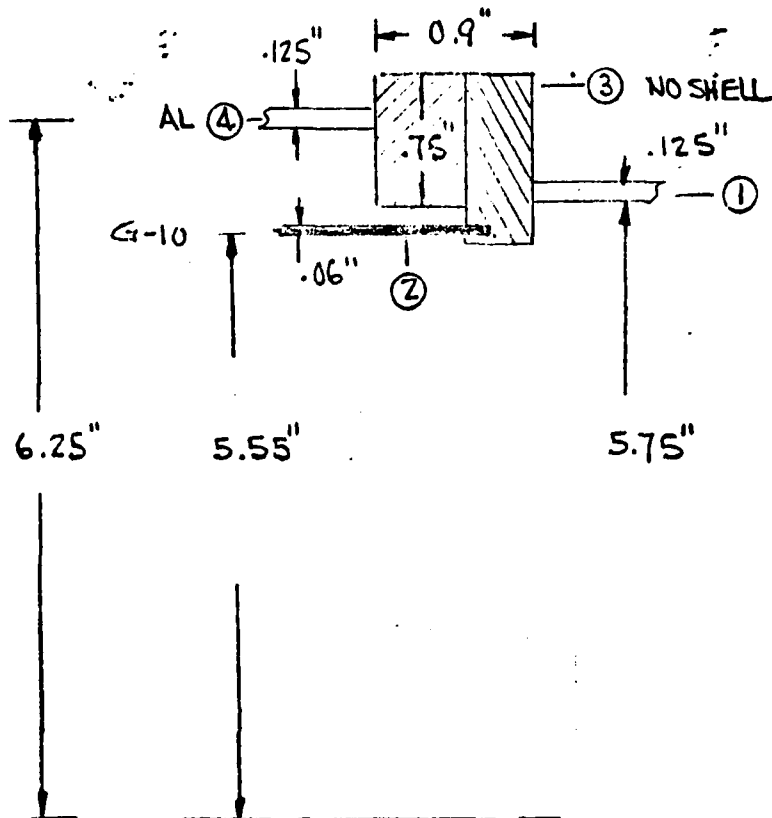
DATE

APPROVED BY

DATE

PAGE OF

FIGURE 7
BOND JOINT





ERNST, ARMAND & BOTTI ASSOCIATES, INC. • Engineers

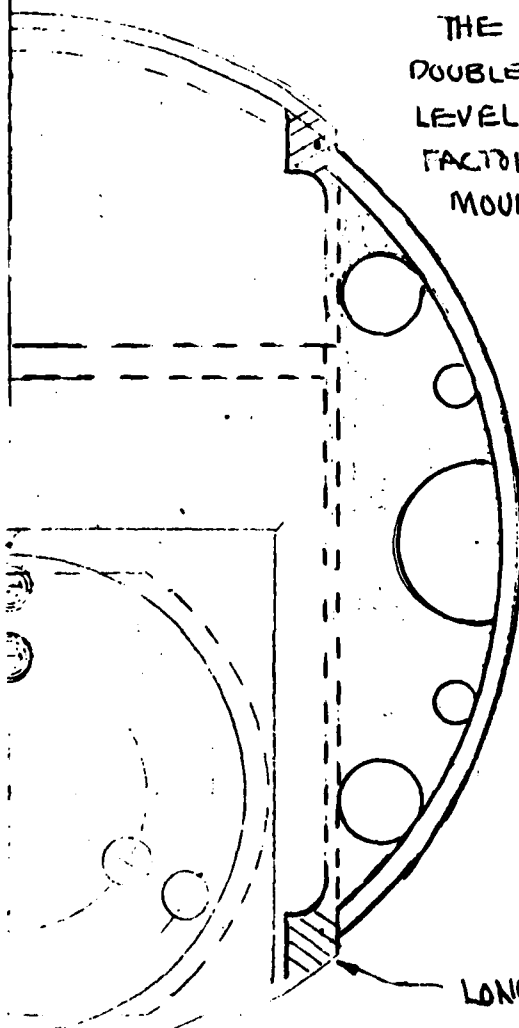
60 HICKORY DRIVE, WALTHAM, MASSACHUSETTS 02154

TELEPHONE 617/890-5179

| | | | | |
|------|--|---|--------------|--|
| By | | TITLE: <i>MTG. RING ANALYSIS</i> | Page No. | |
| Date | | | | |
| Dwg | | | Project No. | |
| | | | Proposal No. | |

4.0 MOUNTING RING ANALYSIS

THE MOUNTING RING WAS ANALYZED PREVIOUSLY IN REFERENCE ("HIGH PRECISION TELESCOPE", STRESS REPORT - UTAH STATE - 22914-01). A VERY CONSERVATIVE ANALYSIS IN THE REFERENCE REPORT (PAGE 13) INDICATES A MAXIMUM STRESS OF 3780 psi FOR A 5/8" PLATE.



THE HOLE PATTERN SHOWN SHOULD \approx DOUBLE THE PLATE FLEXIBILITY AND STRESS LEVELS. ALLOWING A STRESS CONCENTRATION FACTOR OF 3; THE MAXIMUM POSSIBLE MOUNTING RING STRESS $\approx 3780 \times 2 \times 3 \approx 22,000$ psi

HENCE; $(3780 < \sigma_m < 22,000 \text{ psi})$

NOTE THAT AN ALTERNATE LOAD PATH THROUGH THE LONGITUDINAL STIFFENERS IS AVAILABLE FOR LOAD TRANSFER FROM THE TELESCOPE TO THE DEWAR.

CONCLUSION: MOUNTING RING IS ADEQUATE FOR THIS APPLICATION BASED ON PREVIOUS ANALYSIS AND SECONDARY LOAD PATH.

LONGITUDINAL STIFFENERS

SECTION IX

INTERNAL CALIBRATION

1.0 GENERAL DESCRIPTION

1.1 The blackbody assembly consists of a blackbody cavity mounted into a housing with a nichrome wire heater and two thermistors used in the control circuit. The assembly is then mounted into a blackbody housing and lens mount.

1.2 The hot wire assembly is a miniature tungsten lamp with the outer glass shell removed. The tungsten wire and base portion of the lamp assembly is then potted into a housing that completes the hot wire assembly.

2.0 OPERATION

2.1 The blackbody assembly is turned on by command from the electronics and requires at least 5 minutes for warm up. The radiation from the blackbody is collimated through the silicon lens, reflected off a small fold mirror attached to the front cover, and directed into the optical train and brought to a focus on the detector array by the M4 mirror.

Using a 300°K blackbody, the power reaching the focal plane is 1.039×10^{-10} watts/cm²/Ω in the SW micron band and is 4.2×10^{-9} watts/cm²/Ω in the MW micron band.

Prior to the cover removal after launch the blackbody will be used for calibration measurements. When the cover is removed the small fold mirror attached to the cover is also removed and the blackbody will then be turned off for the remainder of the flight.

2.2 The hot wire calibration source will be used in addition to the blackbody source during the pre-mission phase. It will be turned on to check the signal level, transient response and gross calibration. The hot wire will be functioned when the scan mirror is in

the middle of its travel and the blackbody turned off. The post-cover removal checks will be accomplished in the same sequence as that used during pre-mission with the exception that the sequence will be used only during the interval between target engine burns. The power reaching the focal plane using a hot wire is $.7 \times 10^{-7}$ watts/cm²/Ω in the SW micron band and is 2.69×10^{-6} watts/cm²/Ω in the MW micron band.

SECTION X

FOCAL PLANE DESIGN

SUMMARY

This section will cover the Focal Plane Design and construction including test results. Due to the classification requirements certain data areas will be omitted from this report.

1.0 INTRODUCTION

The spatial radiometer focal plane contains forty high performance (Hg, Cd) Te detectors. The forty elements are divided into two twenty element arrays. One of these arrays must be sensitive to radiation in the short wave band while the other twenty element array is sensitive to radiation in the medium wave band. For simplicity, we will refer to the Short Wavelength Band as SW, and the Medium Wavelength Band as MW. In each of the arrays there are ten large elements ($0.021'' \times 0.021''$) and ten small elements ($0.0105'' \times 0.002''$). These give the focal plane optimized resolution in both the far and near field respectively. The resultant near field IFOV is $.2^\circ \times .04^\circ$ or $3.5 \times .7$ milliradians. The far field IFOV is $.4^\circ \times .40$ or 7×7 milliradians.

The focal plane assembly is built on the detector plate. The arrays on their own semicircular circuit boards are mounted on the center of the detector plate. This plate is in the optical path and has a central disc and four slender spokes. The disc is just large enough for the two arrays with filters and electrical connections. The spokes support the tape cables. In this way a minimum obscuration is introduced into the optical path.

(Hg, Cd) Te detectors are being utilized for the spatial radiometer sensor because of their variable bandgap properties and their high sensitivity under reduced background conditions.

$(\text{Hg}_{1-x}\text{Cd}_x)\text{Te}$ is a pseudo binary alloy which can be grown with any desired ratio of Cd to Hg. As the percentage Cadmium increases the energy gap increases and the cutoff wavelength of the resultant IR detector decreases. The variation in cutoff wavelength as a function of composition (x-value) and wavelength are well known in the composition range of interest. Detectors can be tailor-made for each wavelength band by using an appropriate composition of $\text{Hg}_{1-x}\text{Cd}_x\text{Te}$ as the starting material. The background photon flux for

the system is assumed to be 1×10^9 photons/cm²/sec or less. At such a low photon flux only the most sensitive detector materials can come close to the background limited detectivity. (Hg, Cd) Te has demonstrated this exceptional sensitivity both before and during the Spatial Radiometer Program. In addition, the far field detectors require the highest detectivity. The far field detectors are very large 0.021" x 0.021" and require a region of (Hg, Cd) Te over 0.2" which has uniform, very high sensitivities. This achievement of high detectivities in large elements over the full ten elements has been a major accomplishment to date in the spatial radiometer focal plane.

This design report will discuss in more detail in the succeeding sections the focal plane characteristics required to meet sensor requirements, the mechanical layout and electrical connection and supportive test data as available at the time of this report (depending on classification of material).

2.0 FOCAL PLANE CHARACTERISTICS

The design of the spatial radiometer array is the first step in assuring that the detectors will meet the sensor requirements. The near and far field requirements and spatial resolution are addressed by using 0.021" x 0.021" elements for the far field and 0.0105" x 0.002" elements for the near field. The detectivities required for the far and near field elements are 2.0×10^{13} cmHz^{1/2}/watt and 2×10^{10} cmHz^{1/2}/watt respectively. These detectivities correspond to Noise Equivalent Radiance (NER) levels for far and near fields respectively. The detector elements have resistances of less than 10,000 ohms in all cases and thus a common ground can be used for the detectors on the focal plane without encountering crosstalk problems.

The second step in fabricating good spatial radiometer arrays is the selection of the starting material. The cutoff wavelength must be higher than the wavelength band. This would require

$x = 0.4$ for the SW band and $x = 0.3$ for the MW band. Material suitable for MW can be used for SW although the reverse is not true. Therefore, we have used MW material almost exclusively. The carrier concentration and uniformity are very important. Photoconductive detectors require extremely pure material. We have recently developed an excellent non-destructive technique using metal-insulator semiconductor structures to determine the carrier concentration. This has permitted us to very accurately limit our selection of starting material to material with carrier concentrations less than $8 \times 10^{14} \text{ cm}^{-3}$ and uniformity over greater than 0.2".

The third major step is the array fabrication. The many processing steps can be critical to the ultimate detector performance. Two important parameters which appear to be affected by processing are $1/f$ noise and photoconductive (trapping) gain. The $1/f$ noise is the most important for spatial radiometer.

The last step is testing which demonstrates that the detectors do meet the sensitivity requirements at low backgrounds. Emphasis is placed on meeting the large or far field element requirements since they are much more difficult than the small or near field elements. Data shown in Section 4 will be for the large elements. The dynamic range can be modeled analytically and will be discussed in more detail in Section 4.

3.0 MECHANICAL LAYOUT AND ELECTRICAL CONNECTIONS

The spatial radiometer focal plane is fabricated from components and subassemblies which are in turn fabricated from more basic components. Figure 1 is a schematic diagram which indicates the different components and the order of assembly. Each component and its integration into the various assemblies will be discussed.

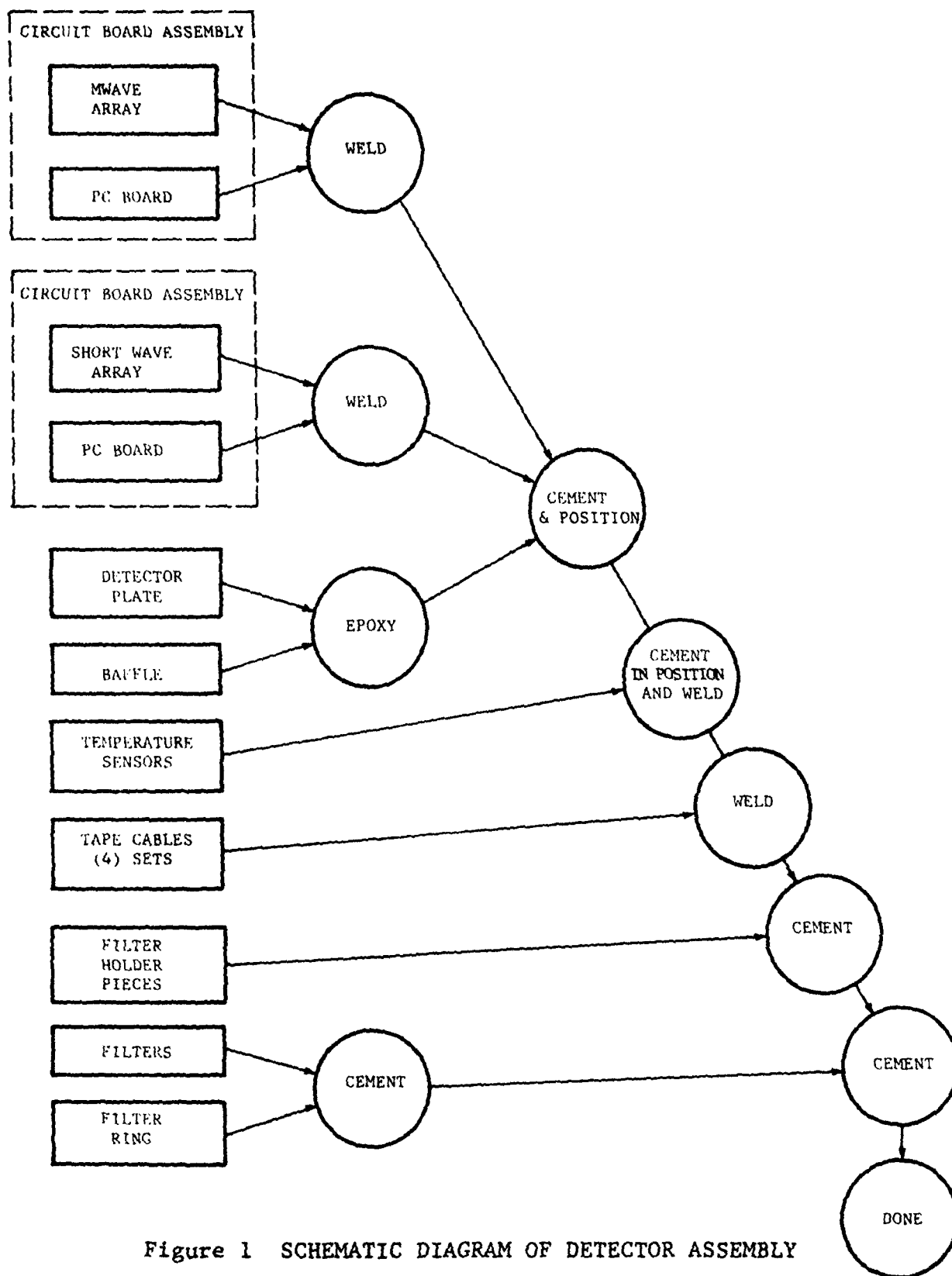


Figure 1 SCHEMATIC DIAGRAM OF DETECTOR ASSEMBLY

3.1 Detector Array Assembly

The Detector Array Assembly (Figure 2) is the heart of the entire module. As indicated in Figure 1, there are two arrays required, a medium wavelength array and a short wavelength array. Dimensionally, however, they are identical and identical procedures are used to fabricate both. The array consists of twenty (HgCdTe) detector elements, which all share a common ground connection which is designated GND. There is a row of large elements designated L1 through L10. The size of each large element is .021" x .021". The spacing between large elements is .001". Parallel to the large elements and at a distance of .010" is a row of small elements designated S1 through S10. The size of these elements is .002" x .0105". The spacing between these elements is also .001".

The elements are mounted on an alumina substrate .010" thick which has been cut to shape. The detector elements themselves are nominally 10 microns thick. The electrodes are formed by evaporating indium onto the module and bonding .001" diameter gold wire onto the indium pads.

3.2 Circuit Board

The circuit board (Figure 3) is a shaped alumina board with etched gold tracks. The board acts as a mechanical carrier for the detector array. Notches on the half circle flats act as evacuation ports for the volume enclosed by the filters in the finished module.

Electrically, the circuit board acts as an interface between the gold wires of the detector array and the larger electrical cables. The circuit board also has provisions for mounting temperature sensors.

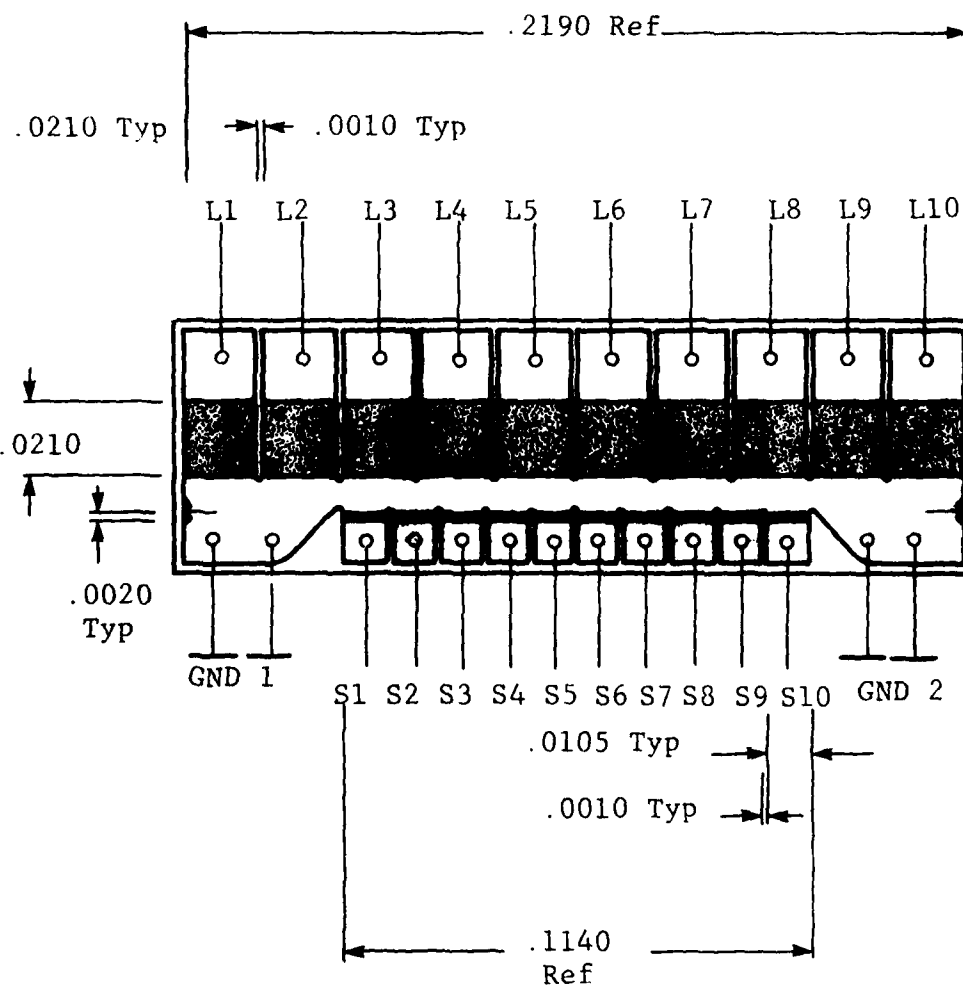


Figure 2 DETECTOR ARRAY ASSEMBLY

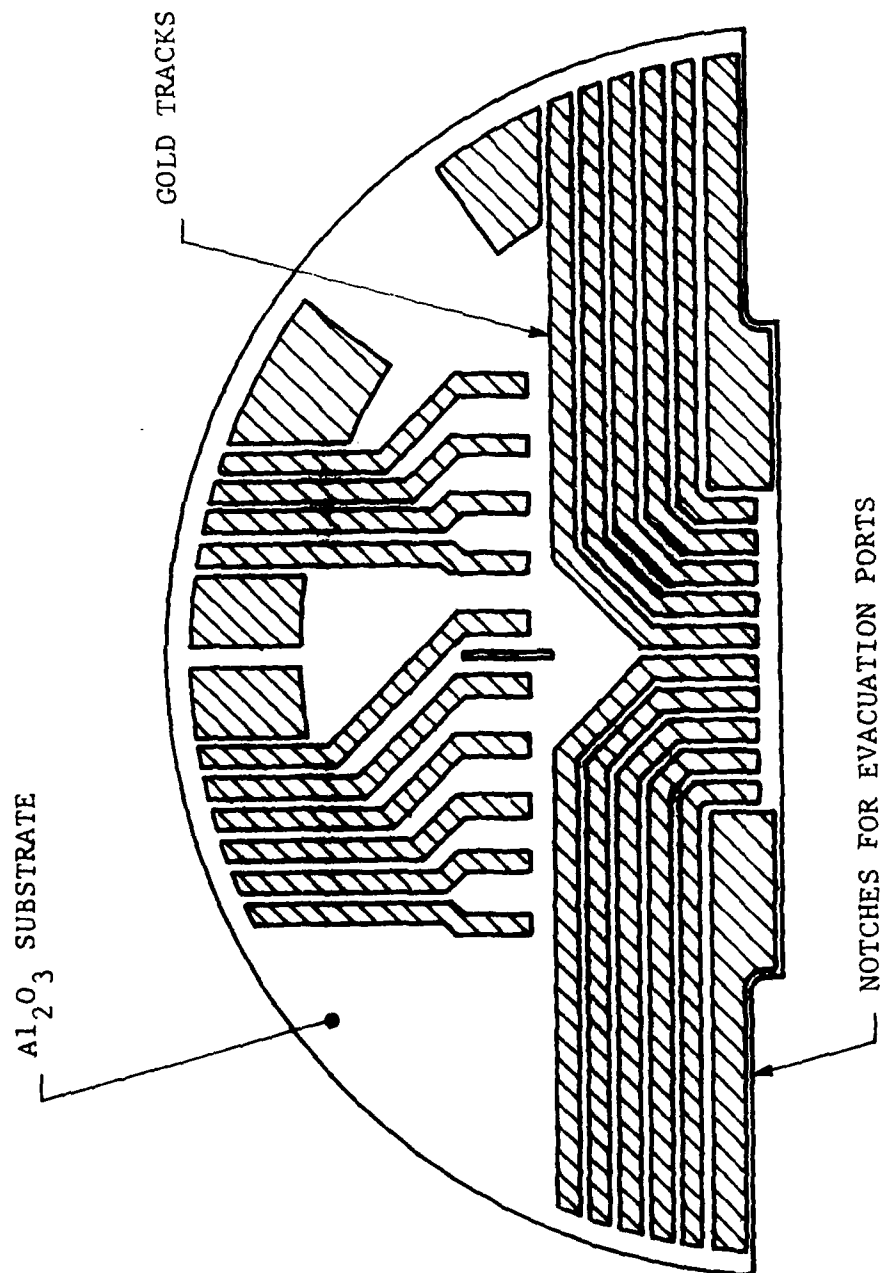


Figure 3 CIRCUIT BOARD

3.3 Circuit Board Assembly

A circuit board assembly (Figure 4) is fabricated by aligning and cementing a detector array to a circuit board using the alignment marks on the board and in the array. The gold wires are then welded to the appropriate gold tracks and trimmed to length. It should be noted that the circuit boards tracks route the small element leads underneath the array. This routing is necessary to permit close spacing of the MW array with the SW array.

3.4 Detector Plate and Baffle

The detector plate (Figures 5 and 6) is the starting point for fabrication of the detector module. It is a 0.5" diameter disk connected to a 3.812" diameter rim by four thin spokes. A baffle plate .020" thick covers the top surface of the detector plate. The circuit board assemblies are mounted on the center disk and cables are mounted along the spokes or spider legs. There is an assymetry in the mounting bolt hole positions which identifies the medium wavelength half of the module from the short wavelength half. The center disk has scribe lines to aid in the alignment procedure.

3.5 Tape Cable Assembly

Four separate identical tape cables route electrical connections from the detectors and temperature sensors to miniature connectors. Each cable (Figure 7) is two layers of copper film conductors insulated by kapton film. One end of the two layer cable is connected to a miniature connector and potted. The other end is trimmed and welded to the circuit board assemblies. The electrical paths in the cables are denoted by T1 through T11 and TG7 and TG2 in Figure 8.

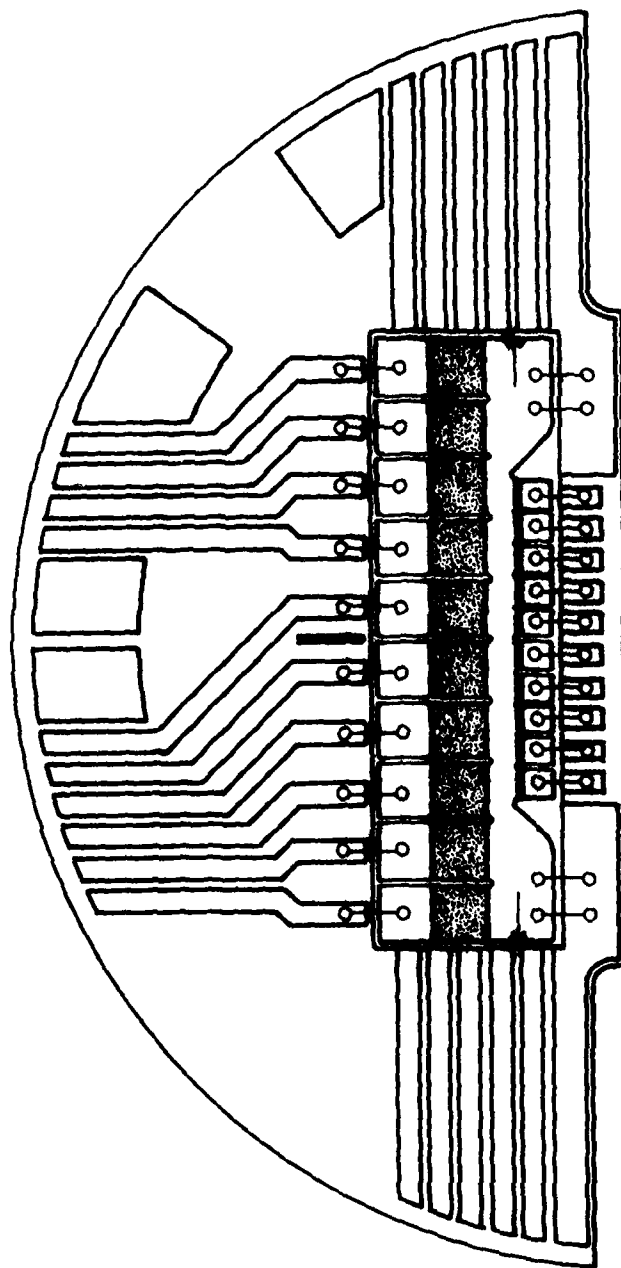


Figure 4 CIRCUIT BOARD ASSEMBLY

10-11

7902-4

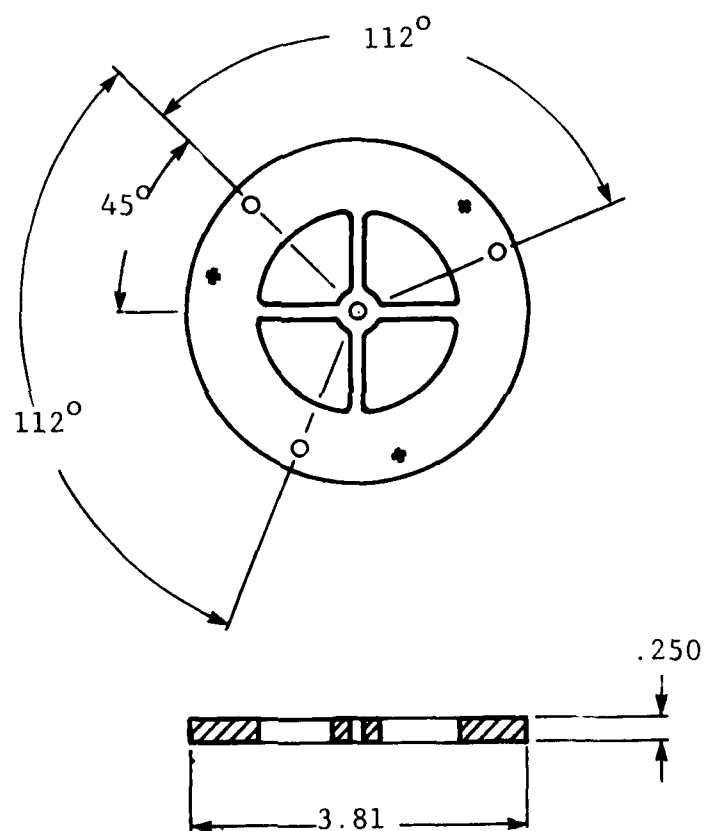


Figure 5 DETECTOR PLATE

10-12

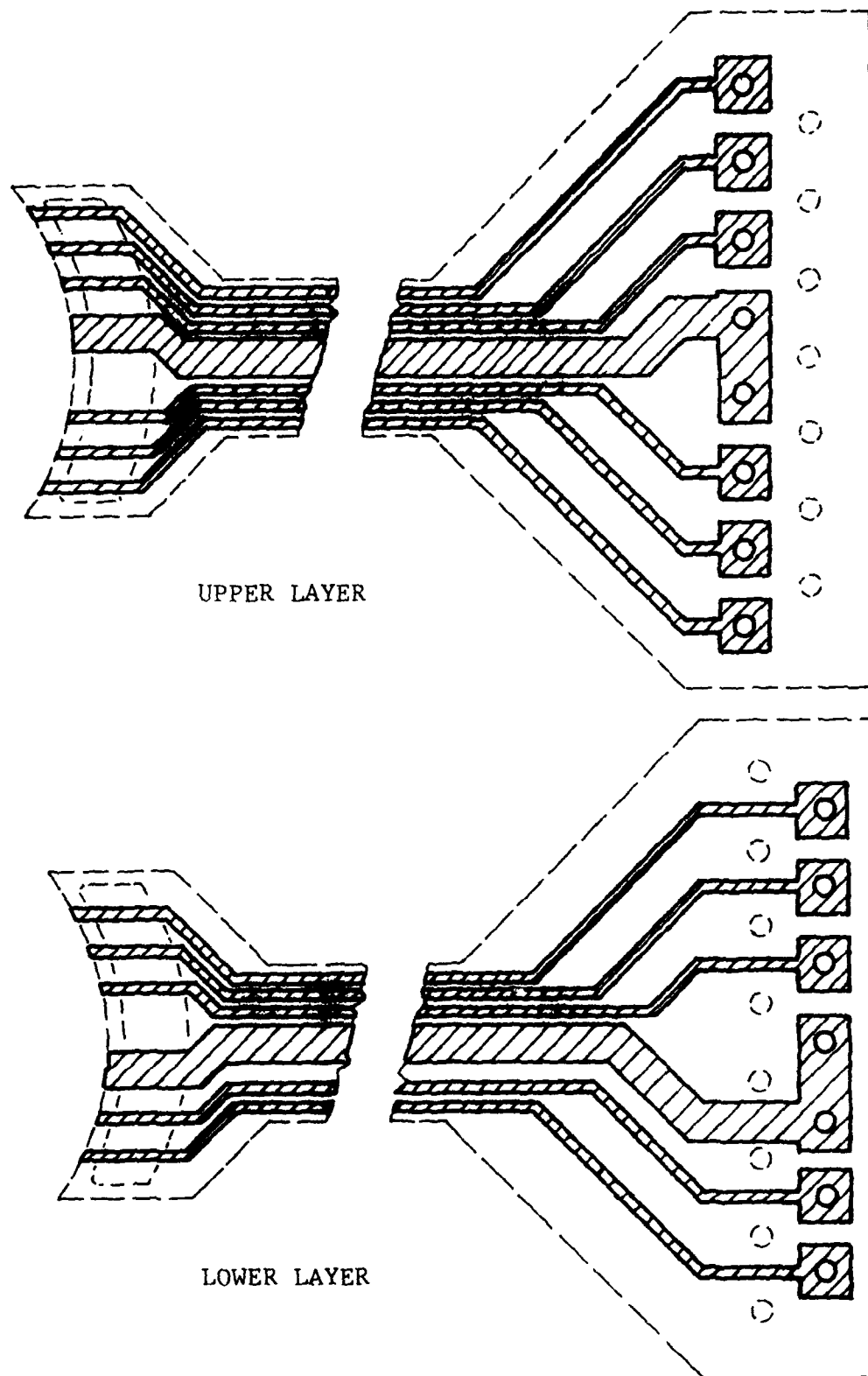


Figure 7 CABLE CONDUCTORS
10-14

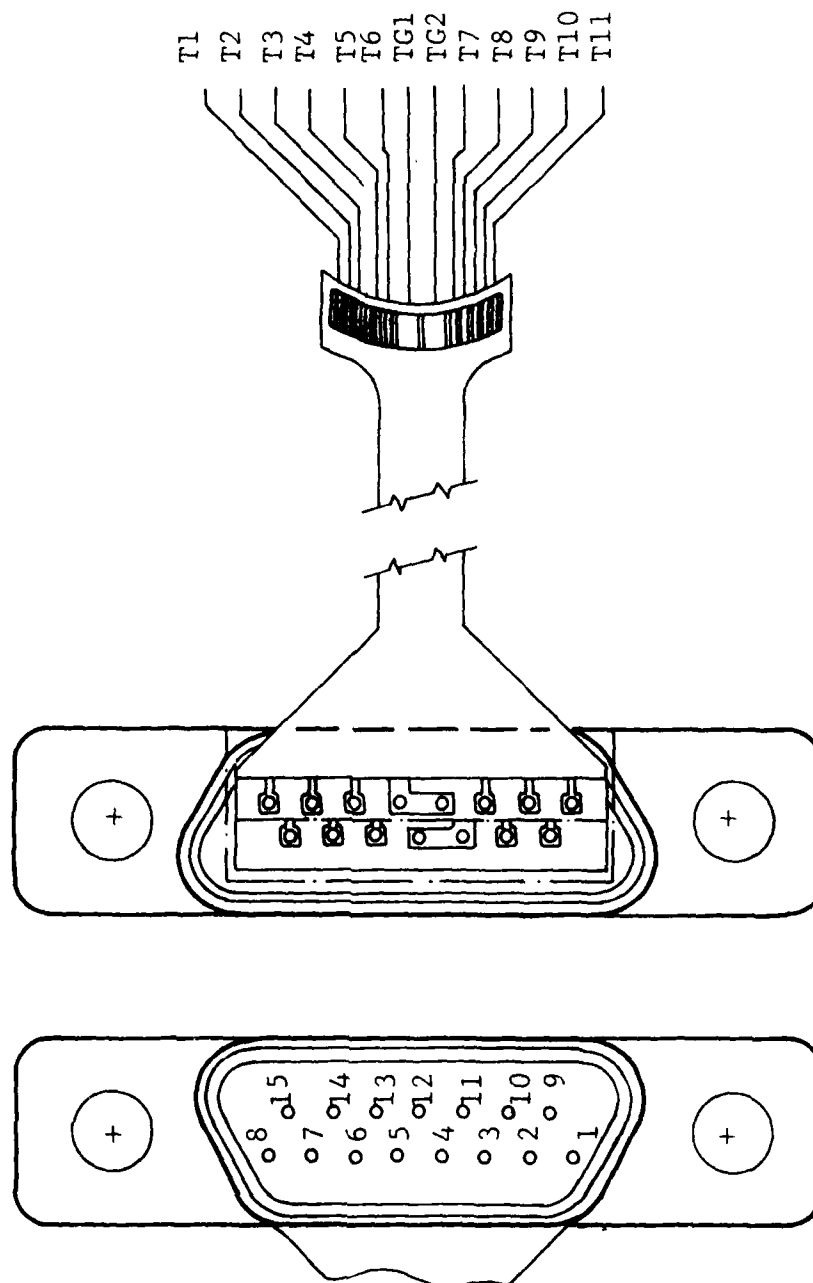


Figure 8 CABLE ASSEMBLY AND NUMBERING DESIGNATION

3.6 Filter Support Structure

The filter support structure consists of filters (Figure 9), a filter holder cap (Figure 10), and a filter mount (Figure 11). The filter set consists of two dimensionally identical interference filters. One is the medium wavelength filter and the other is the short wavelength filter. These filters are cemented into the filter holder cap as shown in Figure 12 to form a filter assembly. The short wavelength filter is identified by an orientation mark scribed on the filter holder cap.

The filter mount is a ceramic ring with a separator bar down the center. The purpose of the filter mount is to hold the filter assembly a fixed distance above the detector elements. This distance is approximately .010". The separator bar optically separates the two arrays of different wavelengths. (See Figure 13.)

3.7 Assembly

Figure 13 is a detail drawing of the center disk of the detector plate with all components in place but with the filter assembly removed. The medium wavelength circuit board assembly is cemented to the disk and aligned according to the scribe marks on the disk surface. After the epoxy has cured, the short wavelength circuit board assembly is cemented in place and aligned with the medium wavelength circuit board assembly. Figure 14 shows the correct orientation of the detector plate bolt holes with respect to the placement of the MW array and the SW array.

After the epoxy has cured the cable ends are trimmed and welded to the printed circuit board patterns. It should be noted that although the cables are mechanically identical, they are not identical in function. After welding, the cables are identified as J1, J2, J3, and J4. Figure 15 is a table identifying each connection of each cable.

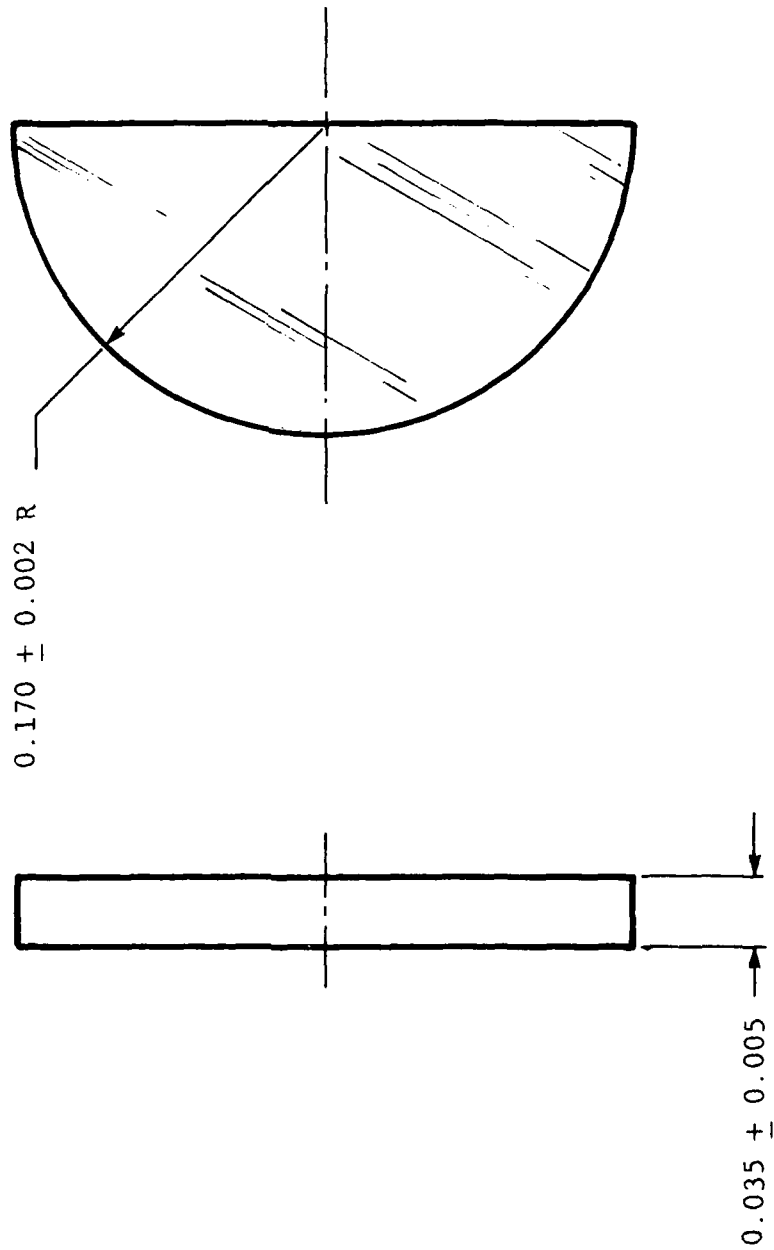


Figure 9 FILTERS

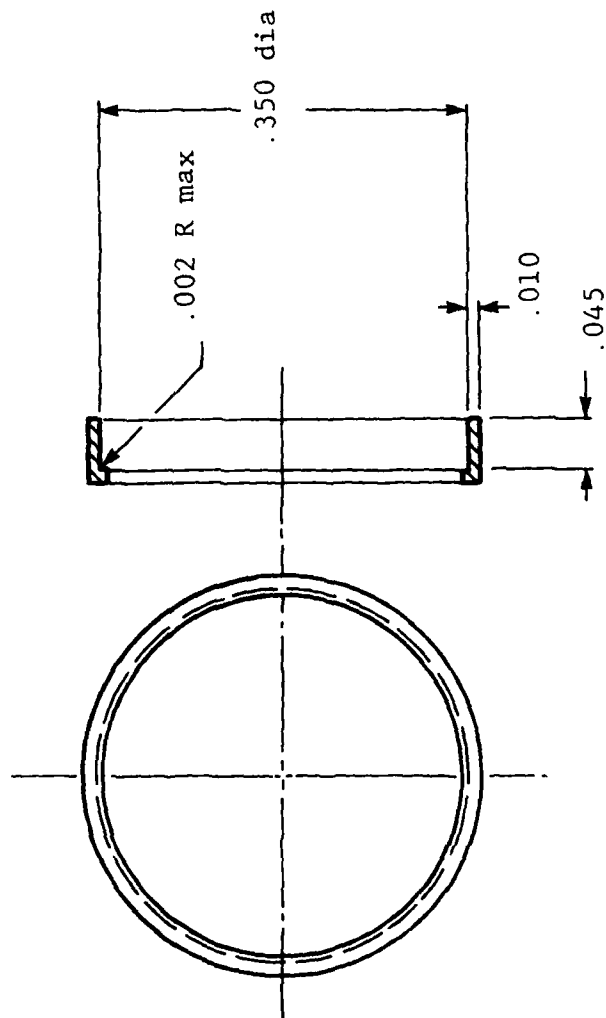


Figure 10 FILTER HOLDER CAP

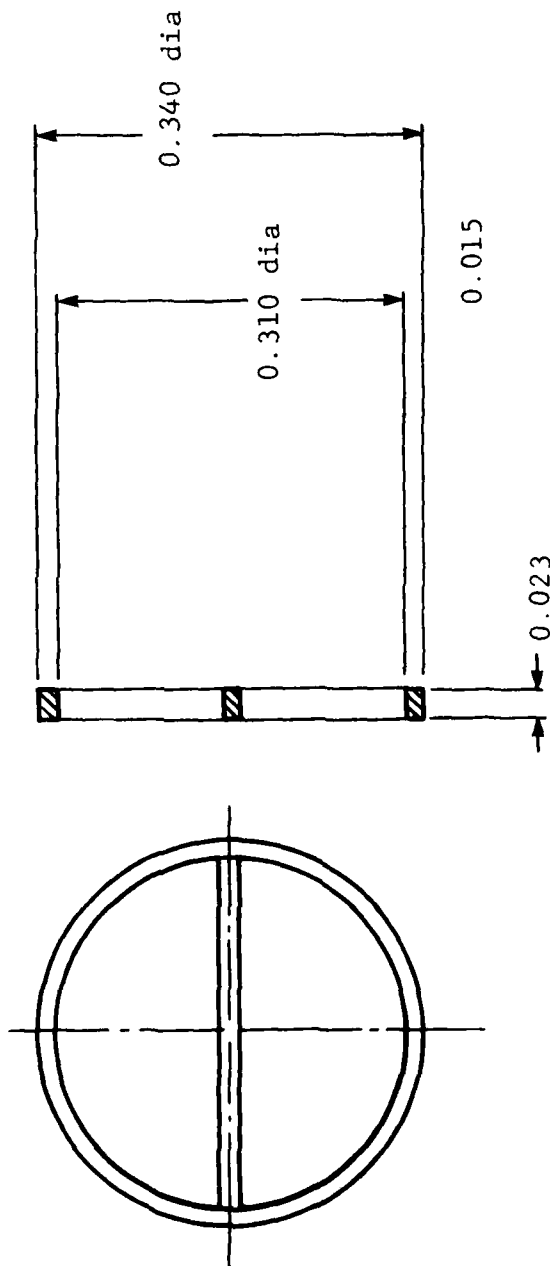


Figure 11 FILTER MOUNT

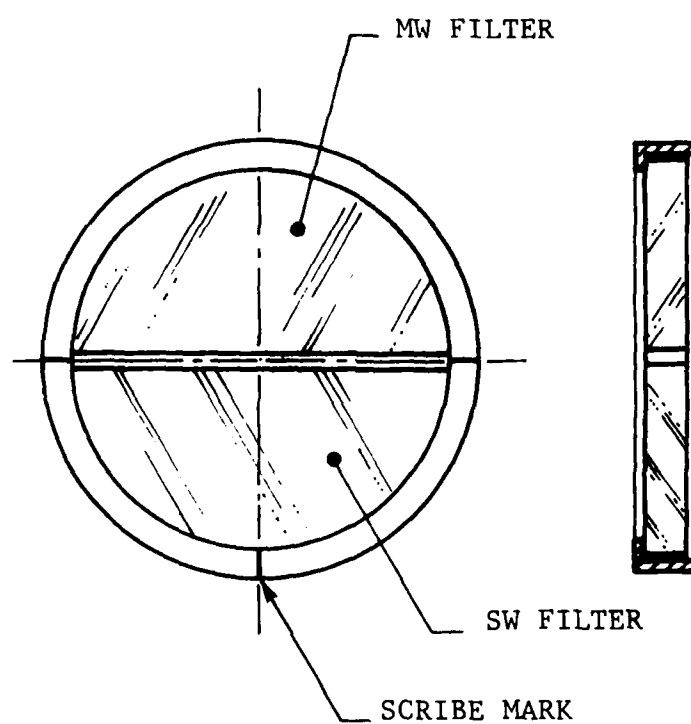


Figure 12 FILTER ASSEMBLY

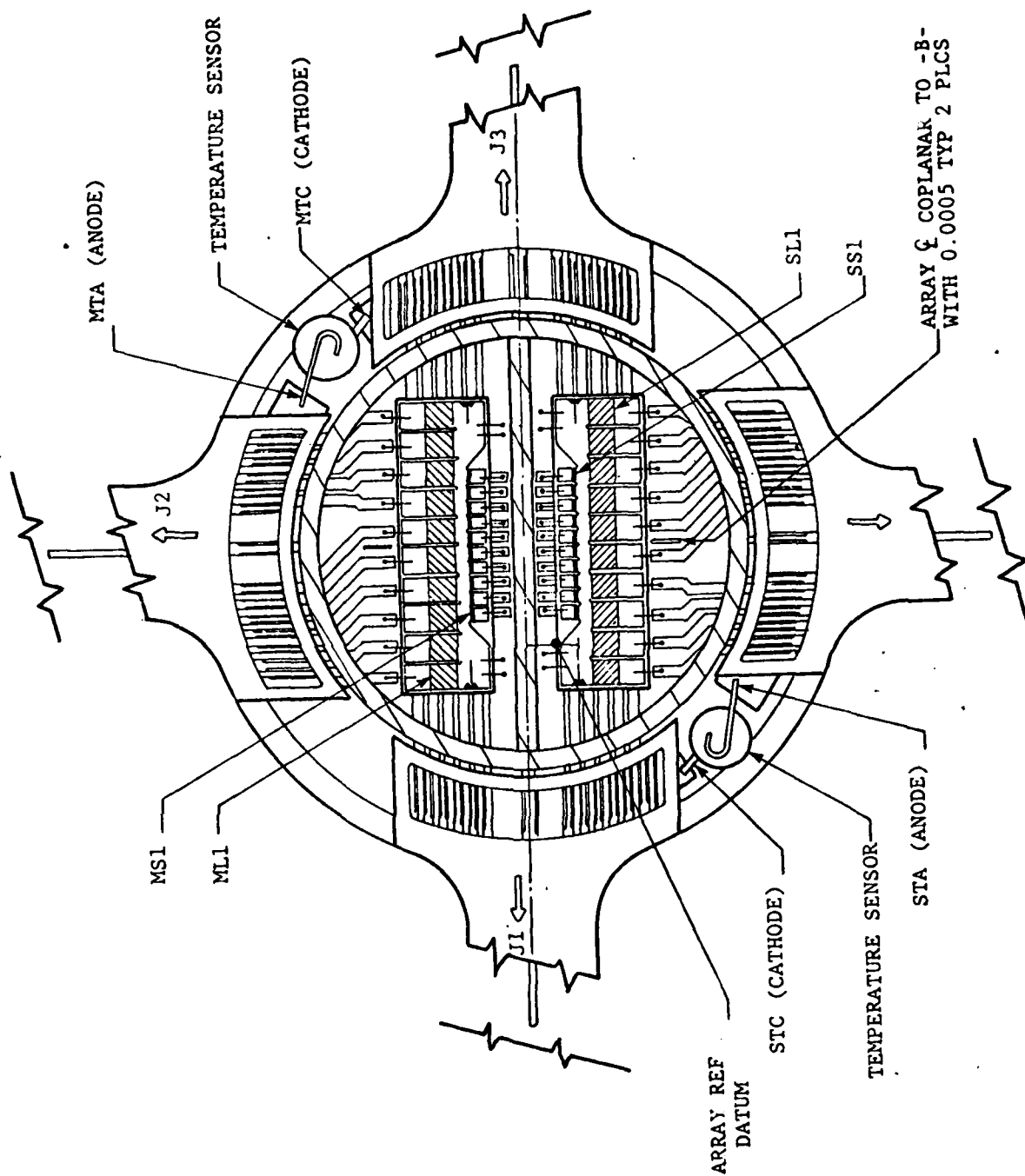


Figure 13 DETECTOR PLATE ASSEMBLY CLOSEUP

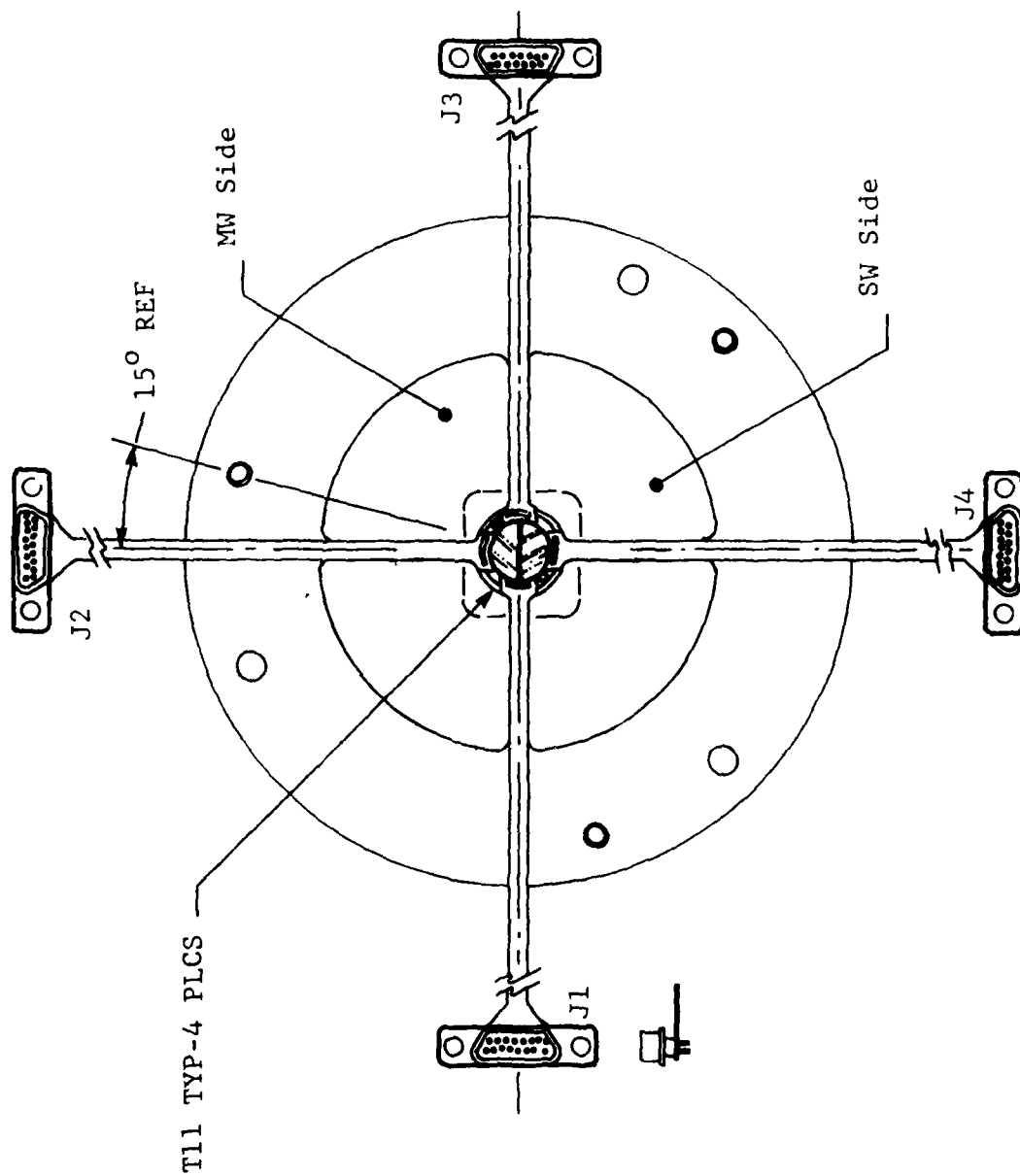


Figure 14 ORIENTATION OF MW AND SW ARRAYS WITH RESPECT TO BOLT HOLE PATTERN IN THE DETECTOR PLATE

THIS PAGE IS BEST QUALITY PRACTICABLE
FROM COPY FURNISHED TO DDC.

| CONNECTOR PIN LIST | | | | | | | | TAPE CABLE LEAD DESIG J1-J4 |
|--------------------|----------|--------|----------|--------|----------|--------|----------|-----------------------------------|
| J1 | | J2 | | J3 | | J4 | | |
| PIN NO | DETECTOR | PIN NO | DETECTOR | PIN NO | DETECTOR | PIN NO | DETECTOR | |
| 1 | MS5 | 1 | LTA | 1 | SS5 | 1 | SLA | T11 |
| 2 | MS3 | 2 | ML9 | 2 | SS3 | 2 | SL9 | T9 |
| 3 | MS1 | 3 | ML7 | 3 | SS1 | 3 | SL7 | T7 |
| 4 | SG2 | 4 | N.U. | 4 | MG2 | 4 | N.U. | T61 |
| 5 | SG2 | 5 | N.U. | 5 | MG2 | 5 | N.U. | T61 |
| 6 | SS9 | 6 | ML5 | 6 | MS9 | 6 | SL5 | T5 |
| 7 | SS7 | 7 | ML3 | 7 | MS7 | 7 | SL3 | T3 |
| 8 | STC | 8 | ML1 | 8 | MTC | 8 | SL1 | T1 |
| 9 | MS4 | 9 | ML10 | 9 | SS4 | 9 | SL10 | T10 |
| 10 | MS2 | 10 | ML8 | 10 | SS2 | 10 | SL8 | T8 |
| 11 | MG1 | 11 | N.U. | 11 | SG1 | 11 | N.U. | T62 |
| 12 | MG1 | 12 | N.U. | 12 | SG1 | 12 | N.U. | T62 |
| 13 | SS10 | 13 | ML6 | 13 | MS10 | 13 | SL6 | T6 |
| 14 | SS8 | 14 | ML4 | 14 | MS8 | 14 | SL4 | T4 |
| 15 | SS6 | 15 | ML2 | 15 | MS6 | 15 | SL2 | T2 |

MS5

Small Element Number 5
Medium Wavelength Array

Figure 15 IDENTIFICATION LIST FOR CONNECTORS

After welding, the cables are cemented to the detector plate-baffle along the length of the spokes. Temperature sensors are cemented in position and their leads connected. Finally, the filter mount ring is cemented in place. At this point, the module may be checked electrically and visually. Just before installation, the filter holder assembly is aligned and cemented in place. This cementing process may be done with a removable epoxy to facilitate subsequent checks.

4.0 TEST DATA

Primary emphasis to date in the test program has been to assure adequate sensitivity (D_{λ}^*) in the large element detectors. This data can be summarized in two graphs since the uniformity across the array is excellent. All measurements have been made at 77K since it is expected the temperature will be stable and be no greater than 78K.

Figure 16 shows the detector elements in a D_{λ}^* vs R_{λ} plot at 77K and 30 Hz. The responsivity, of course, is increased by increasing the bias. The last point on each line represents a bias of 2 volts or 37.5 V/cm on each detector. Previously excess noise (presumably 1/f noise) dominated so that above approximately 5 V/cm the detectivity decreased. With the lower 1/f noise both higher detectivities and higher responsivities are possible simultaneously.

Figure 17 shows the responsivity, detectivity and noise as a function of frequency. This array is optimized for MW operation so even better results are expected in that band. The noise at 30 Hz is $20 \text{ nV/Hz}^{1/2}$ and thus will not be significantly degraded by the amplifier which has a noise level of approximately $6 \text{ nV/Hz}^{1/2}$ at 30 Hz. The responsivity is correspondingly high with $7.5 \times 10^6 \text{ V/watt}$ at 30 Hz and $2.6 \times 10^7 \text{ V/watt}$ at 10 Hz.

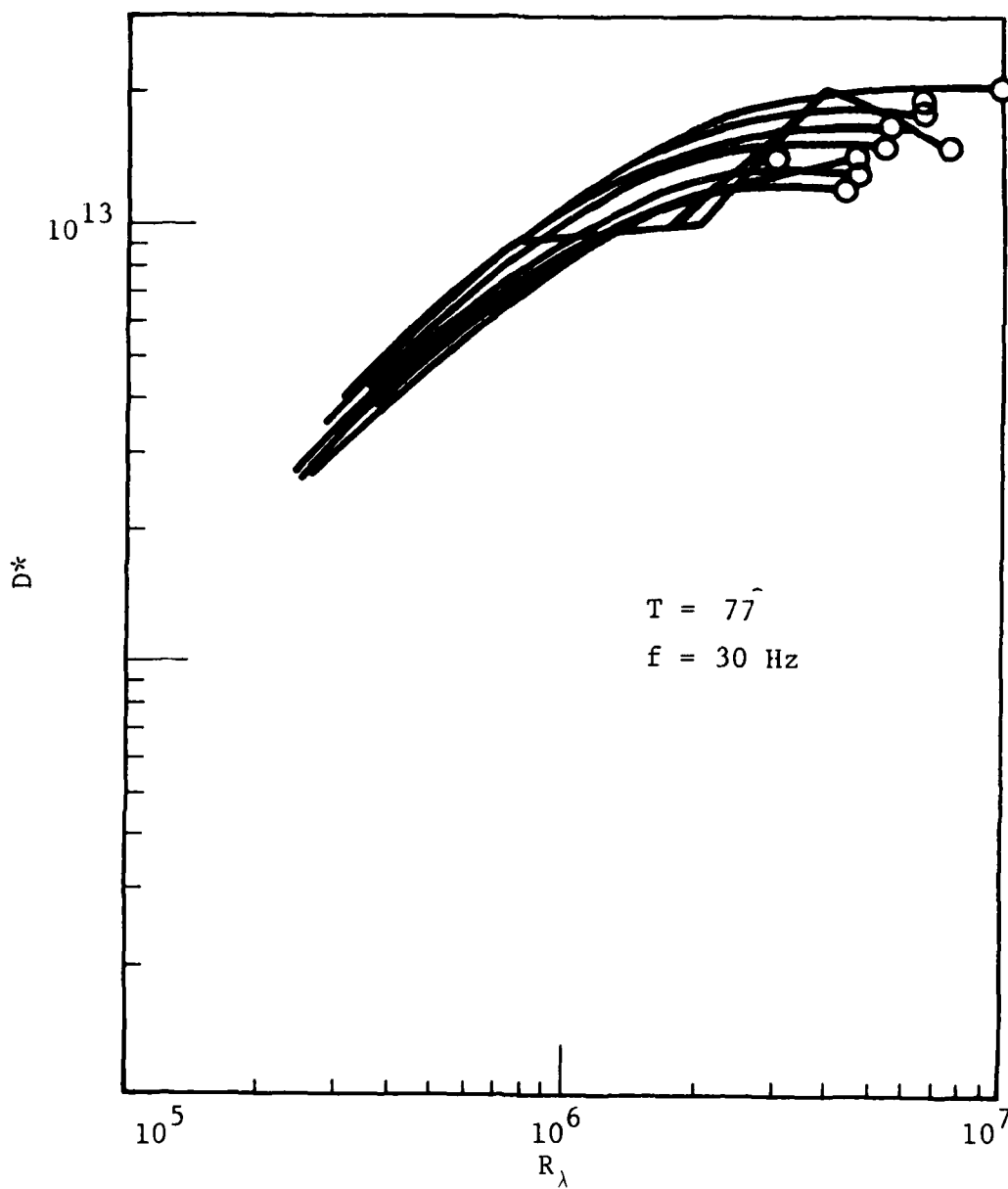
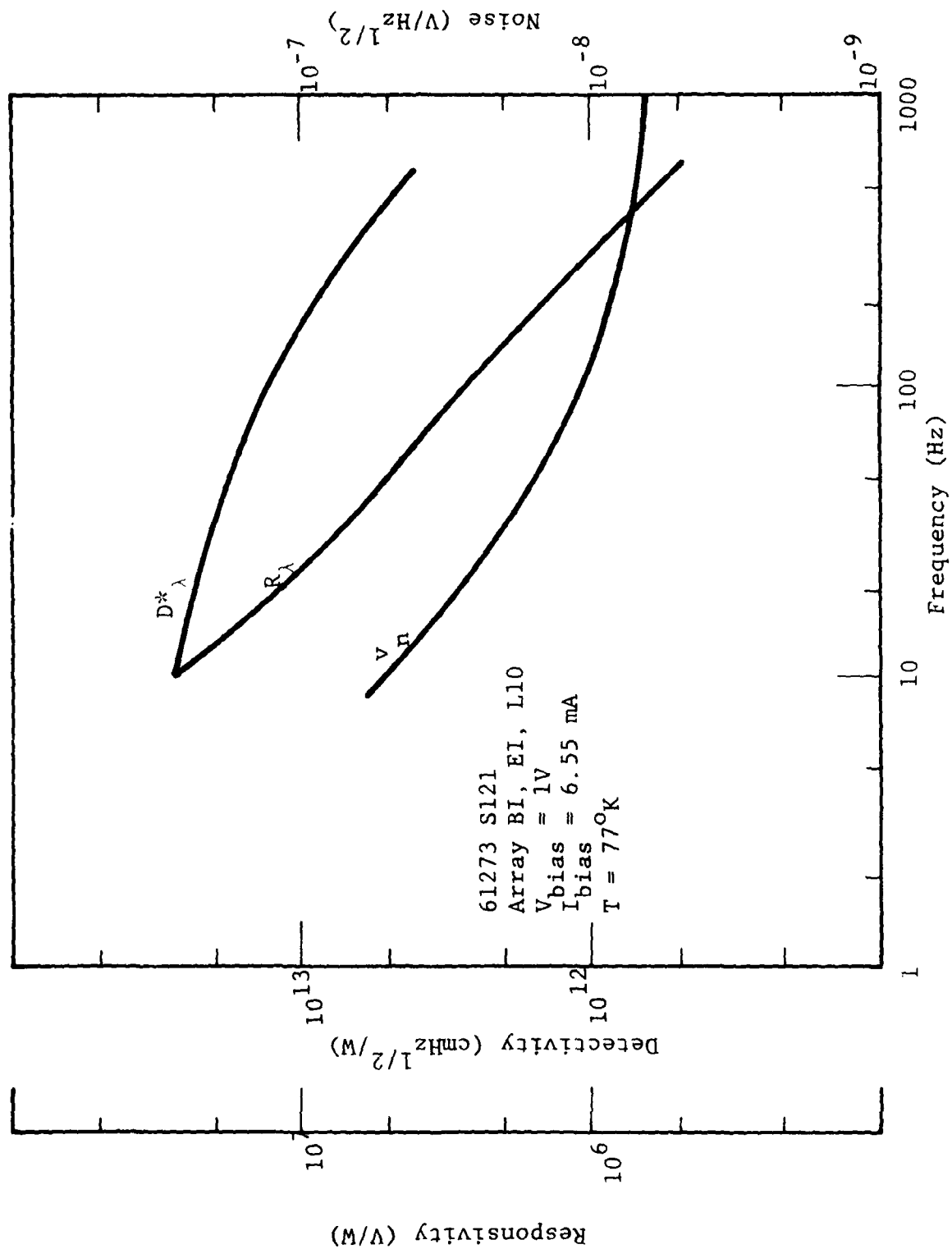


Figure 16 SPATIAL RADIOMETER ARRAY PERFORMANCE AT SW

Figure 17 PERFORMANCE OF TYPICAL LARGE ELEMENT AT $\lambda = SW$

The photoconductive gain for these high sensitivity near infrared (Hg, Cd) Te detectors is enhanced by a trapping gain mechanism which is essential for meeting the high detectivity requirements. The result of the trapping gain is a compression of dynamic range. The responsivity versus flux can be considered analytically by showing both the resistance and lifetime as a function of photon flux. The value for β has been previously measured in near-infrared detectors and is approximately 0.7. This lifetime change dominates the resistance change.

Dynamic range compression can be described analytically as the change in responsivity per unit change in photon flux level. That is, the change in responsivity R_λ which results from a photon flux level change ΔQ is given by the equation:

$$\frac{dR_\lambda}{dQ} \Delta Q = \text{change in } R_\lambda \text{ for an incremental change } \Delta Q$$

For constant current operation, R is expressed by the equation:

$$R_\lambda = \frac{\eta\lambda}{hc} q \frac{\mu e \tau}{R_d^2} I$$

Both resistance, R_d and lifetime τ are functions of photon flux and have the respective functional relations to Q ,

$$R_d = \frac{1}{wdq\mu_e} \left(\frac{1}{n_o + \frac{\eta Q \tau}{d}} \right)$$

$$\tau = AQ$$

After suitable substitution and differentiation of the responsivity equation,

$$\frac{dR_\lambda}{dQ} = -R_\lambda \left(\frac{2\tau\eta(1-\beta)}{dn_o + \eta Q \tau} + \frac{\beta}{Q} \right)$$

The first component is the change due to change of resistance. The second component is the change due to change of lifetime.

SECTION XI

QUALIFICATION TEST

11-1

7902-4

SUMMARY

Vibration qualification testing was done in accordance with AFGL test specification tech data no. 76-4. The test levels are as follows:

Qualification Testing

Small components (less than 5 lbs.)

.15 g^2 /Hz 100-1000 Hz w/6 dB/oct rolloff to 20 Hz and 2000 Hz.

Other components

.10 g^2 /Hz w/spectral distribution as stated above.

Acceptance Testing

All components

.05 g^2 /Hz w/spectral distribution as stated above.

Systems must survive the above levels but must operate .005 g^2 /Hz w/spectral distribution as stated above.

MSMP Sensor Module Systems Acceptance Test Level

.028 g^2 /Hz 100-1000 Hz w/6 dB/oct rolloff to 20 Hz and 2000 Hz.

Test duration in all cases to be 1 minute minimum.

Shock Tests

All components

50 g's, 11 msec half sine.

MSMP Sensor Module System

25 g's, 11 msec half sine.

AD-A081 584

HONEYWELL ELECTRO-OPTICS CENTER LEXINGTON MA
SPATIAL RADIOMETER. VOLUME 1.(U)
MAR 79 R SULLIVAN

F/G 17/5

UNCLASSIFIED

7902-4-VOL-1

AFGL-TR-80-0061-VOL-1

F19628-75-C-0179

NL

3 of 3
of 009600



313

313

313



END

DATE
FORMED
4-80

END

The first vibration and shock test was performed on the dewar/brazement assembly only. Report Number Spatial Radiometer 092676-0017 is included in Volume II of this final report. Portions of the test and test results leading to the successful environmental qualification will be addressed in this section. Page numbers have been changed to conform to this report.

1.0 SCOPE

The Spatial Radiometer Assembly was subjected to random vibration and shock inputs at Acton Environmental Test Lab on 17 August 1976. This report covers the results on the test.

2.0 PURPOSE

The purpose was to qualify the Dewar/Brazement Assembly per the environmental conditions as specified in the AFGL Spec No. 76-4.

3.0 TEST PLAN

The Spatial Radiometer System No. 1 was assembled in the flight configuration with the following exceptions:

- The Focal Plane Assembly was not mounted.
- Flight wiring was not used.
- No electronics were tested.

All other conditions of the flight system were incorporated. M1 and M2 were aligned, flight connectors were used, all baffles and stops mounted and flight scanner were used.

The Focal Plane Assembly and electronics will be qualified at a later date per AFGL Spec No. 76-4. The Focal Plane will be qualified on the Final Acceptance Test of the sensor at the $0.05 \text{ g}^2/\text{Hz}$ level.

The tests were conducted in accordance with AFGL Spec No. 76-4 (see Appendix A) for Qualification Testing.

The test level for random vibration was $0.10 \text{ g}^2/\text{Hz}$ 100-1000 Hz with 6 dB/oct rolloff to 20 Hz and 2000 Hz.

The shock input was 50 g's half sine at 11 milliseconds.

4.0 TEST RESULTS AND CONCLUSIONS

The Spatial Radiometer Assembly was assembled and aligned in the flight configuration with the Flight Scan Mirror Assembly. The dewar was cooled to 77K and the scan mirror was operational. The test fixture was modified from another program for use with the Spatial Radiometer Assembly.

All temperature sensors were monitored through the test. The scan mirror was placed in the scan mode during the random and shock inputs of the test.

Figure 1 shows the 3 axes of vibration and Figure 2 shows the 3 axes of the shock pulse inputs.

The first axis run on random was the Z-axis. During the first 30 seconds, the Scan Mirror Scope Trace stopped. It was decided to continue the tests and evaluate the scan mirror problem after the test was completed.

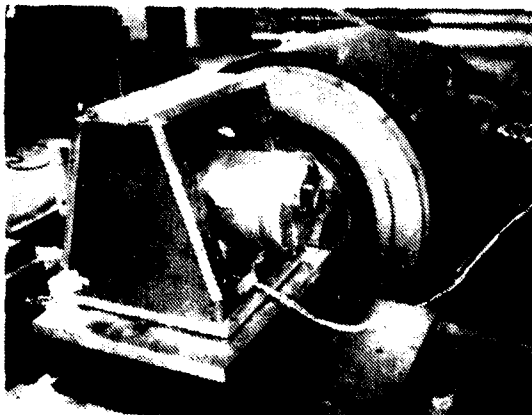
All axes were completed and the assembly was returned to EOC for evaluation.

The Dewar Assembly passed the Qualification Test without any problems. All temperature sensors worked properly and indicated the assembly did not develop any leaks or damage to the vacuum system.

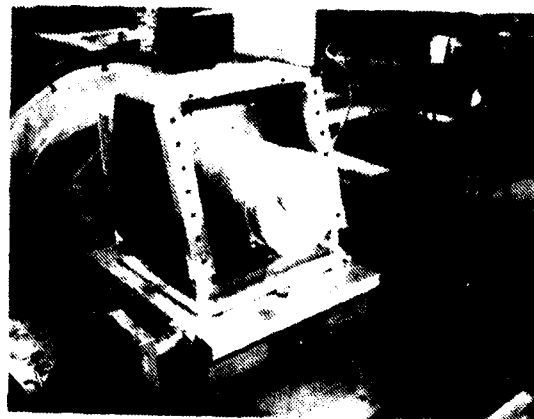
After the system warmed up the brazement was removed. The alignment was rechecked and no change in alignment was noted. All baffles apertures, stops and temperature sensors showed no damage or movement.

The USU Cover Assembly showed internal motion between the Radiation Shield Cold Plate and the Brazement Front Aperture baffle which is normal, however, the aluminum mating surfaces showed wear and small aluminum chips. A corrective action to hard anodize both surfaces to eliminate the wear problem was completed on both parts.

X-AXIS



Y-AXIS



Z-AXIS

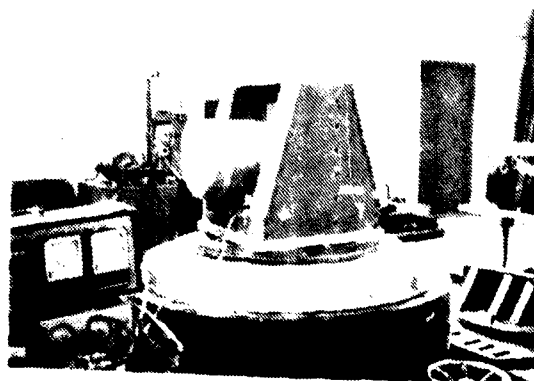
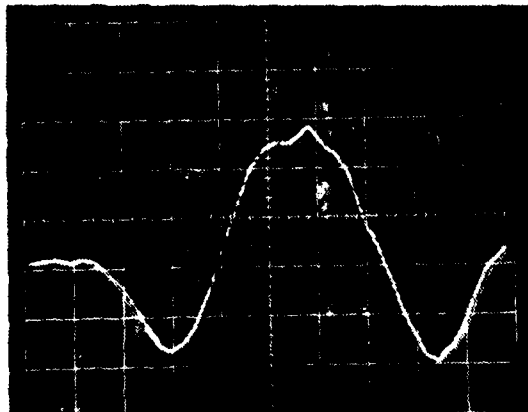


Figure 1 AXES OF VIBRATION

X-AXIS



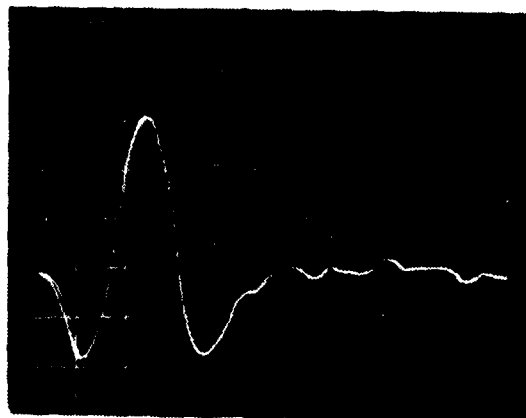
2 ms/cm

Y-AXIS



2 ms/cm

Z-AXIS



10 g's/cm

5 ms/cm

Figure 2 SHOCK PULSES

11-7

7902-4

The Scan Mirror Assembly Alignment to the Brazement and M1 and M2 mirrors remained unchanged. Further evaluation of the scan mirror indicated that the RVDT position indicator had moved on the mirror shaft causing the electronics to change the mirror to the mirror stop position. The RVDT was repositioned properly on the mirror shaft and the scan mode returned to the correct scan alignment. The scan traces were compared before and after the environmental test and no degradation was noted.

The corrective action taken on the scan mirror was to bond the RVDT to the mirror shaft in the correct position. The motor rotor is bonded to the mirror shaft in the present design and did not move during the test, therefore, the light weight RVDT bonded to the shaft is not anticipated as a problem.

The next environmental test of the Spatial Radiometer Assembly will be per AFGL Spec No. 76-4 at the acceptance test levels.

Final acceptance vibration on the sensor and electronics was completed at Acton Test Labs per the AFGL spec tech. data no. 76-4. A copy of the test lab report, no. 12949-2, is included in Volume II of this report. Prior to this test the dewar/brazement and scan mirror assembly was tested at the qual level requirement of the tech. data no. 76-4 spec. on 17 August 1976. A copy of Acton Test Lab Report No. 12617 is included in Volume II. During the August test the scan mirror stopped and a test wiring problem was suspected. However, on 15 March, the scan mirror stopped at the acceptance levels of the test plan and was removed from the system for evaluation.

The problem was due to the rotor moving on the mirror shaft causing an electronic phase shift. To correct the problem, 4 tapped holes were (EDM) Electronic Discharge Machined into the rotor and a new cap was fabricated and pinned to the shaft. The Scan Mirror Assembly was retested at the acceptance qualification level and passed. A copy of the Associated Testing Lab Report No. T-4927-11 is included in Volume II.

SECTION XII

SYSTEM OPERATIONAL PARAMETERS AND TEST RESULTS

SUMMARY

As system number 1 was in process of assembly a performance test plan was generated by EOC to evaluate the sensor parameters as designed. A complete copy of the test plan is included in Volume II of this report, ref. document no. SPAT RAD 020477-0016. This section will cover the results of the system number 1 testing and problems encountered.

1.0 SYSTEM PROBLEMS

During January and February of 1977 evaluation testing continued on system number 1. A major portion of the reporting period was used to evaluate a dewar leak problem. The major concern was the temperature rise in the dewar affecting the electronic operation.

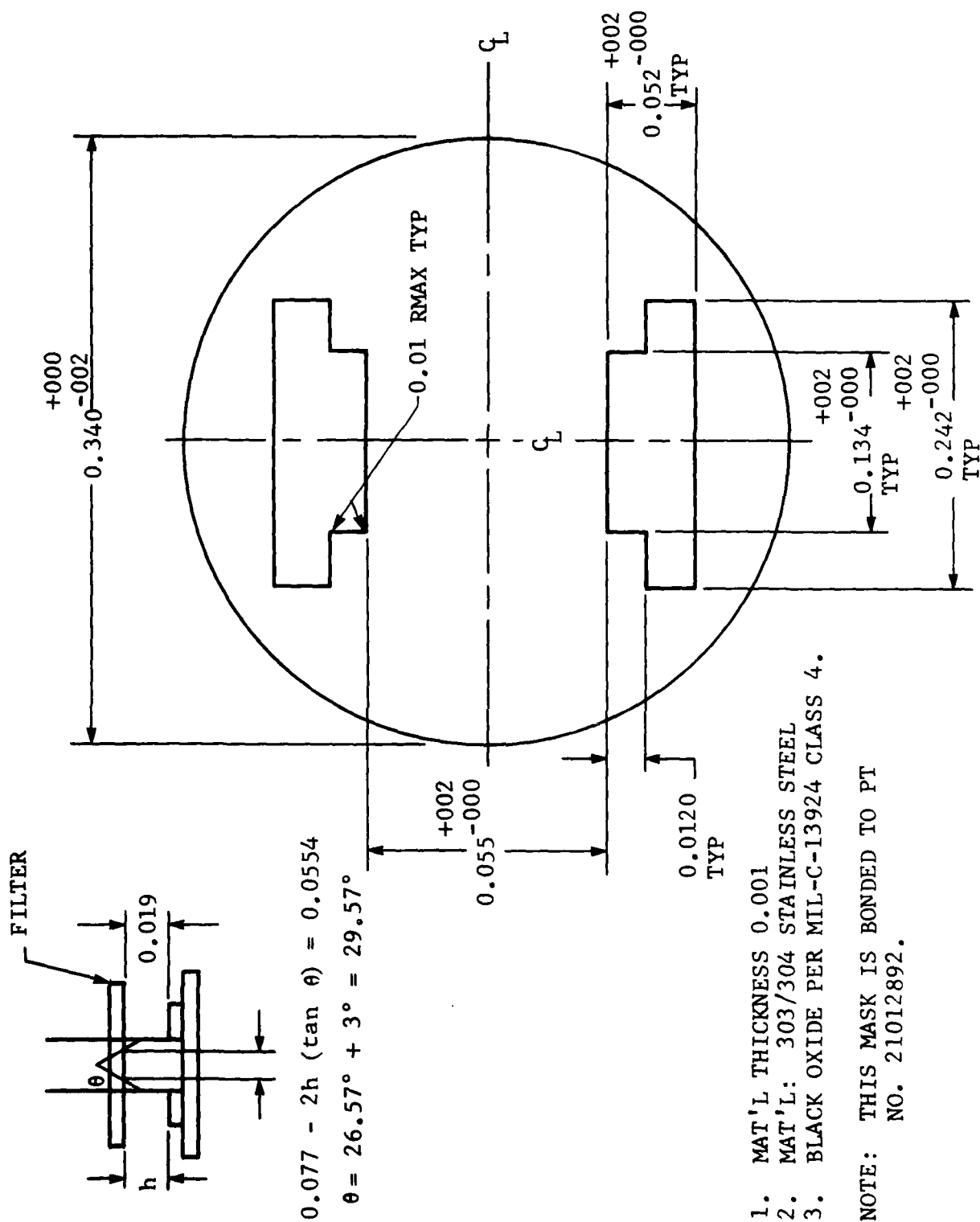
Closer examination of the dewar uncovered porosity in some of the external brazed seams. At that point all external seams on the brazement were grooved and filled with a thin coat of 2850 epoxy. Hold time testing was evaluated after final assembly and proved satisfactory for the launch requirements.

Performance testing continued throughout March and April of 1977. Final acceptance vibration on the sensor was also completed in this time frame. The problems and solution associated with vibration was covered in Section 4.8.

During the May - June, 1977 time frame, calibration/acceptance testing at AFGL was terminated due to a focus and spectral leak in the detector filter assembly. Calibration could not continue until corrective action was taken.

The final results of the retest program indicated that a mask over the detectors appeared to correct the light leak problem and a new shim on the focal plane corrected the focus problem. The detector mask is shown in Figure 1, 1A. Results of the mask are shown in Figures 2 and 3 of a typical detector. However, during further "bonc" calibration testing further anomalous behavior of the SWIR detector channels were noted and calibration tests were stopped.

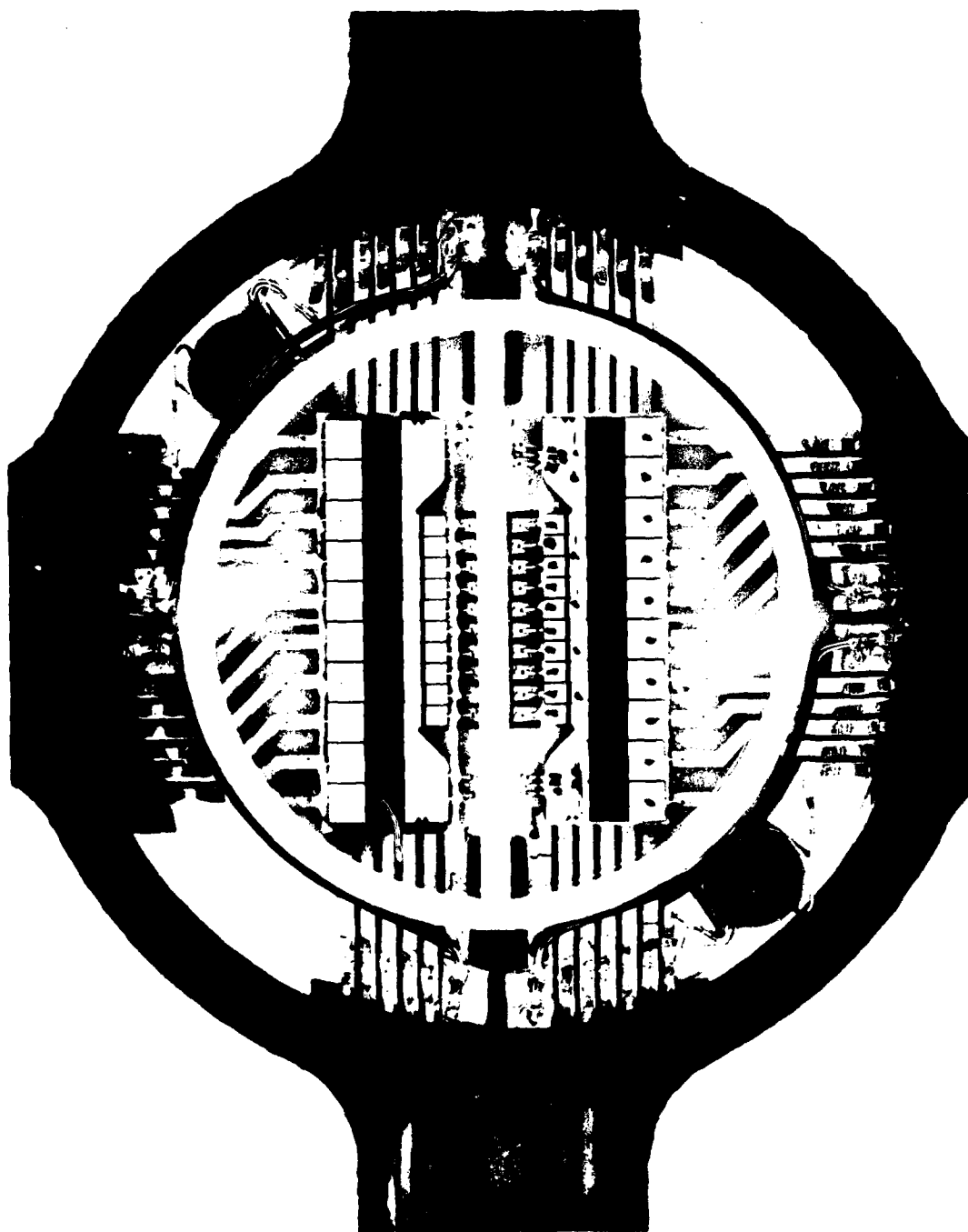
Increased test activities and consulting efforts from EOC systems, detector, thermal and optical groups continued on a daily basis until a solution to the problem was found.



1. MAT'L THICKNESS 0.001
2. MAT'L: 303/304 STAINLESS STEEL
3. BLACK OXIDE PER MIL-C-13924 CLASS 4.

NOTE: THIS MASK IS BONDED TO PT
NO. 21012892.

Figure 1 Detector Mask



01427

Figure 1A Focal Plane

12-5

7902-4

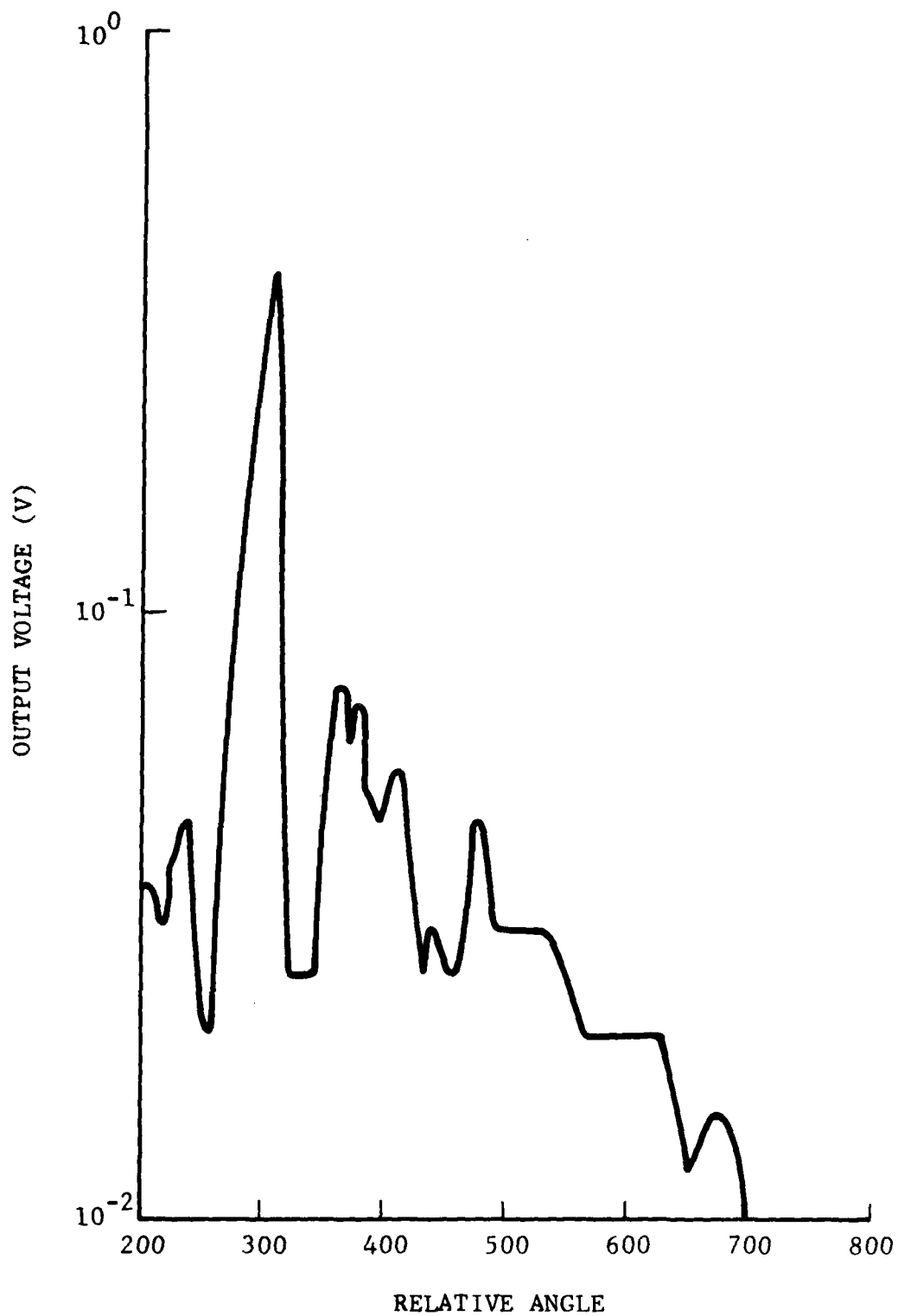


Figure 2 Shortwave Large No. 9 (Azimuth) Before Fix
12-6

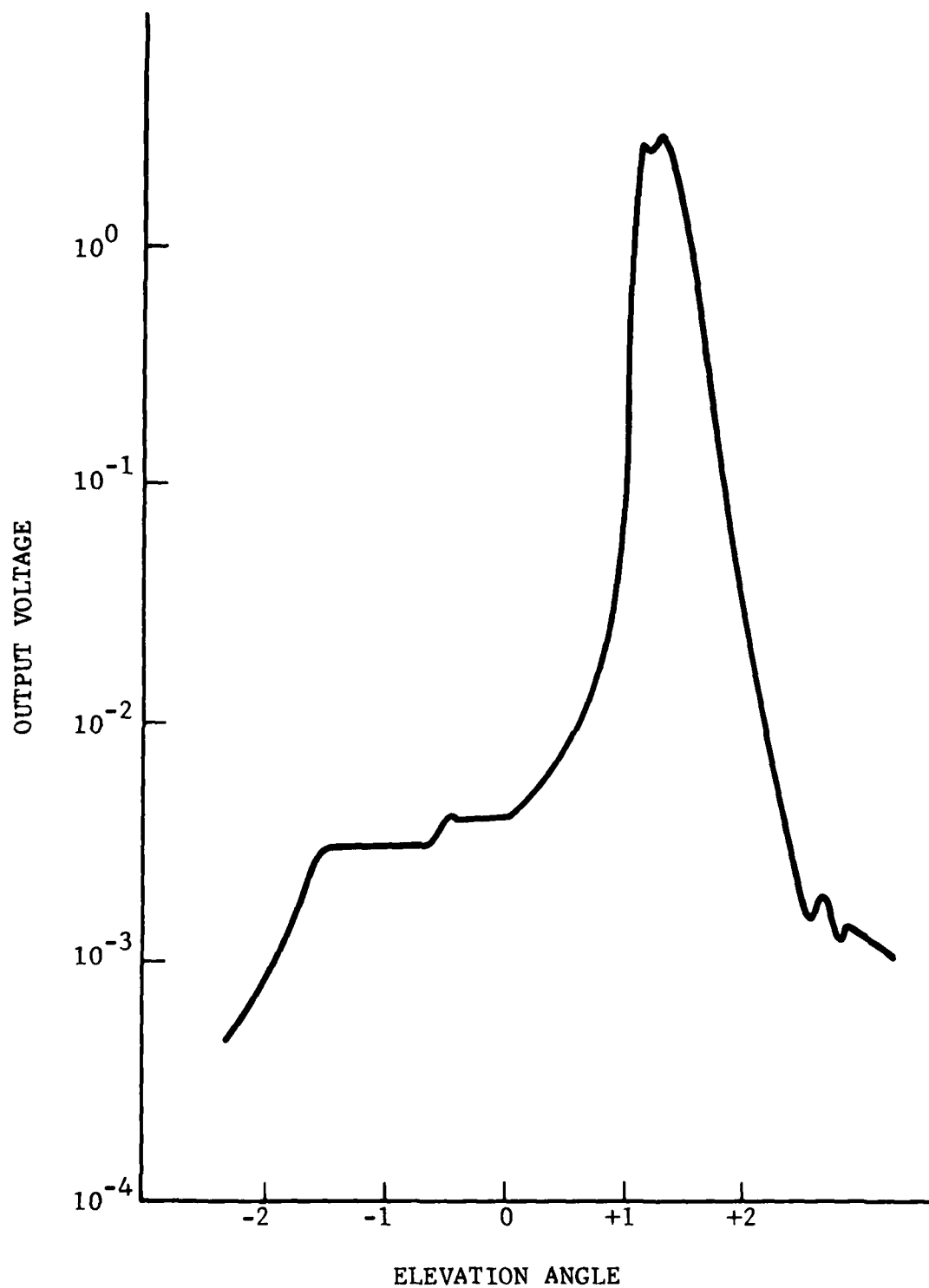


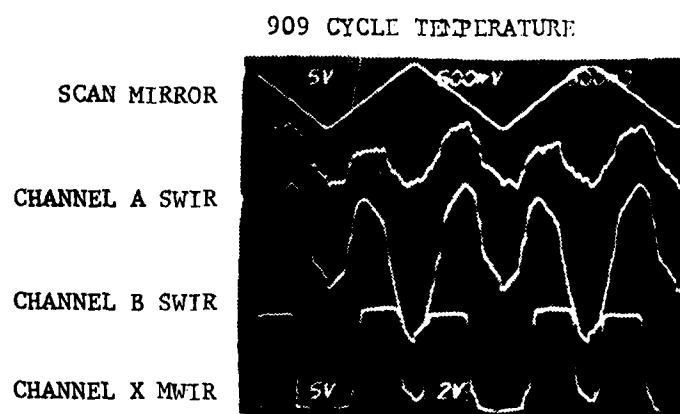
Figure 3 Shortwave Large No. 9 (Elevation) After Fix

12-7

Early in September after many iterative test cycles a solution to the problem was found. The problem appeared to be a filter spectral leak in the 6-8 μ m region and also beyond the 10 μ m region. This leak caused a sinusoidal like response on the SWIR channel detectors.

Our solution to the problem was to install a .125 thick Vycor (No. 7906) glass in the Lyot stop of the sensor. The configuration corrected the SWIR detector behavior, however, it degraded the MWIR detector channels.

The following figures 3.1 and 3.2 will show the comparison of performance levels before and after the installation of the final Vycor material flown in system No. 1.



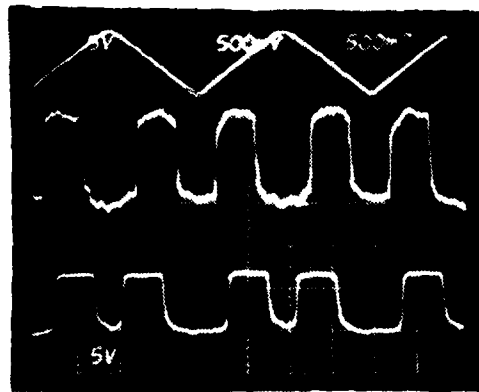
Tests performed with AFGL extended source calibrator
(ref. "Bonc" Tester)

Figure 3.1 Typical Waveform Before Vycore Fix

908 CYCLE TEMPERATURE

CHANNEL B SWIR

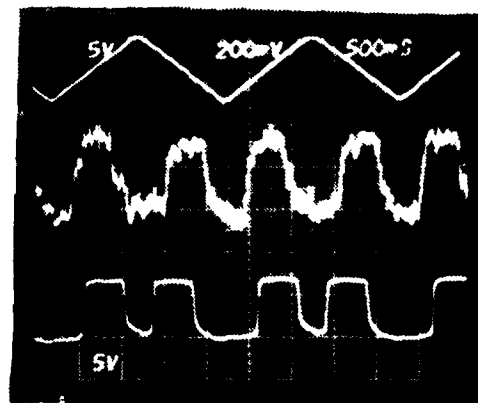
CHANNEL X MWIR



911 CYCLE TEMPERATURE

CHANNEL A SWIR

CHANNEL X MWIR



Tests performed with AFGL extended source calibrator
(ref. "Bonc" Tester)

Figure 3.2 Typical Waveform After Vycore Fix

AFGL agreed to the degraded MWIR channels and final acceptance on the "bonc" and cold collimation tests were completed.

The absolute calibration and system performance data was done at the AFGL test facility. All data was recorded on tape, however, EOC did not reduce the data. It was decided late in the program that AFGL would reduce the "bonc" and cold collimator calibration data.

Measurements were made on a number of channels during the corrective action phase of the program to evaluate the system parameters, however, they are not considered final performance results.

2.0 FIELD MAPPING OF THE DETECTOR

The mapping of the sensor field in space provides instantaneous element position within the sensor scan field. See Figure 4. Mapping of the sensor field requires measurement of the position of detector edge elements both on axis and $\pm 3^\circ$ off axis.

The sensor was mounted on an azimuth rotary table with an angular elevation adjustment mechanism to provide two axis of motion for field mapping (see Figure 5). The sensor was positioned in front of a blackbody collimator source. The collimator was aligned to the sensor boresight by using a transfer mirror to reflect from the external boresight mirror (see Figure 6).

The detector elements to be mapped are shown in Figure 7.

A .012 diameter point source was used at the blackbody and imaged on the focal plane with a spot size of approximately 4.4 mils. The blackbody was adjusted to produce a signal to noise level of at least 10 on each detector being mapped.

The first position to be located was the "0" or on axis position. The rotary table was turned in the \pm direction relative to the collimating beam until the detector edges did not respond. Readings on the rotary table were recorded for both directions. This total azimuth reading was divided in half and this point is the on axis or "0" position.

12-11

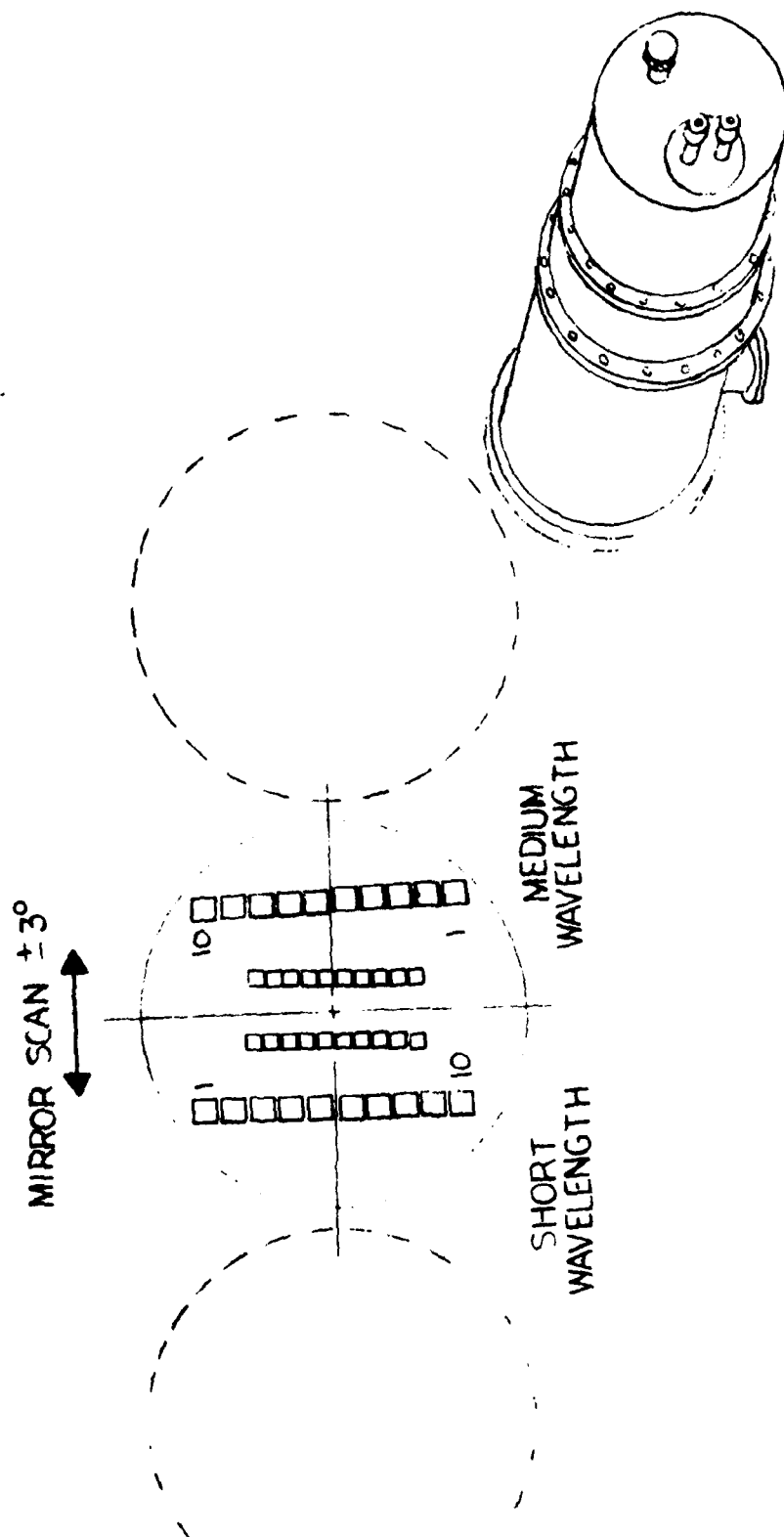


Figure 4 Sensor Field

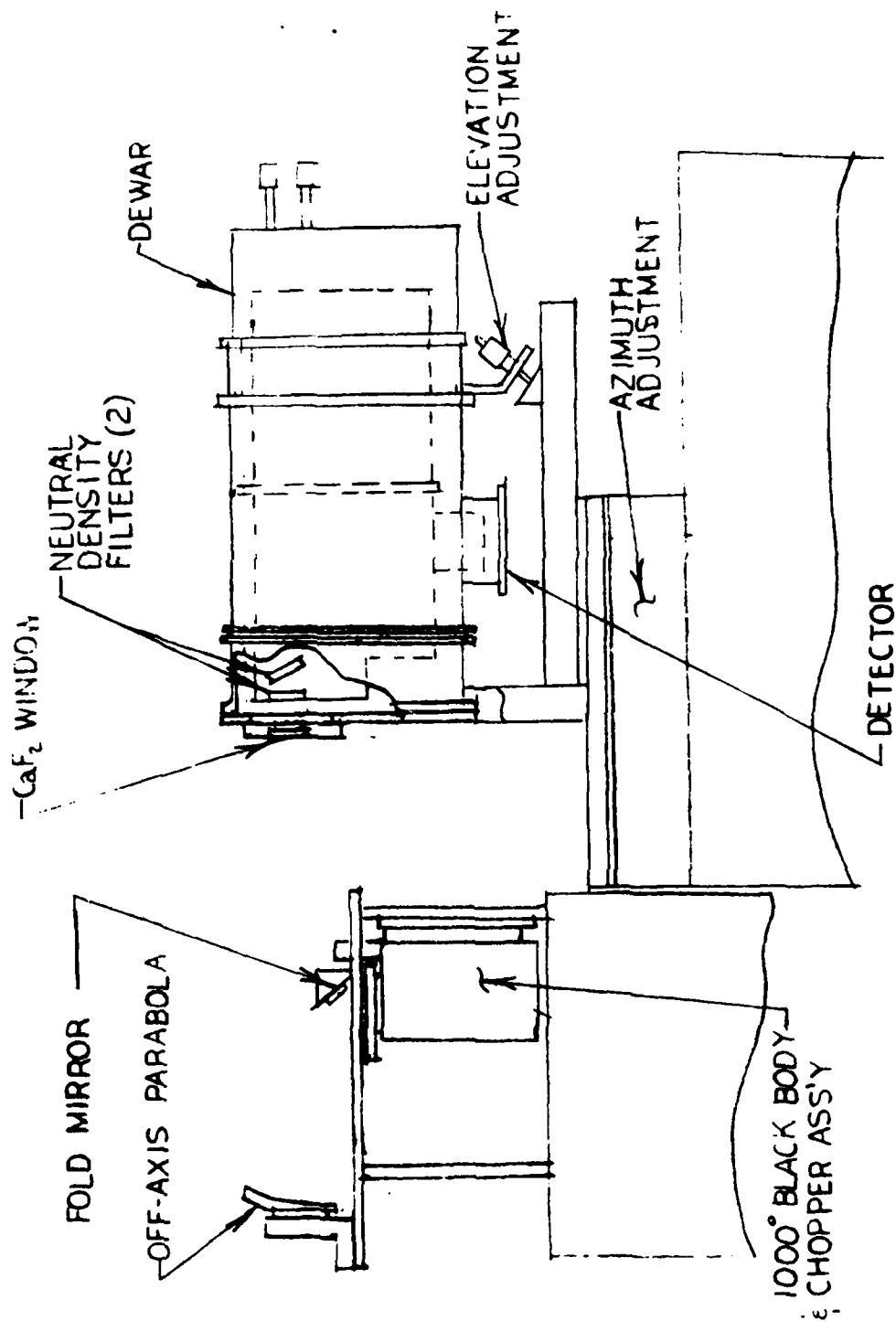


Figure 5 Test Configuration

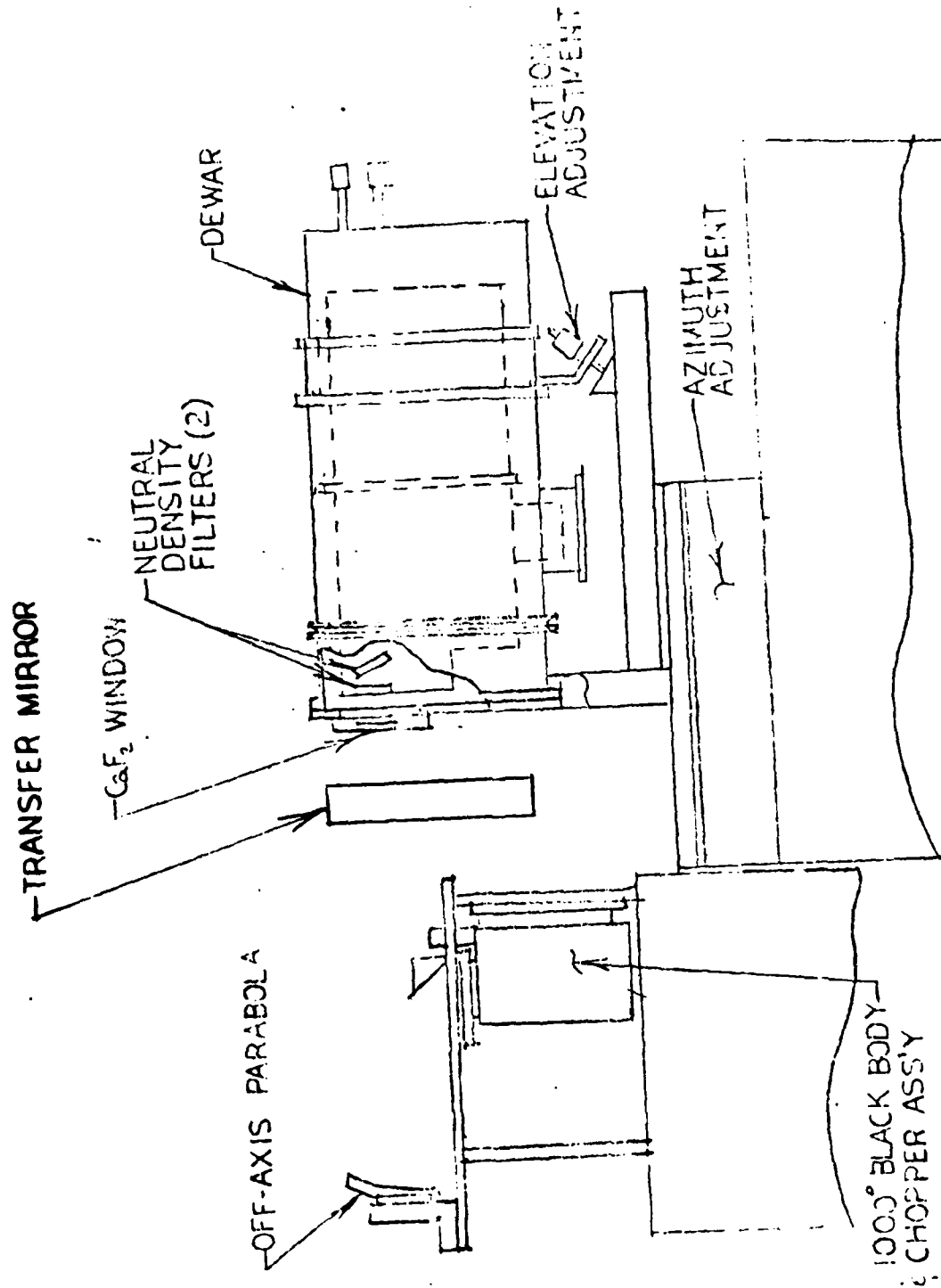


Figure 6 Field Mapping Setup

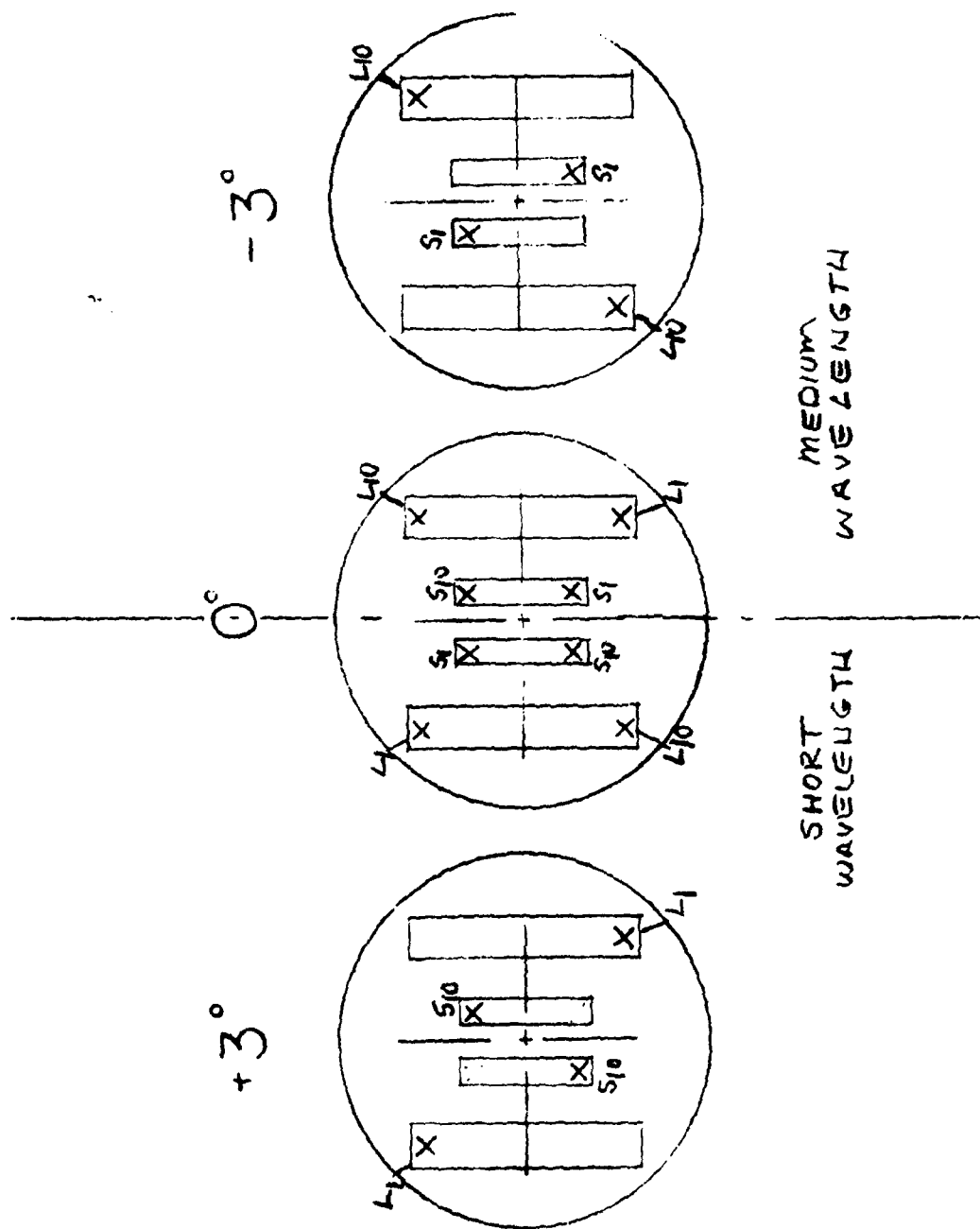


Figure 7 Detector Elements for Field Map

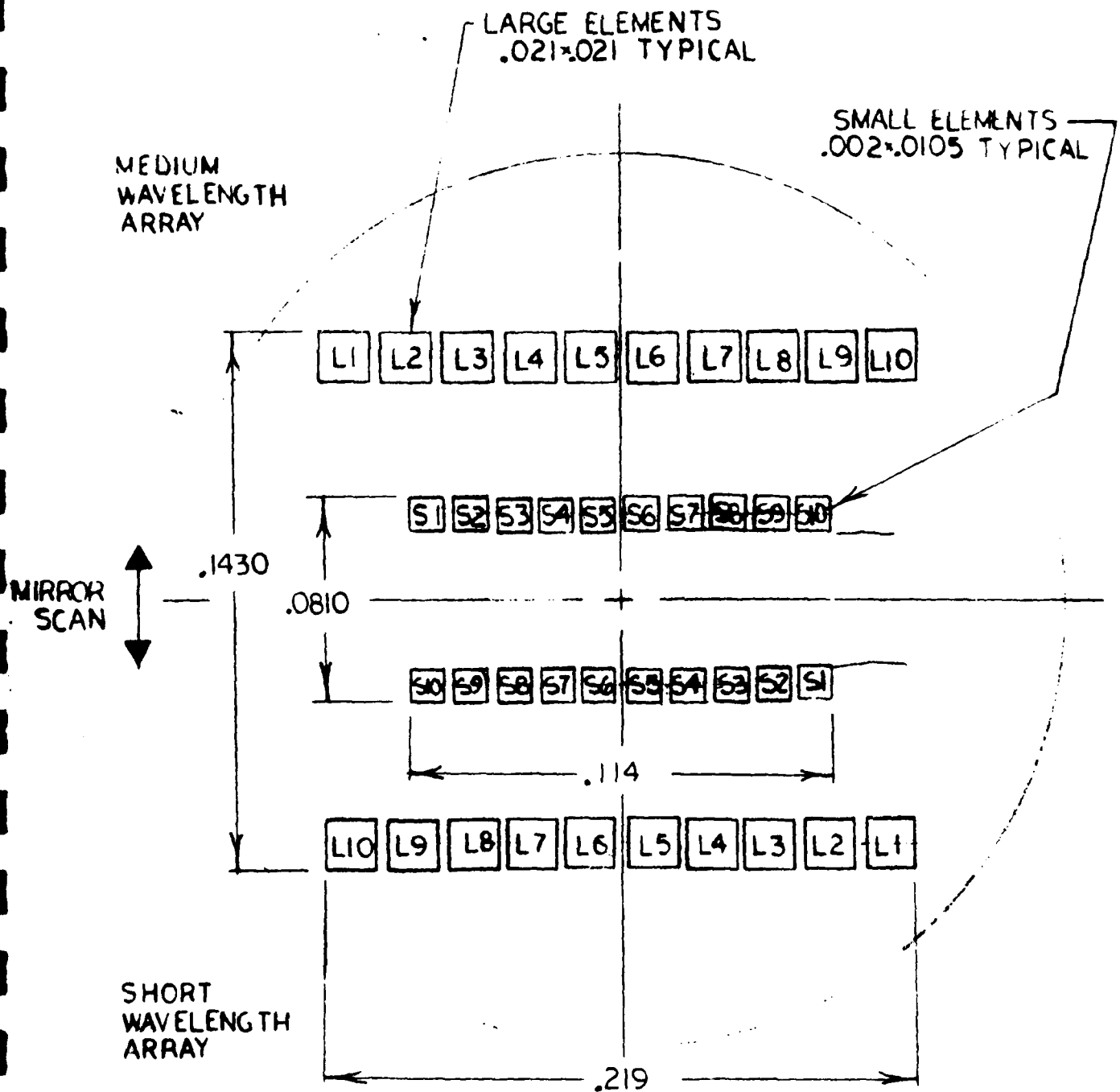


FIGURE 8
DETECTOR ELEMENT LAYOUT

12-16

TABLE 1

SPATIAL RADIOMETER

| | <u>SPEC</u> | <u>DESIGNED</u> | <u>MEASURED</u> |
|------------------|--------------------------------|--------------------------------|------------------------------------|
| FOV | | | |
| NEAR FIELD | 2° x 6° | 2° x 6° | 2.18° x 6.4° |
| FAR FIELD | 4° x 6° | 4° x 6° | 4.2° x 6.4° |
| IFOV | | | |
| NEAR FIELD | .2 x .2 | .2 x .04 | Test Limited |
| FAR FIELD | .4 x .4 | .4 x .4 | .39 x .38 |
| FILTER BAND PASS | | | |
| SHORT | $\lambda \pm .11 \mu\text{m}$ | $\lambda \pm .11 \mu\text{m}$ | $\lambda + .11$ $\lambda - .09$ |
| MEDIUM | $\lambda \pm .125 \mu\text{m}$ | $\lambda \pm .125 \mu\text{m}$ | Data Being Shipped |

The zero elevation position signal drop was located by finding the midpoint between detectors L5 and L6 on both the medium and narrow fields of both colors. The elevation micrometer adjustment readings were recorded in the same manner as the azimuth readings. Reference Figure 8 for detector element layout. A minimum of two scans in each direction elevation and azimuth was made to provide the field map of the detector.

The data system (CRT and computer) can also selectively and repetitively display detector data for any pre-selected mirror position relative to the external azimuth and elevation adjustments.

Table 1 summarizes the results of the EOC field mapping procedure.

3.0 DYNAMIC BORESIGHT ALIGNMENT

The sensor was mounted on an azimuth rotary table equipped with an angular elevation adjustment mechanism to provide two axes of motion. The sensor was positioned in front of a blackbody collimator source, and aligned to the boresight. The sensor was under vacuum and cold. Since the center of motion of the scan mirror is the center of the scan field, selected detector positions were measured relative to this in order to determine actual boresight. Alignment is accomplished by positioning the blackbody source image on individual detector elements by adjusting and recording the sensor angle in azimuth and elevation.

From the electrical "0" position of the sensor, a transfer mirror was used to align and lap into position an external boresight reference mirror. The original requirement for boresight was to be within $1/4^\circ$. Our alignment method was $\leq .016^\circ$ for the sensor boresight.

SECTION XIII
PRE-FLIGHT/FLIGHT DATA

SUMMARY

This section outlines the pre-flight and flight information received from system No. 1.

1.0 Introduction

The sensor was launched from the White Sands Missile Range on November 19, 1977. There was a four week period before the launch during which integration and payload tests were performed. Various problems did arise during this period but were resolved prior to launch. The sensor performed as required during the flight and a large amount of flight engineering data was obtained. The following sections detail both the pre-flight flight performance results.

Pre-flight Operation

The EOC launch support activities for the MSMP program encompassed a 3-1/2 manweek effort of two EOC personnel.

The preliminary tasks included unpacking and test equipment check-out in the vehicle assembly building area. System and functional tests were supported through the pre-launch test cycle.

The EOC launch check-out procedure was coordinated with the MSMP countdown sequence.

Functional checks during the pre-launch sequence countdown tests were recorded on tape using both the spatial radiometer sensor system, and the AFM recording system. Data during the

The following procedure was used for the

See page 2.

LAUNCH CHECK-OUT PROCEDURE

| | |
|--------------|--|
| T-33 hrs. | Start Pump Warm Sensor |
| T-9 hrs. | Start LN ₂ Transfer |
| T-7 hrs. | Finish LH ₂ Transfer |
| T-6 hrs. | Turn on Power to System |
| | Begin Functional Checks & record on tape |
| T-5 hrs. | Voltages and Temps. - Compare to Calibrations (CRT) |
| T-4-3/4 hrs. | Mirror - Scan Pattern and Amplitude (AGE) |
| T-4-1/2 hrs. | Data Channel Stabilization - Nominal Values (CRT) |
| T-4-1/4 hrs. | Data Channel Noise - Nominal Values (CRT) |
| T-4-1/4 hrs. | Data Channel Noise - Nominal Values (Record) |
| T-4 | Run Hot Wire Calibration (Record) |
| | Playback data and compare to calibrations |
| T-3 hrs. | Run blackbody Calibrations (Record) |
| | Playback data and compare to calibrations |
| T-2-1/2 | Top off LN ₂ in dewar and connect Tavco Vent Valve |
| T-2-1/4 | Remove Pump from Sensor and Cap off pumping port |
| T-2.0 | Remove VPS and Cryogenic Equip. from Launch Area. |
| T-1-1/2 hrs. | Voltages and Temp - Compare to Calibrations (CRT) |
| T-1-1/4 hrs. | Data Channel Stabilization - Compare to Nominal Values (CRT) |
| T-1 hr. | Voltages and Temp. - Compare to calibrations (CRT) |
| T-45 min. | Scan Mirror - Scan Pattern & Amplitude (AGE) |
| T-40 min. | Hot Wire Calibration (Record) |
| | Playback data and compare to calibrations. |

| | |
|------------|--|
| T-15 min. | Computer in record and display mode. |
| T-10 min. | Blackbody operation - (CRT) |
| T-8 min. | Scan Mirror - Scan pattern and Amplitude (AGE) |
| T-5 min. | Temp.- Compare to calibrations (CRT) |
| T-4 min. | Data Channel Stabilization - Compare to Nominal Values. (CRT) |
| T-3 mins. | Internal Power Switch over Begin Continuous Record |
| T-110 sec. | Scan mirror - Scan Pattern & Amplitude (AGE) |
| T-90 secs. | Hot wire calibration - Monitor MWIR thru AGE |
| T-60 secs. | Voltages and Temp - CRT |
| T-30 secs. | Data Channel Stabilization - Nominal Values AGE. |

3.0 Functional Performance - Flight

The entire flight data stream was recorded both on the Honeywell and AFGL recorders. The Honeywell data showed more sync losses because of receiver and decommutator problems, but the data was good enough to evaluate the sensor performance. There was no evidence of sensor performance degradation during the entire flight. All mechanisms, sources and detectors operated as required. The following sections give more detailed data for the various functional units.

3.1 Detectors

All detector channels except the number 6 small element in the short wave array (which was damaged during previous assembly tests) were operational during the entire flight as evidenced by the data obtained from the use of the in-flight tungsten source calibrator. (Results are presented in Section 3.3).

One of the primary concerns was whether the channels would maintain d.c. offset during the launch and boost phase. The offsets did drift slightly ($< 50\text{mv}$) during the launch phase but settled back to their nominal levels before the actual data taking period. Even this slight change was not significant enough to degrade sensor performance.

3.2 Scanning Mirror

The scanning mirror performed as required during the launch and flight. The scanning waveform is a trapezoid as shown in Figure 3.0. This waveform is the actual analog output of the angular transducer mounted on the shaft of the scanning mirror. This analog voltage is sampled at a 250 sample/sec rate and encoded into the PCM bit stream. A least squares fit algorithm was applied to the sampled data. A straight line equation was generated from the algorithm which was a plot of mirror position versus time. The actual time co-ordinates were

3.0 Functional Performance - Flight

The entire flight data stream was recorded both on the Honeywell and AFGL recorders. The Honeywell data showed more sync losses because of receiver and decommutator problems, but the data was good enough to evaluate the sensor performance. There was no evidence of sensor performance degradation during the entire flight. All mechanisms, sources and detectors operated as required. The following sections give more detailed data for the various functional units.

3.1 Detectors

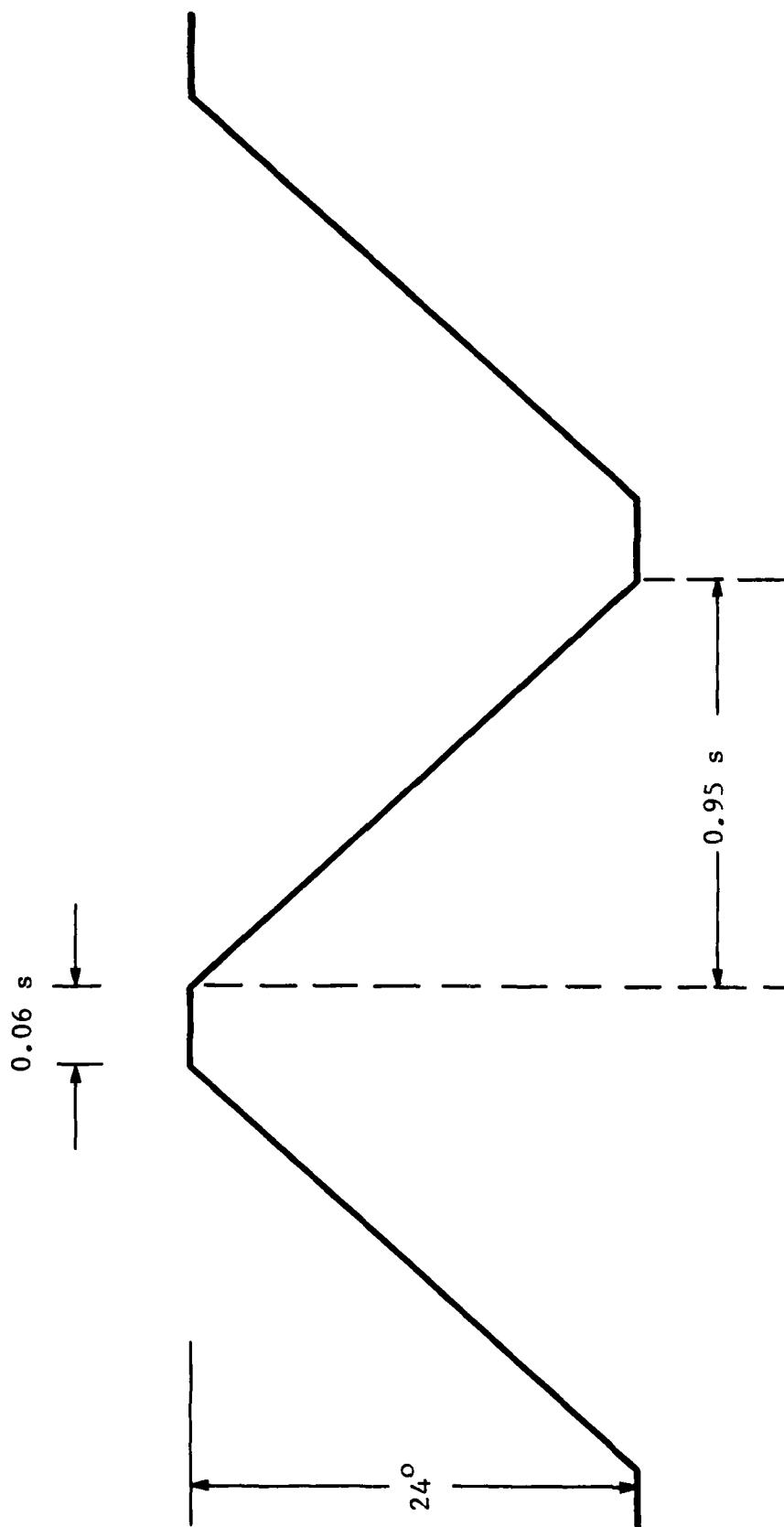
All detector channels except the number 6 small element in the short wave array (which was damaged during previous assembly tests) were operational during the entire flight as evidenced by the data obtained from the use of the in-flight tungsten source calibrator. (Results are presented in Section 3.3).

One of the primary concerns was whether the channels would maintain d.c. offset during the launch and boost phase. The offsets did drift slightly ($< 50\text{mv}$) during the launch phase but settled back to their nominal levels before the actual data taking period. Even this slight change was not significant enough to degrade sensor performance.

3.2 Scanning Mirror

The scanning mirror performed as required during the launch and flight. The scanning waveform is a trapezoid as shown in Figure 3.0. This waveform is the actual analog output of the angular transducer mounted on the shaft of the scanning mirror. This analog voltage is sampled at a 250 sample/sec rate and encoded into the PCM bit stream. A least squares fit algorithm was applied to the sampled data. A straight line equation was generated from the algorithm which was a plot of mirror position versus time. The actual time co-ordinates were

7902-4



13-7

Figure 3.0 Scan Mirror Waveform

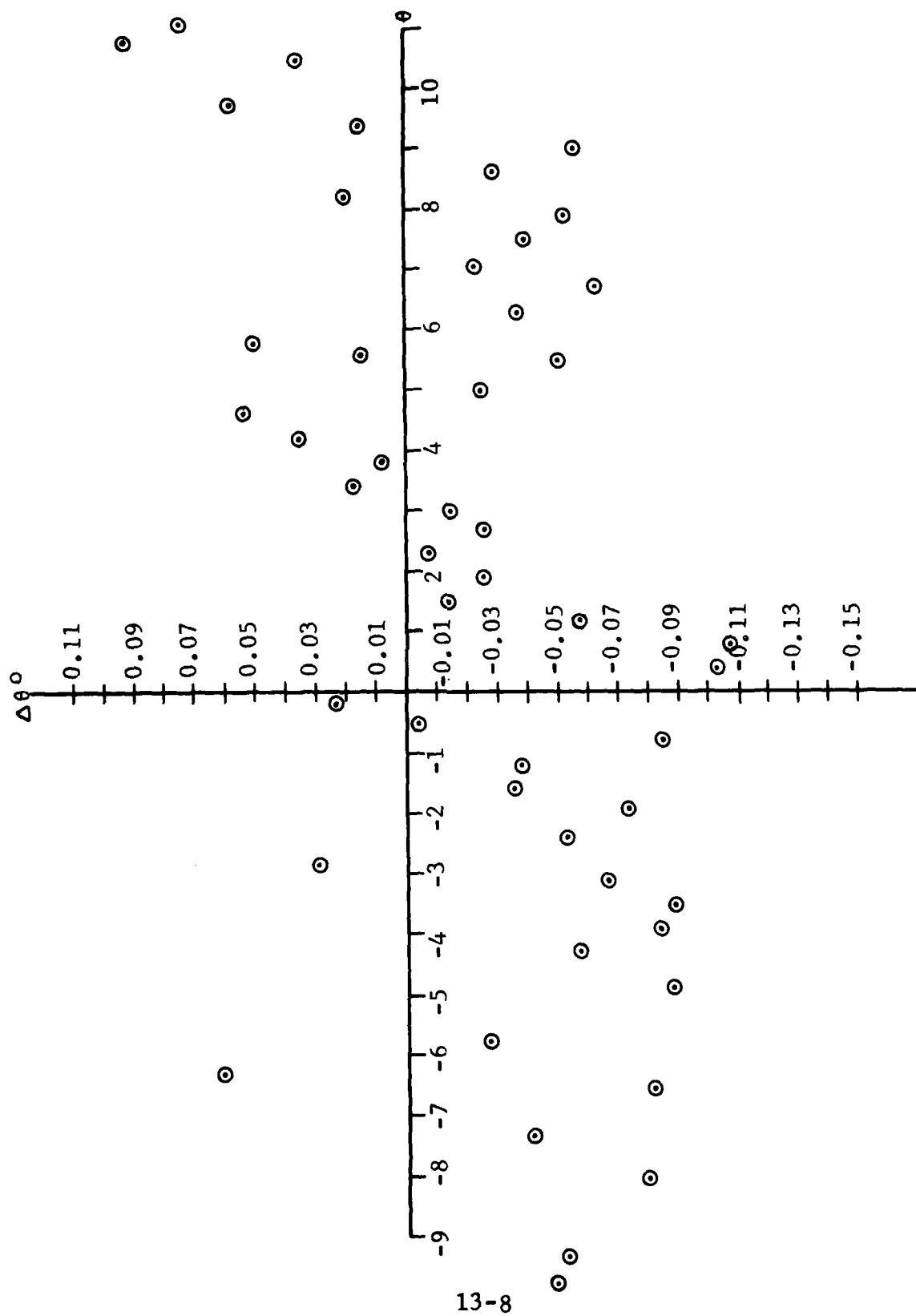


Figure 3.1 Scanning Mirror Position Jitter During Launch

Table I

| Flight Time | Blackbody Temp. (°K) | Tungsten Source Temp. (°K) |
|------------------|-------------------------|-------------------------------|
| T ₀ | 300°K | 221.0 |
| T ₃₀ | 299.4K | 220.7 |
| T ₆₀ | | |
| T ₉₀ | | |
| T ₁₁₈ | | |
| T ₁₅₀ | | |
| T ₁₈₀ | | |
| T ₂₁₀ | | |
| T ₂₃₃ | | |
| T ₂₄₀ | | |
| T ₂₇₀ | | |
| T ₂₇₃ | | |
| T ₃₀₀ | | |
| T ₃₆₀ | | |
| T ₃₉₀ | | |
| T ₄₂₀ | | |
| T ₄₄₁ | | |

299.9°K

220.7

Calibrator Source Temperatures

then plugged into this "ideal" equation and the "ideal" voltage output of the transducer was generated. The difference between this ideal voltage and the actual measured voltage was then the assumed jitter or error in the scanner position. This voltage error was then converted to an angular position error and plotted versus the angular position. Figure 3.1 shows the angular error during the launch phase when maximum vibration and acceleration were encountered.

As is evident, the angular error or jitter did not exceed 0.1 degrees during launch.

3.3 Blackbody Calibrator

The blackbody calibrator was the primary calibrator up to the time of cover deployment at which time the tungsten source calibrator became the primary calibrator. Table I gives the temperature of the blackbody at thirty second intervals during the flight. The temperature held to within $\pm .10^{\circ}\text{K}$.

3.4 Tungsten Source Calibrator

The tungsten source calibrator was the primary calibrator after cover deployment. Six calibrations were performed during the flight using the tungsten source. The detector signal responses for several detectors were reduced and are summarized in Table II. The first five calibrations were used. They were spaced approximately 40 seconds apart. The table gives the mean calibration signal levels for each of the detectors and their standard deviation over the five calibrations. The deviation in all cases is less than five percent which indicates both stable source output and detector/preamp responsitivity. Table I also shows the temperature of the tungsten filament at thirty second intervals over the entire flight. No significant change could be detected.

Table II

MWIR Detector/Tungsten Source Repeatability - 5 Calibrations

| <u>Channel</u> | <u>Mean Calib. Signal ()</u> | <u>Std. Deviation (Total)</u> |
|----------------|-----------------------------------|------------------------------------|
| 1 | 160 | 7.1 |
| 2 | 260 | 8.4 |
| 3 | 270 | 10.0 |
| 4 | 290 | 15.8 |
| 5 | 350 | 13.0 |

3.5 Sensor Temperature

The sensor temperature stability is a critical parameter for sensor operation. Table III shows the temperature of key points in the sensor during the flight. As is evident all internal sensor temperatures did not change by more than 0.3°K . The electronics assembly did rise about 3.5°C . This was caused by the loss of convective cooling of the electronics assembly as the rocket payload ascended into a vacuum. The 3.5°C rise is not significant because the electronics is designed to accomodate a 30°C temperature rise.

The four sensor voltage supplies (+15V, -15V1, -15v2 and +5V) showed no change in level over the entire flight.

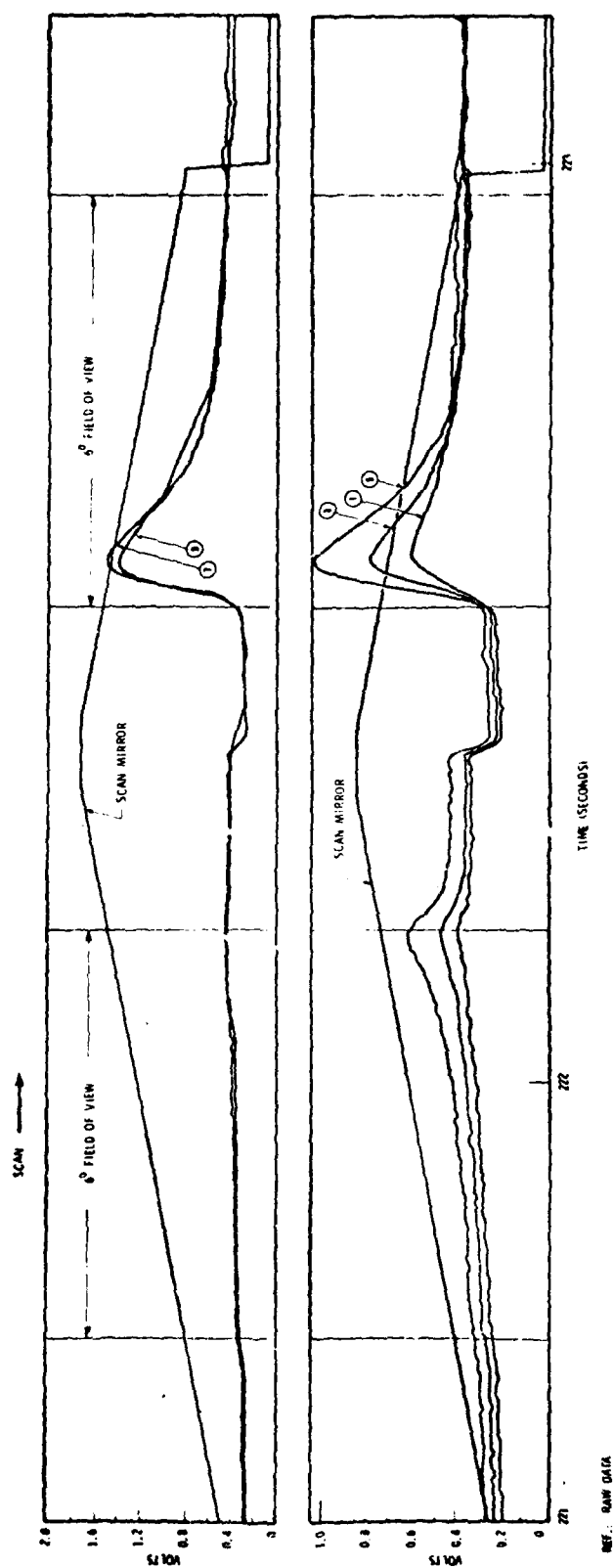
4.0 Mission Data

As is evident, the sensor module was in a tumbling mode during the mission. The detector data did show high level signals and in some cases saturating signals as the Earth and rocket booster crossed the sensor field of view.

During a short interval, the target engine appears to have crossed the sensor module Field of View as indicated by the on-board T.V. camera. The Spatial Radiometer did record a signal at this time also. Figure 3.2 shows the plot of five MWIR large element channel outputs along with the scan mirror position. The target appears at the edge of the Field of View and was probably moving quite fast because less than one seconds worth of data was recorded. The abrupt step in the signal channels at scanner turn-around is the clamping action of the preamps and has nothing to do with the signal. The SWIR detectors showed no signal response.

| Flight Time | Electronics Assy. (°C) | N ₂ Tank Top Right Front (°K) | Focal Plane (°K) | Scan Mirror (°K) | N ₂ Tank Rear Upper Right (°K) |
|------------------|---------------------------|--|---------------------|---------------------|---|
| T ₀ | 20.0 | 79.8 | 79.0 | 80.0 | 79.7 |
| T ₃₀ | 19.6 | 79.6 | | 79.9 | 79.5 |
| T ₆₀ | 19.6 | 79.8 | | 79.9 | 79.6 |
| T ₉₀ | 20.1 | 79.6 | | 79.9 | |
| T ₁₁₉ | 20.6 | 79.6 | | | |
| T ₁₅₀ | 21.1 | 79.4 | 79.0 | | |
| T ₁₈₀ | 21.4 | 79.4 | 79.1 | | |
| T ₂₁₀ | 21.8 | 79.6 | | | |
| T ₂₃₃ | 32.0 | | | | |
| T ₂₄₀ | 22.0 | | | | |
| T ₂₇₀ | 22.3 | | | | |
| T ₂₇₃ | 22.3 | | | | |
| T ₃₀₀ | 22.5 | | 78.9 | | |
| T ₃₁₃ | 22.6 | | 78.8 | | |
| T ₃₃₀ | 22.7 | | | | |
| T ₃₅₃ | 22.8 | | | | |
| T ₃₆₀ | 22.8 | | | | |
| T ₃₈₀ | 23.0 | | | | |
| T ₃₉₀ | 23.0 | | | | |
| T ₄₂₀ | 23.2 | | | | |
| T ₄₄₁ | 23.4 | 79.6 | 78.8 | 79.9 | 79.6 |

Sensor Temperatures During Flight
Table III



13-14

Figure 3.2 MMIR DETECTORS FAR FIELD

Section XIV

System No. 2

14-1

7902-4

Summary

This section outlined the tests and evaluation efforts performed on System No. 2 thru December 31, 1978.

The system was not launched as scheduled due to a pre-separation on the launch and will be re-scheduled for an early 1979 flight.

System No. 2

1.0 System No. 2 Spatial Radiometer was started in parallel with System No. 1. During the initial problem phases System No. 2 was put on Hold until corrective action results on System No. 1 were resolved.

As a result, the initial focus, detector mask and scan mirror vibration problems were eliminated. The sensor was assembled in December 1977 and the integration/checkout phase was continued. The second focal plane was manufactured in the same manner as focal plane No. 1 and similar anomaly behavior of the SWIR detectors were noted.

AFGL requested EOC to evaluate the problem because they did not want to fly System No. 2 with reduced sensitivity of the MWIR channels.

To help evaluate the problem additional EOC Staff personnel were involved on the program. Many iterative tests were completed on the focal plane with no new solutions to the problem. An EOC representative visited OCLI in California to discuss the focal plane problem. The result of the meeting included a series of filters lent on consignment by OCLI to EOC for further evaluation of the focal plane.

The following tests were performed to evaluate the SWIR anomaly.

- A. An AFGL borrowed SWIR notch filter mounted on focal plane
- B. Reduced aperture on extended source calibrator with normal focal plane configuration
- C. Calcium fluoride .230 thick window located in front aperture first field stop position

- D. OCLI LWIR pass filter located in Lyot Stop position
- E. OCLI SWIR pass filter located in Lyot Stop position
- F. OCLI SWIR pass filter in Lyot Stop position with optical bias changes
- G. OCLI SWIR pass filter in Lyot Stop position with optical and detector bias voltage changed
- H. Removed flight filters and installed OCLI SWIR spike filter in Lyot Stop position
- I. Installed 1" thick C_aF_e window in Lyot Stop position with flight filters removed.
- J. With 1" thick C_aF_e window in Lyot Stop position flight filter position on focal plane was reversed
- K. Extended blackbody source on AFGL calibration tester
- L. Used EOC calibration source with flight configuration and varied source apertures and temperature
- M. Extended waveguide installed on AFGL calibrator and normal focal plane assembly
- N. AFGL extended source calibrator with reduced aperture on focal plane spider and normal focal plane

The results of all the tests with the filters showed little improvement.

A meeting with Dr. J. Jamieson, HEOC and AFGL was held to discuss the SWIR channel behavior. After an indepth discussion of the anomalous behavior of the SWIR channel and methods of testing, both EOC and Dr. J. Jamieson indicated that the BONC calibration may be the cause, and further investigation would be required.

A decision was made by EOC and AFGL to order a new SW filter from OCLI without spectral leaks. Tests and evaluations of the system continued thru the end of December.

Field mapping and boresight alignments were completed

during this evaluation phase. The field map procedure and results were approximately the same as System No. 1. The boresight alignment was $\times .016^\circ$ on System No. 2.

The scanner, blackbody and tungsten calibration sources all operated as required. No changes were made in these sub-assemblies from System 1.

The second dip brazed cryogen tank structure developed leaks similar to the first unit, however, the brazement could not be repaired by impregnation or epoxy methods. Electrical tests continued using a vacuum pumping station. A plan was developed to complete the electrical tests and repair the cryogen tanks by electron beam welding. This course of action was in line with the existing flight schedule of System No. 2.

A decision in December was made to replace the cryogen tanks with new electron beam welded tanks on the brazement. After completing electrical tests the initial plan was to EB-weld over existing brazed joints to insure vacuum tight integrity. Brazing alloys were checked and found to be compatible with the EB process. The first problem encountered as the tanks were removed was additional seams and dowel pin joints that were not indicated on the original drawing. In addition, the EB weld and braze joints were not compatible for EB welding. An excess of foreign particles in the braze joints caused the EB welds to open or blow holes in the existing seams.

After completion of the electron beam welding, the cryogen tanks were still not leak tight. An attempt to fix the leak areas with additional electron beam touch-up did not solve the problems.

AFGL was informed of the problem and a new schedule for the delivery of System No. 2 was developed.

An alternate method of heli-arc welding over the electron

beam process was tried. The heli-arc method sealed some of the leaks on the electron beam welds, however, additional leaks developed due to the high heat required for the arc weld process.

The welding process was stopped and the problem was evaluated at EOC. The decision was made to remove the existing tanks and replace with individual welded tanks welded to each side of the optical structure brazement. Each individual tank was constructed similar in size and shape to the original configuration. The overall weight of the system was increased by six pounds and a total loss of one liter in the tank capacity was sacrificed. The one liter loss in cryogen capacity did not affect the eight (8) hour hold time of the system. The welding of the new tanks to the brazement required a complete re-processing of the structure, including stress relieving, heat treat and re-machining for optical alignment.

The following paragraphs will outline the structural analysis performed based on the new tank concept.

Spatial Radiometer Structural Analyses:

Structural analyses of the re-configured tanks and dewar flange was performed to predict tank and weld stresses for 1, 3 atmospheres pressure and dynamic loads. The analyses assume that:

- 1) The tanks' baffles are welded to the tanks' flat plates,
- 2) H-frame covers are attached to the H-frame in a manner to carry structural loads, and
- 3) Tack welds of the tanks to the H-frame sides can carry structural loads from tank flat plates to the H-frame sides.

SPATIAL RADIOMETER STRUCTURAL MODEL

The predicted vibration resonances, stresses and safety factors are listed below. These results predict the maintaining of structural integrity for operational pressure and dynamic testing.

A STARDYNE structural model of one of the tanks, baffle covers' stiffness and section of H-frame side (between baffles) was used for predicting 1 and 3 atmospheric pressure stresses. Figure 2 shows the structural model. Table I lists stresses and safety factors at tank and baffle welds. The minimum safety factor listed in Table I is 5.88.

A STARDYNE structural model of the dewar (assumed rigid) mounted with a G-10 cylinder to the pressure vessel was analysed. The first G-10 cylinder bending mode frequency was predicted to be 186 Hz. The lowest torsional dewar frequency was predicted to be 736.5 Hz. A comparison of this 186 Hz G-10 cylinder resonance and the dewar torsional frequency of 365 Hz shows an acceptable frequency separation. Thus, the G-10 cylinder and dewar torsional vibration modes will not amplify their individual resonances during the dynamic testing. The tack welds, carrying structural loads, will not cause slapping of the tank flat plates during dynamic testing. This is because dynamic test deformations of the unsupported tank flat plates do not exceed the 1 atmospheric pressure.

The complete system was qualified to acceptance test levels of AFGL tech data spec no. 76-4 on May 31. EOC Test Plan, and Test Reports from EOC and Acton Environmental Test Laboratory are included in Volume II. The system was delivered to AFGL on June 5, 1978.

Ref: Vibration Test Plan No. 22715-ESOR

Ref: Dynamic Environmental Test Report No. 061578-0023

Ref: Acton Environmental Test Report No. 13963

TABLE I
SPATIAL RADIOMETER STRUCTURAL ANALYSIS

| LOCATION | Maximum Stress, psi | | Operational | |
|-----------------------|---------------------|---------------|----------------|--|
| | Static Pressure | | Minimum Stress | |
| | 1 atm., oper. | 3 atm., proof | Safety Factor | |
| Tank Weld, Joint 1 | 2325. | 6976. | 7.74 | |
| Tank Weld, Joint 7 | 2284. | 6853. | 7.89 | |
| Baffle Weld, Joint 8 | 3067. | 9201. | 5.88 | |
| Baffle Weld, Joint 12 | 3023. | 9070. | 5.94 | |

Point source and extended source calibrations were done at AFGL during 6/78. In addition the detector/preamp frequency response, detector spectral response and crosstalk were measured. The data is being reduced by AFGL and has not been available to EOC as of this report.